UNIVERSITÀ
DEGLI STUDI
DI PADOVA

Università degli Studi di Padova

Dipartimento di Fisica ed Astronomia “G. Galilei”

SCUOLA DI DOTTORATO DI RICERCA IN FISICA

INDIRIZZO COMUNE

CICLO XXVIII

TESI DI DOTTORATO DI RICERCA IN FISICA

Integrated Opto-Microfluidic Lab-on-a-Chip in Lithium Niobate for Droplet Generation and Sensing

Direttore della Scuola: Ch.mo Prof. ANDREA VITTURI

Supervisore: Ch.ma Prof.ssa CINZIA SADA

Dottorando: GIACOMO BETTELLA

Abstract

In the last decades microfluidics has gained an increasing interest by the scientific community due to its capability of manipulating liquids on the microscale. In particular droplet microfluidics technology holds great promise due to its precise control on very small volumes of fluid: droplets can be coalesced, mixed and sorted, employed either as micro chemical reactors or as carriers of biological samples.

This features, in combination with fast analysis tools, allow for the realization of Lab-on-a-Chips (LOCs), miniaturized and portable devices able to perform chemical, biological, environmental or medical analyses where laboratory facilities lack.

Nevertheless, in most cases, sensing inside LOCs is performed by external optical stages somehow added to the microfluidic chip. One of the hurdle towards the effective employment of such systems is indeed the complete integration between the microfluidic stage and the optical one. Often extended systems such as microscope objectives and fast CCD cameras have been used to detect droplets inside microfluidic channels nullifying the efforts spent to decrease the dimensions of LOCs and their related advantages.

In this work the first opto-microfluidic Lab-on-a-Chip (LOC) for both generation and detection of droplets, entirely integrated in lithium niobate is presented.

The main elements of the LOC are a passive droplet generator, where water in oil droplets are produced by the cross-flow of immiscible phases, and two waveguides on the surface of the crystal able to illuminate droplets perpendicularly to their flow and to collect the transmitted intensity.

The realization of single mode channel waveguides at a wavelength of 632.8 nm on lithium niobate by titanium in-diffusion is achieved and the obtained waveguides are characterized by Rutherford Backscattering Spectrometrxy (RBS), Secondary Ion Mass Spectrometry (SIMS) and near field measurements.

A deep investigation on the applicability of lithium niobate on the field of microfluidics is carried out through a study of its wettability. In addition a functionalization procedure to improve its hydrophobicity is defined.

Various techniques to engrave the microfluidic channels directly on the crystal are taken into account. In particular the ablation by a femtosecond pulsed laser at a wavelength of 800 nm is widely investigated by optical microscopy and atomic force microscopy (AFM)

in order to define the best process parameters to get the lower average roughness of the channel walls ($R_a \sim 50\,\mathrm{nm}$). Channels engraved with a dicing saw are also characterized showing to be the best solution for optofluidic applications due to their extremely low average roughness ($R_a = (6 \div 7)\,\mathrm{nm}$).
New techniques for sealing the channels engraved on the surface of the crystal are described with a particular care to the device durability and its applicability to different purposes. Passive droplet generators with a T-junction geometry obtained by laser ablation in lithium niobate are shown to generate droplets in a wide range of frequencies (10÷1000Hz) and with a very sharp distribution of droplets volumes ($\sigma < 3\%$). Their performances are characterized employing an optical microscopy setup and the experimental data are discussed with respect to the theoretical models reported in literature. Discrepancies from the theory at low values of the capillary number ($Ca < 3 \cdot 10^{-3}$) are highlighted and described by means of an empirical law.

Finally the coupling of the waveguides to the microfluidic stage is discussed showing how it can be used to count and trigger the droplets during their flow, achieving better performances than the standard optical microscopy setup.
The ultimate configuration of the presented LOC prototype is characterized by two crossing channels obtained by mechanical dicing with three inlet branches and one outlet branch. Three phases are flown together (oil, water and a saline solution) and alternating droplets of pure water and saline solution are produced in oil. The transmitted intensity from the waveguide is shown to be sensitive to the refractive index of the solution with a sensitivity of $\Delta n = 2 \cdot 10^{-3}$ in the range $n = [1.339, 1.377]$.

This is the first example of a Lab-On-a-Chip for real time droplet counting and refractive index sensing, completely integrated in lithium niobate.

Estratto

Negli ultimi decenni la microfluidica ha riscosso un crescente interesse presso la comunità scientifica grazie alla sua capacità di manipolare liquidi su scala micrometrica. In particolare la microfluidica a gocce è particolarmente promettente per la possibilità di controllare volumi di fluido molto ridotti: le gocce possono essere unite, mescolate e selezionate, utilizzate come microreattori chimici o per trasportare campioni biologici.

Queste peculiarità, unite a strumenti di analisi rapidi, permettono di realizzare i cosiddetti Lab-on-a-Chip (LOC), dispositivi miniaturizzati e portatili capaci di condurre analisi chimiche, biologiche, ambientali o mediche in mancanza di veri e propri laboratori.

Ciononostante, nella maggior parte dei casi, la rilevazione all'interno dei Lab-on-a-Chip viene praticata da stadi esterni di ottica affiancati al chip microfluidico. Infatti uno degli ostacoli maggiori verso l'effettivo utilizzo di questi sistemi è il raggiungimento di una completa integrazione tra lo stadio microfluidico e quello ottico. Spesso sistemi ingombranti come gli obiettivi di un microscopio o fotocamere veloci sono utilizzate per rilevare gocce all'interno di canali microfluidici, vanificando gli sforzi fatti per ridurre le dimensioni dei LOC e i vantaggi ad essi collegati.

In questo lavoro viene presentato il primo Lab-on-a-Chip opto-microfluidico per la generazione e la rilevazione di gocce, interamente integrato in niobato di litio.

I principali elementi del LOC sono un generatore di gocce passivo, dove vengono prodotte gocce di acqua in olio attraverso l'incontro tra flussi di fasi immiscibili, e due guide d'onda sulla superficie del cristallo capaci di illuminare le gocce perpendicolarmente alla direzione in cui scorrono e raccoglierne l'intensità trasmessa.

Vengono mostrate la realizzazione di guide a canale monomodo alla lunghezza d'onda di 632.8 nm in niobato di litio per diffusione di titanio e la loro caratterizzazione attraverso le tecniche di Rutherford Backscattering Spectrometry (RBS), Secondary Ion Mass Spectrometry (SIMS) e near field.

Un'indagine approfondita sull'applicabilità del niobato di litio in campo microfluidico viene svolta attraverso lo studio delle sue proprietà di bagnabilità. In aggiunta viene definita una procedura di funzionalizzazione per aumentarne l'idrofobicità.

Vengono prese in considerazione varie tecniche per scavare i canali direttamente sul cristallo. In particolare l'ablazione per mezzo di un laser impulsato al femtosecondo ad una lunghezza

d'onda di 800 nm viene caratterizzata tramite microscopia ottica e microscopia a forza atomica (AFM) per stabilire i migliori parametri del processo al fine di ottenere la minima rugosità media possibile ($R_a \sim 50\,\text{nm}$). Vengono inoltre caratterizzati canali scavati con una lama autolucidante che risultano essere la migliore soluzione nell'impiego in optofluidica per la loro rugosità estremamente ridotta ($R_a = (6 \div 7)\,\text{nm}$).

Sono state inoltre sperimentate nuove tecniche per la chiusura dei canali, prestando particolare attenzione alla durevolezza del dispositivo e alla possibile applicazione in diversi campi.

Si mostra come i generatori passivi di gocce con geometria a "T" (T-junction) ottenuti per ablazione laser in niobato di litio siano in grado di generare gocce in un ampia gamma di frequenze ($10 \div 1000\,\text{Hz}$) e con una distribuzione di lunghezze estremamente piccata ($\sigma < 3\%$). Ne vengono caratterizzate le prestazioni con l'impiego di un sistema di microscopia ottica e i dati sperimentali vengono discussi confrontandoli con i modelli teorici riportati in letteratura. Le discrepanze tra la teoria e i dati sperimentali a bassi valori del numero di capillarità ($Ca < 3 \cdot 10^{-3}$) vengono evidenziate e descritte per mezzo di una legge empirica.

Infine viene affrontato l'accoppiamento delle guide d'onda allo stadio microfluidico mostrando come il chip possa essere sfruttato per misurare il tempo di passaggio delle gocce, ottenendo risultati migliori rispetto al classico sistema di microscopia ottica.

La configurazione finale del LOC è caratterizzata da due canali che si intersecano, ottenuti per lavorazione meccanica, con tre rami di immissione e uno di uscita. Tre fasi vengono flussate contemporaneamente (olio, acqua e una soluzione salina) in modo da ottenere gocce alternate di acqua e di soluzione salina in olio. Si mostra come l'intensità trasmessa dalla guida d'onda dipenda dall'indice di rifrazione della soluzione salina con una sensibilità di $\Delta n = 2 \cdot 10^{-3}$ nel range di valori $n = [1.339, 1.377]$.

Il dispositivo presentato è il primo esempio di Lab-On-a-Chip per il conteggio e la misure dell'indice di rifrazione di gocce in tempo reale, completamente integrato in niobato di litio.

Contents

List of Figures

List of Tables

Introduction

This research aims to make a further step towards one of the most challenging targets pursued by the applied sciences of the last twenty years, i.e. the realization of miniaturized and portable devices able to perform chemical, biological, environmental or medical analysis where laboratory facilities lack.
The final purpose of this research field is to integrate multiple laboratory functions inside a single chip with dimensions of less than few square centimetres, able to manipulate volumes of fluid of the order of nanolitres. The main advantages of these so called Lab-On-a-Chips (LOCs) are:

- portability, which gives the possibility of performing on-field measurements without the need of lab facilities;
- lower reagents volume consumption since very small quantity of fluid can be manipulated;
- high throughput due to the easiness in manipulating such small volumes of fluid which allow for fast multiplexed simultaneous analyses.

In most cases sensing inside LOCs is performed by optical stages someway added to the microfluidic chip. One of the hurdle towards the effective employment of such systems is indeed the complete integration between the fluidic stage and the optical one. Often extended systems such as microscope objectives and CCD cameras have been used to detect droplets inside microfluidic channels, nullifying the efforts spent to decrease the dimensions of LOCs and their related advantages. Recently some better solutions have been proposed using optical fibres embedded in the same polymeric matrix employed to realize the fluidic stage [3,4]. However polymeric materials are useful in reducing costs but suffer degradation and poor stiffness, so they are not suitable for steady and durable devices. A different approach was the employment of optical waveguides coupled to microfluidic channels both fabricated by femtosecond laser irradiation on fused silica. Nevertheless no attempt to use this system both to inject the laser beam and to collect the optical signal as well are reported [5–7].

On the other hand lithium niobate could be a good candidate to be employed for an opto-fluidic chip due to its widely acknowledged optical properties largely exploited in the past for telecommunication applications. Waveguides, optical modulators, Bragg gratings, Mach-Zender interferometers can be realized on a single lithium niobate crystal.

Nowadays lithium niobate has been already effectively used to move nano-droplets inside microfluidic channels, exploiting surface acoustic waves (SAW) thanks to its piezoelectricity [8,9] and very recently it has also been employed to trap particles dispersed in oil exploiting its photovoltaic properties [10–13].

Nevertheless microfluidic channels have surprisingly never been realized in lithium niobate until now, missing the possibility to integrate in the same substrate a microfluidic chip and an optical stage.

In this thesis the first Lab-on-a-Chip prototype for both generation and detection of droplets, completely integrated in lithium niobate is presented.

The main idea is to couple two optical waveguides perpendicularly to a microfluidic channel in order to perform an optical analysis of the droplets flowing therein. The elements of the prototype are:

- a droplet generator characterized by a junction between two perpendicular microfluidic channels where water droplet in oil are produced by passive interaction between the two immiscible fluids;
- two facing waveguides perpendicular to the microfluidic channel where droplets flow; the first employed to confine and carry the light which illuminate the droplets, and the second one on the opposite side of the channel used to collect the transmitted intensity.

Here the effective employment of this system to count and trigger water droplets, and to simultaneously measure their refractive index is shown.

This work is included in the framework of a comprehensive project which has the aim to perform optical analysis of droplets constituents by the detection of the fluorescence emitted from specific markers. In this case a further optical stage is needed i.e. a Bragg reflecting grating written on the collecting waveguide by exploiting the photorefractive effect, a typical feature of lithium niobate. This refractive index grating is needed to reflect the light at the wavelength of the pump beam in order to reduce abruptly the transmitted intensity coming from the inlet waveguide and allow for the detection of the fluorescence in the collecting waveguide.

The present thesis is organized as follows:

Chapter 1 will present lithium niobate, outlining its compositional, piezoelectric, pyroelectric and optical properties. A particular attention is devoted to that properties which could be employed in the field of optofluidics, a research area where lithium niobate is a quite unexplored material.

Chapter 2 , after a brief excursus on the state of the art about optical waveguides in lithium niobate, will deal with the realization by titanium in-diffusion of single mode waveguides at 633nm and their characterization by means of Rutherford Backscattering Spectroscopy (RBS) and Secondary Ion Mass Spectroscopy (SIMS), together with the discussion of the results from a FEM based simulation.

Chapter 3 will be dedicated to droplet microfluidics and in particular to the explanation of the theoretical models describing the behavior of the T-junction droplet generators, which are used in the microfluidic stage of the Lab-on-a-Chip presented here.

Chapter 4 will be addressed to the realization of microfluidic channels directly engraved in lithium niobate. In particular laser ablation and mechanical dicing will be presented together with the characterization of the microfluidic channels obtained by means of these techniques. The techniques employed to close the channels will be also described. Finally a wettability study of lithium niobate and a functionalization process to increase its hydrophobicity will be presented.

Chapter 5 will show the results from the characterization of the realized droplet generators illustrating their performances and comparing the experimental results with the theoretical models proposed in literature.

Chapter 6 will deal with the coupling of the waveguides to the microfluidic channels. The results obtained from the final prototype configuration are discuused showing its employment as a droplet counter, trigger and as a refractive index sensor.

1 Lithium Niobate

1.1 Compositional and crystallographic properties

Lithium niobate is a synthetic material and cannot be found in nature. It was described for the first time by Zachariasen in 1928 and then widely investigated by Nassau and Abrahams at Bell Laboratories in the sixties. It is a solid, transparent material not soluble in water and organic solvents. It is one of the four compounds of the pseudo-binary system Li_2O-Nb_2O_5, besides $Li_2Nb_{28}O_{71}$ Li_3NbO_4 and the lithium triniobate $LiNb_3O_8$. The crystal is usually grown by Czochralski technique in its *congruent* composition which is characterized by a lithium deficiency (48.45% of Li_2O). This composition corresponds to a maximum in the liquid-solid curve as depicted in the phase diagram in fig.1.1. At the congruent composition the melt and the growing crystal are identical with respect to the composition, so these crystals show the highest uniformity of the their chemical and physical properties. On the contrary, in other cases, such as the stoichiometric crystal, the composition of the melt and the crystal are slightly varying during the growth and the crystal becomes non-uniform, particularly along the growth axis.

Several physical and optical properties, like the phase transition temperature, the birefringence, the photovoltaic effect and UV band absorption edge, strongly depend on the ratio between the concentration of lithium and that of niobium ratio [15]. This is why the congruent composition is preferred and stoichiometric wafer are not available in commerce.

At room temperature a $LiNbO_3$ crystal exhibits a mirror symmetry about three planes that are 60° apart. The axis obtained by their intersection is the center for a three-fold rotational symmetry of the crystal. These symmetry operations classify the lithium niobate as a member of the space group $R3c$, with point group $3m$. Above the transition temperature it belongs to the centrosymmetric space group $R\bar{3}m$.

In the trigonal system the definition of the crystallographic axes is not unambiguous and three different cells can be chosen: hexagonal, rhombohedral or orthohexagonal. In most

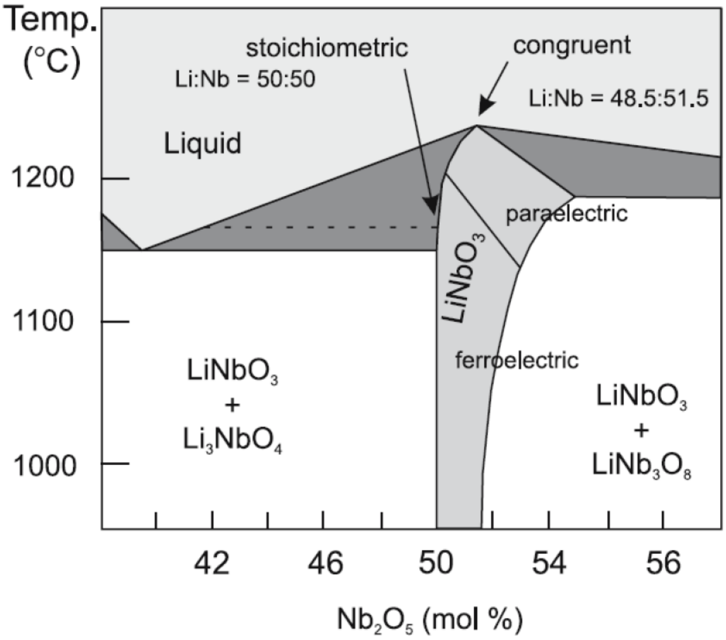

Figure 1.1: Phase diagram of the Li_2-Nb_2O_5 system [14].

applications the orthohexagonal is preferred and usually the tensor components describing lithium niobate physical properties are expressed with respect to the axes from this picture. Nevertheless in crystallography applications the other two descriptions are used as well. The three mutually orthogonal reference axes in the orthohexagonal convention are:

- the z-axis (also indicated as c-axis or optical axis) which is the axis around which the crystal exhibits its three-fold rotation symmetry;
- the y-axis, which lays on the mirror plane;
- the x-axis, perpendicular to the previous ones.

Piezoelectricity is proper of z-axis and y-axis and by convention their positive direction is chosen to be pointing on the negatively charged plane under uniaxial compression. Due to the crystal pyroelectricity along the optical axis, z-axis direction is also indicated as that pointing to the positively charged plane while the crystal is cooling.
Commercial wafers from Crystal Technology employed during the work for this thesis have facets along the circular border at specific directions in order to be easily oriented.

Lithium niobate structure at temperatures below the ferroelectric Curie temperature (T_C = (1142.3 ±0.7)°C for conrgruent composition) consists of planar sheets of oxygen

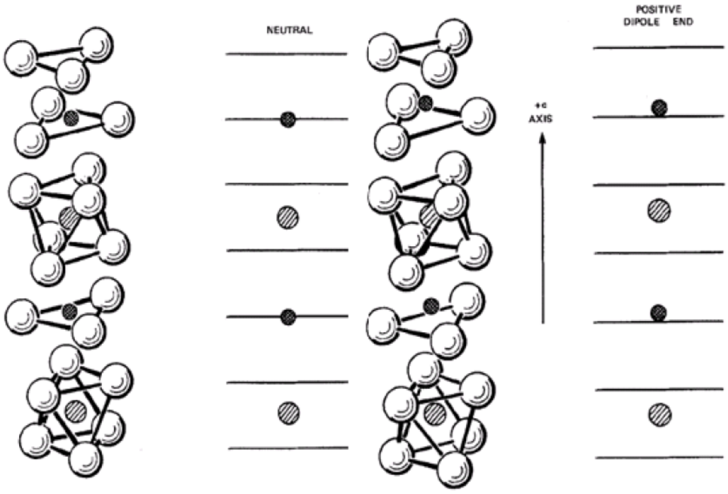

Figure 1.2: Compositional structure of lithium niobate together with the sketched positions of lithium and niobium atoms with repsect to the oxygen planes for the paraelectric (left) and ferroelectric phase (right).

atoms in a slightly distorted hexagonal close-packed configuration (see fig.1.2). The octahedral interstices formed by this oxygen structure are one-third filled by lithium atoms, one-third by niobium and one third is vacant, following, along the c axis, the order Li-Nb-vacancy. In the paraelectric phase, above the Curie temperature, the lithium atoms lie in the oxygen planes, while niobium ions are located at the center of oxygen octahedrals. This phase has thus no dipolar moment.

On the contrary, as the temperature decreases below T_C, lithium and niobium atoms are forced into new positions: the Li ions are shifted with respect to the O planes by about 44pm, and the Nb ions by 27pm from the center of the octahedra. These shifts cause the arising of a spontaneous polarization.

1.2 Defects and Doping

Impurities and structural modifications are extremely important in the study of lithium niobate since they can modify considerably its physical properties.

As mentioned before congruent lithium niobate has a sub-stoichiometric fraction of lithium which corresponds to the lack of about the 6% of lithium atoms respect to the stoichiometric composition. Structure modifications are thus needed to ensure charge compensation after Li_2O outdiffusion.

Three different models have been proposed:

- *oxygen vacancy model*: when lithium oxide outdiffusion is compensated by oxygen vacancies as it usually occurs in the oxides perovskites

$$\langle LiNbO_3\rangle \rightarrow 2V_{Li}^{+} + V_{O}^{2-} + Li_2O$$

- *lithium vacancy model*: when some of the lithium vacancies are compensated by niobium atoms (*niobium antisites*)

$$\langle LiNbO_3\rangle \rightarrow 4V_{Li}^{-} + Nb_{Li}^{4+}) + 3Li_2O$$

- *niobium vacancy model*: when both niobium vacancies and niobium antisites concur to reach compensation

$$\langle LiNbO_3\rangle \rightarrow 4V_{Nb}^{5+} + 5Nb_{Li}^{4+} + 3Li_2O$$

The question on which of this mechanism prevails is still under debate but the oxygen vacancy model seems to be disproved by density measurements [16] which instead confirm the hypothesis of niobium antisites. This substitutional niobium atoms are important since they introduce donor and acceptor levels in the bandgap of the stoichiometric crystal giving rise to the photovoltaic and phtorefractive effect even in the absence of extrinsic impurities as it will be explained in section 1.3.6.

Even more importance was gained in the past by extrinsic defects, since they have been employed to tailor lithium niobate properties since the sixties.

Lithium niobate doping is quite straightforward, due to its high concentration of vacancies. Dopants can be added both during the crystal growth or after the solidification by thermal diffusion or ion implantation.

Extrinsic defects are used both to enhance or reduce the photorefractive effect: Fe on one hand, Mg, Zr, Zn and Hf on the other hand.

Titanium by thermal in-diffusion and hydrogen by proton exchange are used to produce optical waveguides on the surface of the crystal.

Erbium doping was also exploited in order to realize integrated laser sources [17].

Parameter	Ordinary	Extraordinary
A_0	$4.5312 \cdot 10^5$	$3.9466 \cdot 10^5$
A_1	$-4.8213 \cdot 10^8$	$79.090 \cdot 10^8$
A_{IR}	$3.6340 \cdot 10^8$	$3.0998 \cdot 10^8$
A_{UV}	2.6613	2.6613
λ_0	223.219	218.203
n	2.2866	2.2028

Table 1.1: Parameters for generalized Sellmeier equations at room temperature and refractive indices for $\lambda = 632.8$nm.

1.3 Physical Properties

1.3.1 Optical Properties

Pure lithium niobate is a transparent crystal presenting a negligible absorption coefficient from 0.35μm to about 5μm. Light absorption coefficient is very sensitive to the presence of defects or impurities while light propagation is weakly affected by scattering (the extinction coefficient being 0.16dB/cm).

Due to the crystallographic structure and the symmetry properties of lithium niobate, its permittivity tensor, in the orthohexagonal cell reference framework, can be represented by a 3×3 matrix with the form:

$$\bar{\bar{\varepsilon}} = \begin{pmatrix} \varepsilon_{11} & 0 & 0 \\ 0 & \varepsilon_{11} & 0 \\ 0 & 0 & \varepsilon_{33} \end{pmatrix} \tag{1.1}$$

The anisotropy of the permittivity tensor lead to the characteristic birefringence of lithium niobate. In fact two different refractive indices can be found in lithium niobate depending on the orientation of the electric filed: the ordinary refractive index $n_o = \sqrt{\varepsilon_{11}/\varepsilon_0}$ for electromagnetic waves polarized perpendicularly to the z-axis of the crystal and the extraordinary refractive index $n_e = \sqrt{\varepsilon_{33}/\varepsilon_0}$ in the case of a wave with a polarization parallel to the optical axis.

Refractive indices dependence on light wavelength and crystal composition can be interpolated by the generalized Sellmeier equation [18], which is valid in the wavelength range

$\lambda = 400 \div 3000$nm and for compositions of $C_{Li} = 47 \div 50$mol% to an accuracy of 0.002 in n_i:

$$n_i^2 = \frac{A_{0,i} + A_{1,i}(50 - C_{Li})}{\lambda_{0,i}^{-2} - \lambda^{-2}} + A_{UV} - A_{IR,i}\lambda^2 \tag{1.2}$$

where $i = \{o, e\}$ for ordinary or extraordinary polarization respectively and λ is expressed in nanometers. The intensity factors A describe the influence of various oscillators responsible for the refractive indices in the visible and the near infrared region: A_0 for Nb on Nb site, A_1 for Nb on Li site, A_{UV} for high energy oscillators (states in the conduction band, plasmons), A_{IR} for phonons. The parameters at room temperature are listed in table 1.1 together with the typical refractive indices for a congruent composition at a wavelength of 632.8nm, corresponding to a He-Ne laser. Apart on the Li/Nb ratio, lithium niobate refractive indices depend strongly on extrinsic impurities and this feature can be exploited to tailor n_o and n_e by doping. An example of such an advantage is the doping with titanium for the realization of optical waveguides as it will be explained in chapter 2.

1.3.2 Electro-optic effect

The linear electro-optic effect is one of the most important features of lithium niobate crystals. It consists in the variation of the refractive index due to the application of an electric field according to the relation:

$$\Delta\left(\frac{1}{n^2}\right)_{i,j} = \sum_k r_{ijk}E_k + \sum_{k,l} s_{ijkl}E_kE_l + ... \tag{1.3}$$

where $\Delta\left(1/n^2\right)_{i,j}$ is a second-rank tensor describing the change in the relative permittivity. The third-rank tensor r_{ijk} and the fourth-rank tensor s_{ijkl} describe the linear and the quadratic electro-optic effect, usually named *Pockel effect* and *Kerr effect* respectively.
In lithium niobate the Kerr effect can be neglected since the quadratic electro-optic effect has been observed to be significant only under an applied electric filed above 65kV/mm [19]. Due to its symmetry lithium niobate electro-optic linear coefficients can be expressed as a

reduced tensor[1]:

$$r = \begin{pmatrix} 0 & -r_{22} & r_{13} \\ 0 & r_{22} & r_{13} \\ 0 & 0 & r_{33} \\ 0 & r_{42} & 0 \\ r_{42} & 0 & 0 \\ -r_{22} & 0 & 0 \end{pmatrix} \tag{1.4}$$

According to the measurements reported by Bernal *et al.* [20] the values for this coefficients are $r_{13} = 8.6 \cdot 10^{-12}$m/V, $r_{22} = 3.4 \cdot 10^{-12}$m/V, $r_{33} = 30.8 \cdot 10^{-12}$m/V, $r_{51} = r_{42} = 28.0 \cdot 10^{-12}$m/V.

Electro-optic effect is a key-point for integrated optics applications since together with titanium in-diffused waveguides it can be used to realize optical modulators and switches. This characteristic grows the number of possibilities also in optofluidic applications and makes lithium niobate a better choice than other materials such as silica where waveguides are possible but no electro-optic effect is present.

As it will be discussed in 1.3.6 the electro-optic effect, together with the photovoltaic effect, is responsible for the lithium niobate photorefractivity which allows the modification of lithium niobate refractive indices by means of a non-uniform pattern of light intensity.

1.3.3 Piezoelectricity

Lithium niobate exhibits also piezoelectricity since it is possible to induce polarization with applied stress. In particular the induced polarization is:

$$P_i = \sum_{j,k} d_{ijk}\sigma_{jk} \tag{1.5}$$

where σ_{jk} is the second-rank symmetric stress tensor and d_{ijk} is the third-rank piezoelectric tensor. The stress tensor has 6 independent components since $\sigma_{ij} = \sigma_{ji}$. Moreover the crystal symmetry implies a further reduction of d independent components. The results is a piezoelectric tensor with 4 independent components which can be expressed in the

---

[1] The convention $\{jk\} = \{11\} \to 1$, $\{jk\} = \{22\} \to 2$, $\{jk\} = \{33\} \to 3$, $\{jk\} = \{23\}, \{32\} \to 4$, $\{jk\} = \{31\}, \{13\} \to 5$, $\{jk\} = \{12\}\{21\} \to 6$ has been used.

reduced notation as:

$$d_{ijk} = \begin{pmatrix} 0 & 0 & 0 & 0 & d_{15} & -2d_{22} \\ -d_{22} & d_{22} & 0 & d_{15} & 0 & 0 \\ d_{31} & d_{31} & d_{33} & 0 & 0 & 0 \end{pmatrix} \tag{1.6}$$

Piezoelectric crystals exhibit also the converse piezoelectric effect that means they undergo strain under the application of an external electric field. The relation between the external field components and the second-rank stress tensor is:

$$S_{ik} = \sum_i d_{ijk} E_i \tag{1.7}$$

where d_{ijk} are again the components of the piezoelectric tensor. Piezoelectric effect of lithium niobate has been effectively exploited to induce surface acoustic waves (SAW) which has been demonstrated to be useful to move droplets on the surface of the crystal [21] or sort particles in a flowing liquid [22].

1.3.4 Pyroelectric effect

Lithium niobate is a pyroelectric solid which exhibits a change in the spontaneous polarization as a function of temperature. The relation between the change in temperature (ΔT) and the change in the spontaneous polarization (ΔP) is linear and can be written as $\Delta P = \hat{p}\Delta T$ where $\hat{p}$ is the pyroelectric tensor. In lithium niobate this effect is due to the movement of Li and Nb ions relative to the oxygen planes and, since their position is shifted only along the z-axis, the pyroelectric tensor has the form:

$$\hat{p} = \begin{pmatrix} 0 \\ 0 \\ p_3 \end{pmatrix} \tag{1.8}$$

where $p_3 = -4 \cdot 10^{-5} \mathrm{C/m^2K}$ [23] and the negative sign indicates that upon cooling the $+z$ crystal surface will become positively charged.

Pyroelectric effect has been showed to be useful to manipulate micro and nano-droplets by elettrophoresis and trap particles via dielectrophoresis proving another possible application of lithium niobate in the field of microfluidics [24, 25].

1.3.5 Photovoltaic effect

The bulk photovoltaic effect of lithium niobate was discovered in 1974 by Glass *et al.* [26], that observed that a stationary current rises after the crystal was exposed to light. This is an effect typical of non-centrosymmetric crystal by which the momentum of photo-excited electrons has a preferential direction. The result is that a current density $\mathbf{j}_{\mathrm{phv}}$ is generated by illuminating the crystal:

$$j_{\mathrm{phv},i} = \beta_{ijk} e_j e_k^* I = \alpha k_{G,ijk} e_j e_k^* I \tag{1.9}$$

where β_{ijk} are the components of a third-rank tensor called *photovoltaic tensor*, which can be expressed as the product between the absorption coefficient (α) and the Glass coefficient (k_G); e_j and e_k are the polarization vectors of the incident light wave and I its intensity.
In lithium niobate only four components of the photovoltaic tensor are independent: β_{333}, $\beta_{311} = \beta_{322}$, $\beta_{222} = -\beta_{112} = -\beta_{121}$ and $\beta_{113} = \beta_{131}^* = \beta_{232} = \beta_{223}^*$. The generated current density is mainly directed along the optical axis of the crystal since $k_{G,333} = 2.7{\cdot}10^{-9}$cm/V and $k_{G,322} = 3.3{\cdot}10^{-9}$cm/V, while the generated current along the y-axis is one order of magnitude lower (for example $k_{G,222} = 0.3 \cdot 10^{-9}$cm/V).

1.3.6 Photorefractive effect

The photovoltaic effect and the electro-optic effect both contribute to another peculiar phenomenon observed in lithium niobate which is called *photorefractive effect.*
The effect was firstly observed by Ashkin *et al.* [27] when they noted the fanning of a laser beam passing through a lithium niobate crystal and they realized that light was inducing a change in the refractive index of the material. Since this phenomenon was detrimental for their purpose they called it *optical damage.*
The photorefractive effect relies on the presence of intrinsic or extrinsic impurities with two valence states. In fact they add intermediate levels in-between the valence and conduction bands of the pure lithium niobate acting both as donors or acceptors depending on their valence state.
Niobium antisite $\mathrm{Nb_{Li}}$ has this role since it can be found both in the Nb^{4+} donor state

or in the Nb^{5+} acceptor state. The effect is highly enhanced if the crystal is conveniently doped, for example with iron, which presents the Fe^{2+} and Fe^{3+} states.

When a non-uniform light pattern irradiates the crystal, electrons in the highly illuminated areas are excited from the donor level to the conduction band (fig.1.3a). By diffusion, by photogalvanic effect or by drift they are transferred in the dark regions where they are trapped by acceptors (fig.1.3b). This leads to a non-uniform charge distribution and to the rising up of an internal space-charge electric field (fig.1.3c).
The presence of the space-charge electric field changes the refractive index of the material by the above mentioned electro-optic effect and a refractive index pattern is obtained (fig.1.3d).

In the case of Fe doped lithium niobate crystals ($Fe:LiNbO_3$) the phenomenon is described by the one-center charge-transport model proposed for the first time in its complete formulation by Vinetskii and Kukhtarev [28]. The equations describing the charge transport are the following:

$$\begin{cases} \dfrac{\partial N_D^+}{\partial t} = (\beta + sI)(N_D - N_D^+) - \gamma n_e N_D^+ & \begin{array}{c}\text{Excitation-recombination}\\ \text{rate equation}\end{array} \\ \nabla \cdot (\varepsilon_0 \varepsilon \mathbf{E}) = \rho & \text{Poisson equation} \\ \dfrac{\partial \rho}{\partial t} + \nabla \cdot \mathbf{j} = 0 & \text{Continuity equation} \\ \rho = e(N_D^+ - N_A - n_e) & \text{Charge density} \\ \mathbf{j} = -e\mu_e n_e \mathbf{E} - \mu_e k_B T \nabla n_e + s k_G (N_D - N_D^+) I \hat{\mathbf{c}} & \text{Current density} \end{cases} \tag{1.10}$$

where q and N_e are the charge and the density of the carriers respectively, s the photoionization cross section, γ the recombination constant, μ_e the mobility, k_B the Boltzmann constant, T the absolute temperature, k_G the Glass constant, $N_{Fe^{2+}}$ and $N_{Fe^{3+}}$ the densities of filled and empty traps.
The current density is expressed as the sum of three terms due to drift, diffusion and photovoltaic effect respectively.

Photorefractive effect is extremely important in integrated optics applications since it can be exploited to realize holographic Bragg gratings or filters and couple them to waveguides.

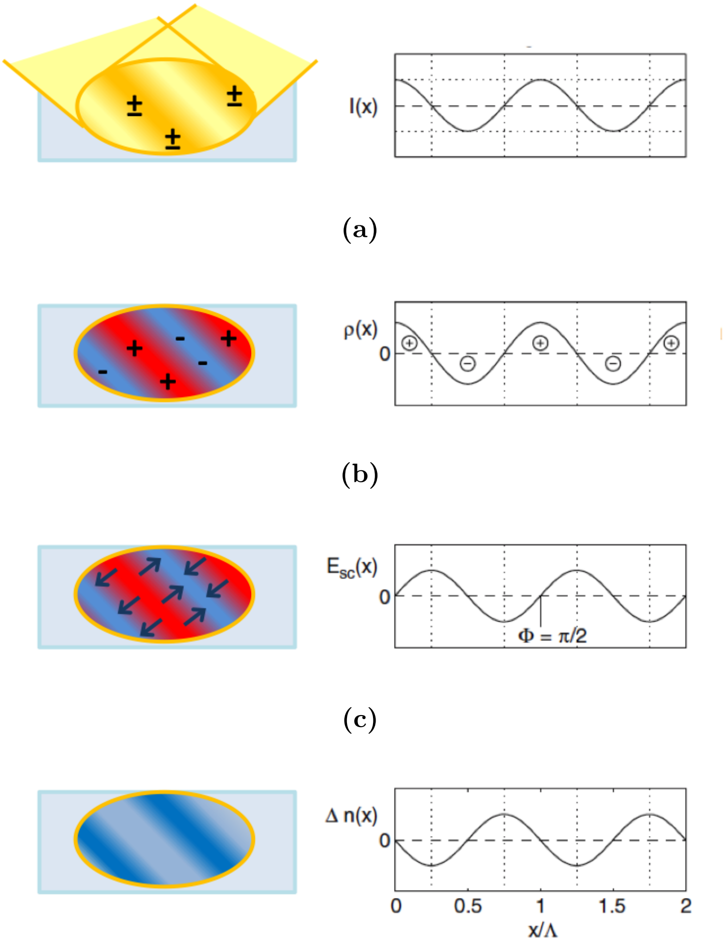

(a)

(b)

(c)

(d)

Figure 1.3: Scheme of the refractive index change building up by photorefractive effect after the illumination by two interfering beams: (a) electrons in the illuminated areas are excited from the donor level to the conduction band; (b) they are transferred by photogalvanic, diffusion or drift current in the dark regions where they are trapped by acceptors; (c) an internal electric field rises up due to the non-uniform charge distribution; (d) the refractive index changes by electro-optic effect due to the internal electric field.

2 Waveguides in Lithium Niobate

2.1 State of the art

Lithium niobate is one of the most popular materials in the field of integrated optics thanks to its very low optical absorption (~0.1dB/cm) in the typical wavelengths employed in telecommunications, around $(1.3 \div 1.55)\mu$m. It is widely used in photonics industry for the realization of waveguides, electro-optical and acousto-optical modulators and switches, nonlinear optical frequency converters and diffraction gratings. This applications are possible due to the material piezoelectric, electro-optic and photorefractive properties (see chapter 1).

Waveguides are the first element of every integrated optical circuit and different techniques are available for their realization in lithium niobate, the most important are:

- **titanium in-diffusion**: it is the most common and studied technique in lithium niobate and it is effectively applied in the realization of integrated optical circuits since the mid-seventies [29–31]. Its wide spread is mainly due to the simplicity and versatility of the fabrication process, to their good light confinement along both the extraordinary and the ordinary axes and to the fact that Ti in-diffused waveguides preserve the electro-optical properties of $LiNbO_3$ [31] allowing for the realization of optical switches and modulators. In fact titanium in-diffusion together with standard photolitographic techniques has been already used to obtain waveguides as well as more complex optical circuits such as modulators, switches, Mach-Zender interferometers and couplers [32, 33].

- **proton-exchange**: PE is another well-known technique for the realization of waveguides. It consists in the immersion of lithium niobate in a liquid source of hydrogen ions at high temperature (150÷400°C) [34]. The refractive index change is due to the substitution of lithium ions (Li^+) from the crystal matrix with H^+ from the liquid phase (usually benzoic acid or toluic acid). In non-linear optics applications a subsequent annealing treatment is performed since it allows achieving a higher resistance to optical damage: this process is referred to as Annealed Proton Exchange (APE). The advantages of this technique are a high refractive index change ($\Delta n_e \approx 0.1$) one order higher than Ti in-diffused waveguides and the easiness of the process. Drawbacks are that only modes polarized on the extraordinary axis are supported and that electro-optical properties of lithium niobate are lost after the proton exchange. Improved techniques able to maintain electro-optical coefficients of lithium niobate are Soft Proton Exchange (SPE) [35] and Reverse Proton Exchange (RPE) although they suffer a lower refractive index change, in the range $0.01 \div 0.03$.

- **ion-implantation**: the damaging of lithium niobate by ion implantation allows for a refractive index change of the order of 0.1. The technique consists in the bombardment of the crystal surface by ions at fixed energy and incidence angle resulting in both the generation of point and extensive defects in the first microns below the surface. Extensive reviews can be found by Chen [36] and Pena-Rodriguez [37]. The employment of a wide variety of ions (H, B, C, O, F, Si, P, Ag) [36, 38] have been reported at different energies (few MeV up to more than 20MeV) and fluencies ($10^{12} \div 10^{17}$ions/cm^2). Depending on the ion energy and mass both electronic excitations and nuclear interactions [39] can contribute to the refractive index change of the material. Post-annealing is usually required to recover optical transparency and get rid of absorption centers generated during the ion implantation process.
  The high refractive index change achievable both in the ordinary and the extraordinary axes and the possibility to obtain 2D patterns by joining beam rastering with photolitographic techniques make this technique appealing although it requires quite huge and expensive facilities.

- **laser writing**: waveguides can be written in lithium niobate both by photorefractive effect and structural modifications after irradiation with a laser beam. The first case was studied by *Itoh et al.* [40], who demonstrated that the refractive index modifications induced by scanning the crystal with a focused laser beam at a wavelength of 514nm and a pump power of 70mW were able to confine light propagating along the ordinary axis and polarized along the extraordinary axis. This technique lead to a considerable increase in n_e of the order of 10^{-3} but they suffer erasure when

enlightened with a sufficiently intense laser beam, specially in the visible range.
On the other hand, a higher power can be employed to impose irreversible structural modification of the crystal structure and obtain a refractive index change as well. Femtosecond laser pulses from a pulsed laser are focused in the region where the waveguide has to be carried out and computer driven step motors move the sample in order to scan the waveguide region [41, 42]. Depending on the energy employed, the effect is a decrease of n_e or both n_e and n_o at higher pulse energies. The guided modes are then localized in between the damaged regions.
The great advantage of this technique is the capability to realize three-dimensional waveguides in the bulk material and to couple them with couplers and diffracting gratings obtained by the same technique [42]. The disadvantage is the poor confinement due to the low refractive index change around $8 \cdot 10^{-4}$.

- **ridge waveguides**: ridge waveguides also can be realized both by mechanical micromachining [43] and chemical etching [44]. The first technique requires computer numerically controlled (CNC) machines operating micro-saws or micro-mills able to ensure optical grade surfaces. On the other hand the chemical approach requires the etching of lithium niobate in a hydrofluoric acid bath which can be favoured by earlier proton exchange [45, 46] or ion implantation in the regions to be engraved.
  Ridge waveguides can be obtained also by more complex techniques like thin films deposition and ion beam micro-milling as in the case of smart guides [47]. Ridge waveguides obviously give the higher confinement due to the high refractive index difference between the lithium niobate core and the surrounding material, but due to fabrication defects can have a higher dispersion than diffused waveguides due to scattering.

In this work the technique employed for the realization of the waveguide was titanium in-diffusion. The reasons for this choice were:

- the need for a high refractive index jump both in y- and z-propagating waveguides for the maximum versatility of the optofluidic device for future applications. Actually among the aims of the research project in which this work is included there is the realization of a phtotorefractive Bragg grating along the waveguide collecting the signal. The grating has the task to reflect the pump wavelength in order to select fluorescence form molecules dispersed in the fluid; since the writing efficiency of the

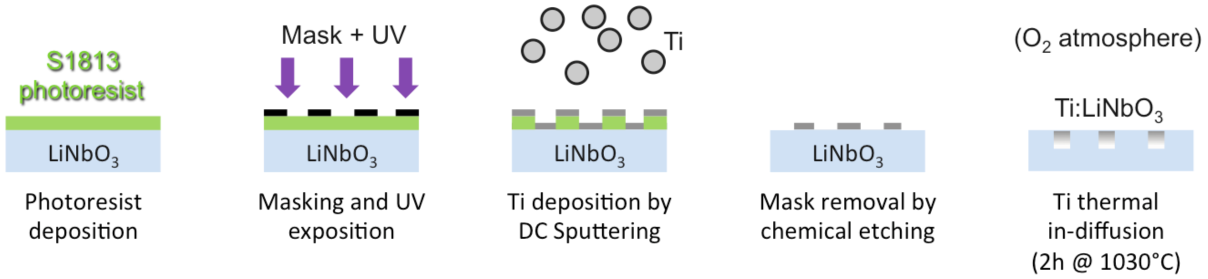

Figure 2.1: Sketch of the main steps for the fabrication of channel waveguides by titanium in-diffusion.

grating by photorefractive effect is order of magnitude higher if the wavevector of the grating is along the extraordinary axis, z-propagating wavelength are preferred; therefore proton exchange was excluded [48];

- the availability of all the facilities needed for the fabrication process (clean room, collimated UV lamp, magnetron sputtering, oven) at the Physics and Astronomy Department of Padova;
- the will to employ, for the realization of the device, techniques highly reproducible and easy to implement in order to facilitate the future technology transfer.

2.2 Titanium In-diffused Waveguides Realization

Channel waveguides were realized by diffusion at high temperature of thin titanium stripes deposited by magnetron sputtering after the sample was masked by standard photolithography.

Before explaining the detailed fabrication procedure it is useful to outline its main steps as also sketched in fig.2.1 as a guideline for the reader:

- a photoresist layer was deposited on the surface of the sample;
- a mask was kept in contact with the photoresist layer while the sample was illuminated with a UV lamp in order to impose degradation of the unmasked regions;
- a titanium thin film was deposited on the patterned surface by sputtering deposition;
- the photoresist layer was removed in a solvent bath in order to leave on the crystal surface only the desired titanium stripes;

- the titanium was diffused into the crystal by high temperature thermal annealing in an oxygen atmosphere.

This scheme is a well-known standard procedure but required several tests to be optimized for the specific available facilities.
Planar waveguides were also realized to prepare the samples for the characterization of the titanium in-diffusion process by Rutherford Back Scattering (RBS) and Secondary Ion Mass Spectrometry (SIMS). The fabrication process of these samples is the same apart from the lack of photolitography steps since a planar titanium film was deposited and diffused on the bare surface of lithium niobate samples at the same conditions of the samples for the channel waveguides.

In the following the detailed steps for the fabrication of channel waveguides are presented.

Samples Cutting. At first the samples were cut with the desired dimensions from a commercial x-cut wafer of congruent lithium niobate from Crystal Technology with a thickness of 1mm and polished on both faces. The cuts were performed with a South Bay 540 cutting machine, equipped with a diamond-coated Cu-alloy blade. The machine was endowed with a graduated protractor to allow for a perfect alignment of the wafer in order to cut the samples along the crystallographic axes.
Each sample underwent a sonicating bath in soap and distilled water, isopropanol and finally acetone for 15 minutes respectively to ensure a clean surface before the sputtering deposition. The cutting of the samples was always performed at the beginning of the procedure during the optimization of the process and when test samples were needed. Nevertheless the final devices were obtained from wafer which underwent the all process before they were cut in smaller samples in order to fasten each single fabrication step and ensure a higher reproducibility.

Photolitography. All the photolitography steps were performed in a ISO 7 class cleanroom financed by the MISCHA project (Microfluidics laboratory for scientific and technological applications).
The photoresist employed was the S1813 from the Microposit S1800 G2 series. It is a positive photoresist engineered to satisfy in particular micro-litography on silicon but it showed to be suitable also on lithium niobate. It was chosen for its compatibility with the emission spectrum of the available UV lamp and for its nominal resolution of 0.48μm, suitable for our purpose.

At first the samples were covered with a primer based on hexamethyldisilizane (HMDS) to favour the adhesion of the phtoresist to oxides. Both the primer and the photoresist were deposited by spin coating at a spin rate of 2000rpm for 30s and 6000rpm for 30s respectively. A mask with patterns of stripes with different widths (5, 6, 8, 10μm) was realized by a specialized company (Delta Mask B.V.). It consisted in a laser patterned chromium layer of 980Å on a plate of Soda Lime glass. After the photoresist deposition the samples were put under the mask, in deep contact with it and exposed to UV irradiation from a highly collimated UV lamp with an intensity of 9mW/cm^2 for 18s. The photoresist was then developed by dipping in a stirred bath of Microposit MF-300 for 60s and then rinsed in a distilled water bath. The quality and the width of the obtained channels were controlled by optical microscopy and profilometry.

Titanium deposition. Sputtering deposition consists in the deposition on the sample surface of atoms which are removed from a metallic or insulating target after bombardment by the ions of a plasma. The process takes place in a vacuum chamber at a controlled pressure and the plasma is sustained by a potential difference between the target and the rest of the chamber. The potential difference can be supplied by a continuous current source or an RF alternating current source, which is mandatory for the sputtering of insulating materials. In the *magnetron* sputtering a magnetic field is also present in the proximity of the target due to permanent magnets. These magnets have the aim to confine secondary electrons coming from the collisions between the plasma ions and the target in order to increase the cationic density in the region of the target and allow for a higher sputtering rate.

The deposition of the titanium film was performed by a magnetron sputtering machine provided by Thin Film Technology. The samples were kept in a cylindrical vacuum chamber at a pressure below $3 \cdot 10^{-6}$mbar, achievable with two subsequent stages: a rotary vacuum pump was used to reach a pressure of $(8 \div 9) \cdot 10^{-2}$mbar and a turbomolecular pump allowed reaching the minimum pressure.

Argon gas was injected in the chamber through a flow-meter at a pressure of $5 \cdot 10^{-3}$mbar to feed the plasma . The titanium target was connected to a DC power source supplying a power of 40W during the deposition. The target was kept covered by a shield during a pre-sputtering time of 3 minutes in order to remove impurities and oxidized layers on its surface.

Normal operation required to put the samples on a sample holder laying at the center of the cylindrical chamber and tilt in their direction the target holder which was positioned out-of-axis. In this way sputtered titanium atoms reached the samples at a certain angle and this feature was found to be detrimental during the lift-off process when channel waveguides have to be realized. Actually this configuration led titanium atoms to impinge on the lateral walls of the channels realized in the photoresist rather than on their bottom. A dedicated sample holder was then designed in order to keep the samples in front of the target and ensure titanium atoms trajectories to be perpendicular to the sample surface.

Lift-off. The photoresist and the titanium deposited on its surface were removed by a bath in the SVC(TM)-14 specific stripper at 60°C for several minutes and then under sonication for few seconds.

Thermal diffusion. The diffusion process was performed in a tubular furnace Hochtemperaturofen Gmbh (model F-VS 100-500/13) by Gero. The sample was positioned on a platinum foil laid on the boat at the end of a quartz rod used to pull them at the center of the oven. The channel waveguides were diffused at a temperature of 1030°C for 2h. The heating and cooling rates were always kept to 300°C and -400°C respectively to avoid excessive thermal stresses of the crystals. Oxygen was fluxed inside the oven chamber at a flow rate of 50Nl/h to reduce surface damage after titanium in-diffusion [49]. Unfortunately wet conditions were not possible with the available set-up so that the optimal conditions reported in literature to avoid lithium out-diffusion were not reached.

Lapping and polishing At the end of the process all samples lateral surfaces were lapped and polished to remove the damages and defects caused by the cutting from the original commercial wafer. The process was carried out with a professional polishing machine by Logitech. The polishing is performed by making the samples laying on a rotating disk. The procedure requires three subsequent steps employing an iron disk wet by an aqueous suspension of 9μm alumina particles, the same disk wet by an aqueous suspension of 3μm alumina particles and finally a polyurethane disk wet by an aqueous suspension of sub-micrometer particles. At the end of the procedure a surface roughness of the order of 1nm is obtained as verified by AFM measurements.

2.3 Titanium diffusion

Titanium in-diffusion is one of the most widely employed techniques for the realization of channel waveguides in lithium niobate, in particular for the fabrication of integrated optical devices [50].
Titanium in-diffusion process was studied in detail in the past and the process was found to go through the following steps:

- $T \sim 500°\mathrm{C}$: titanium is oxidized to $\mathrm{TiO_2}$;
- $T > 600°\mathrm{C}$: $\mathrm{LiNb_3O_8}$ epitaxial crystallites are formed at the surface together with the simultaneous loss of lithium;
- $T > 950°\mathrm{C}$: a $(\mathrm{Ti_{0.65}Nb_{0.35}})\mathrm{O_2}$ mixed oxide source appears and it acts as the diffusion source for titanium in-diffusion inside the bulk crystal.

In general metal diffusion inside oxides from a thin metallic layer is described starting with the well-known Fick's law:

$$\frac{\partial C(x,t)}{\partial t} = \frac{\partial}{\partial x}\left(D\frac{\partial C\left(x,t\right)}{\partial x}\right) \tag{2.1}$$

where $C(x,t)$ is the dopant concentration and the diffusion coefficient D can be dependent on both the temperature T and the concentration C.
The dependence of D on the temperature is usually modeled by an exponential law according to Arrenhius theory: $D = D_0 e^{-\frac{E_a}{k_B T}}$, where E_a is the activation energy.
If D depends on the concentration the solution is not so straightforward with all the possible boundary conditions. An analytical solution in the case of two inter-diffusing semi-infinite alloys was found by Matano in 1932 [51].
In the easier case of D independent of C, two types of analytical solutions of the Fick's equation can be used to describe the diffusion from a thin film at constant temperature. If the film is not completely diffused it can be approximated as an infinite source of dopant because at the surface of the crystal the concentration is constant and equal to the saturation concentration C_s. The solution is described by an error function:

$$C(x,t) = C_s \operatorname{erfc}\frac{x}{\sqrt{4Dt}} \tag{2.2}$$

In the case of a diffusion time much larger than the time needed to exhaust the film, the approximation of the dopant source at $t = 0$ as a layer with negligible width can be made ($C(x, t = 0) \neq 0$ only for $x = 0$) and the solution to the Fick's equation has a Gaussian shape:

$$C(x,t) = \frac{M}{\sqrt{\pi Dt}} \exp\left(-\frac{x^2}{4Dt}\right) = C_0 \exp\left(-\frac{x^2}{4Dt}\right) \tag{2.3}$$

where M is the total amount of dopant deposited in the film and $C_0 \sim \sqrt{t}$ is the concentration at the surface of the crystal at time t. In the case of a titanium in-diffused planar waveguide the general condition to be achieved is that of a completely diffused dopant so that a simple Gaussian can be used to fit the diffusion profile along the surface orthogonal direction as will be shown in the analysis of the SIMS profile in section 2.4.1.

2.4 Experimental Analysis

Titanium in-diffusion in lithium niobate and the fabrication of planar waveguides was deeply investigated by our research group in the past.

During the work for this thesis photolitography, sputtering and diffusion parameters were calibrated for the realization of channel waveguides in the visible range suitable for the employment in the lab-on-chip to be carried out.

In particular the aim was to couple a 632.8nm wavelength Gaussian beam to a waveguide able to illuminate the fluids flowing inside a microfluidic channel with a width of the order of 100μm and another one able to collect the transmitted light. Clearly a high intensity had to be carried by the input waveguide since the light beam has to reach the collecting waveguide several tens of microns ahead. Moreover a good reproducibility of the electromagnetic field exiting the input waveguide had to be ensured for a reproducible response of the optical detection stage.

Although a higher intensity could be coupled in a multi-mode waveguide exciting simultaneously few modes, a single mode waveguide was preferred due to the invariance of the electromagnetic field along the waveguide direction. In this way it was ensured that the profile of the field exiting from the input waveguide was independent of its length and also of the end-butt coupling condition reached at its beginning. In addition, although both y- and z-propagating channel waveguides were fabricated, the second ones were pursued for the final configuration of the optofluidic chip since one of the aim of the project was

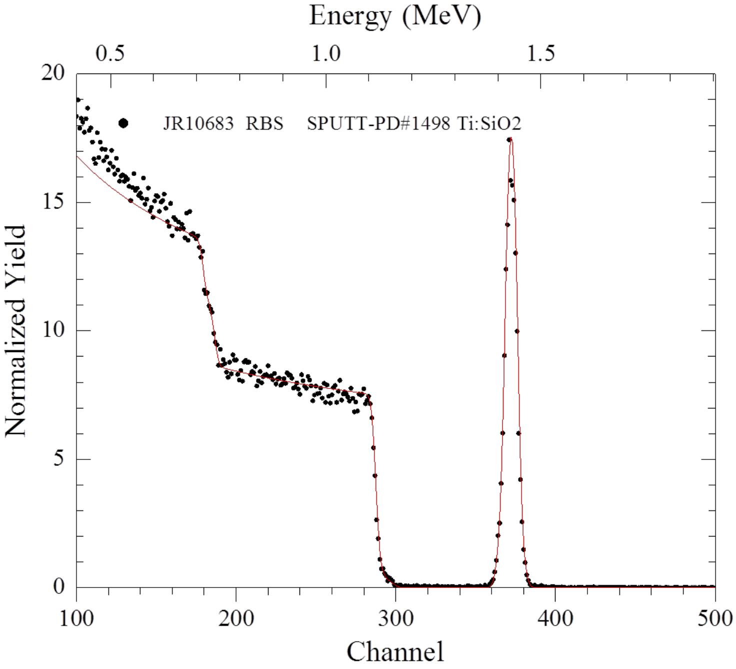

Figure 2.2: RBS spectrum of an as-deposited sample of Ti on a silica (SiO_2) substrate.

the integration of a reflecting Bragg grating on the collecting waveguide by photorefractive effect and this property is highly enhanced if the grating wavevector is directed along the optical axis of the crystal (see section 1.3.6).

In order to find the best experimental parameters for the realization of z-propagating channel waveguides a calibration of the diffusion process was performed by measuring the deposited titanium dose with *Rutherford Backscattering Spectrometry* (RBS) and the diffused profile with *Secondary Ion Mass Spectrometry* (SIMS).
Finally a finite element method simulation was employed to calculate the guided modes.

2.4.1 RBS and SIMS Characterization

RBS was used to measure the titanium surface concentration of the thin film deposited by sputtering. Titanium films were deposited on silica substrates by sputtering technique and then measured at the Legnaro National Laboratories (LNL-INFN). The incident beam was a 2MeV proton beam and the silicon solid state detector was placed at 170° with respect to the incident beam with a detection angle of 1.966mstrad.
In fig.2.2 a typical RBS spectra is reported from a titanium film of (41 ± 5)nm deposited on a SiO_2 substrate at the same conditions used for the final realization of the waveguides.

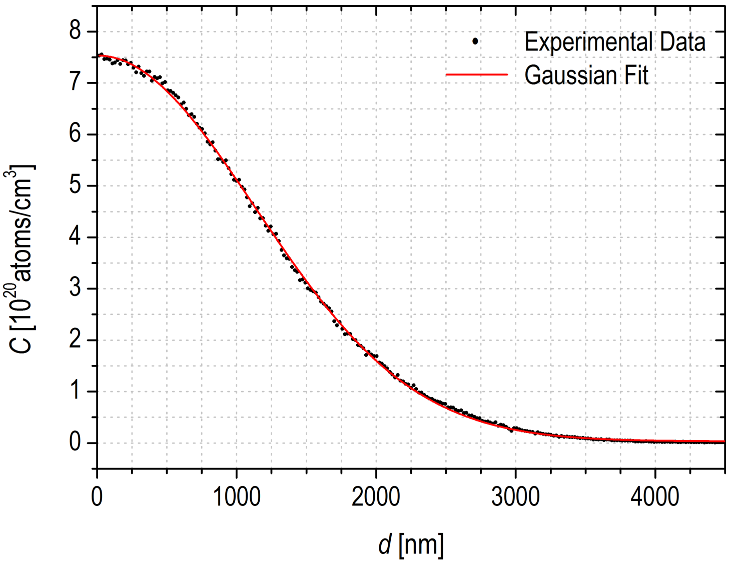

Figure 2.3: Concentration profile obtained from the SIMS measurement of a 37 ± 1nm titanium film on a x-cut $LiNbO_3$ substrate after diffusion in O_2 at 1030°C for 2h.

The Ti peak is sharp due to the very small thickness of the deposited film and it is clearly distinguishable from the background signal due to the backscattering from Si and O atoms, starting at higher and lower energies respectively. The interpolation of the experimental data gave a titanium surface concentration of $150 \cdot 10^{15}$atoms/cm^2 that means a sputtering deposition rate of $(8.3 \pm 1) \cdot 10^{14}$atoms/(cm$^2 \cdot$s) and a titanium concentration in the sputtered film of $(4.1 \pm 0.1) \cdot 10^{22}$atoms/cm^3. From the RBS spectrum it was also deduced that the sputtered layer was partially oxidized, with an approximate composition $TiO_{0.8}$. However this does not affect anyway the diffusion process since during the thermal treatment the titanium film is completely oxidized at a temperature of about 500° before starting in-diffusion.

After the diffusion at 1030°C for 2h, the titanium concentration in the first microns below the surface was investigated by Secondary Ion Mass Spectrometry using a CAMECA ims4f. A 10KV Cs+ primary beam was used to sputter the surface of the sample kept at -4.5kV (so that a final 14.5KeV impact energy was delivered). Negative secondary ions detection was exploited together with electron gun compensation of the charge build-up occurring in insulators.

A typical concentration profile as a function of the sputtered depth is reported in fig.2.3. The profile refers to the diffusion of the titanium film obtained with the same parameters reported for the RBS measurements and diffused at 1030°C for 2h in an O_2 atmosphere.

The profile area was normalized over the total amount of diffused titanium calculated from the RBS spectrum in the verified hypothesis of the complete diffusion of the metallic film during the thermal annealing. From the normalization also the titanium concentration at the surface can be derived and it was found to be $C_0 = (1.06 \pm 0.04) \cdot 10^{21}$ atoms/cm^3.
As discussed in section 2.3, in the hypothesis of a sufficiently long diffusion time the dopant profile has a Gaussian shape. The diffusion coefficient at 1030°C was then calculated from the Gaussian fit of the experimental data as:

$$D = \frac{\sigma^2}{2t} = (89 \pm 2)\mathrm{nm}^2/\mathrm{s} \tag{2.4}$$

where σ is the Gaussian standard deviation.
Both the values for C_0 and D obtained by this calibration were used as parameters in the numerical simulation described in the following section.

2.4.2 Numerical Simulation

A numerical simulation was used to find out the best parameters for the titanium in-diffusion starting from the surface concentration C_0 and the diffusion coefficient D obtained by the joint RBS and SIMS measurements.
The simulation was slightly modified from a model developed by dr. Nicola Argiolas with COMSOL Multiphysics®. The main purposes of the simulation were to state the upper limit of the titanium stripes width to ensure single mode in-diffused waveguides and give the effective refractive index of such a mode.

The simulation software assumes a linear medium ($\mathbf{D} = \varepsilon\mathbf{E}$, $\mathbf{B} = \mu\mathbf{H}$) and time-harmonic oscillation of the electric and magnetic fields ($\mathbf{E}$,$\mathbf{B}$) in order to simplify Maxwell's equations to the following equations:

$$\begin{aligned} \nabla \times \left(\frac{1}{\mu}\nabla \times \mathbf{E}\right) - \omega^2\varepsilon_c\mathbf{E} &= \mathbf{0} \\ \nabla \times \left(\frac{1}{\varepsilon_c}\nabla \times \mathbf{H}\right) - \omega^2\mu\mathbf{H} &= \mathbf{0} \end{aligned} \tag{2.5}$$

where $\varepsilon_c = \varepsilon_r + i\dfrac{\sigma}{\omega\varepsilon_0}$, with ε_r the relative permittivity and σ the electrical conducibility.
If $(\nabla \cdot \mathbf{E}) = 0$ there is no need to solve for the magnetic field ($\mathbf{H} = \frac{1}{i\omega\mu_0}\nabla \times \mathbf{E}$) and using the relation $\varepsilon_r = n^2$ for non-conducting ($\sigma = 0$) and non-ferromagnetic materials ($\mu_r = 1$)

the equation to be solved is:

$$\nabla \times (\nabla \times \mathbf{E}) = k_0^2 n^2 \mathbf{E} \tag{2.6}$$

Assuming a z-propagating waveguide, the z component of the electric field is assumed to be a harmonic function of z so that $\mathbf{E}(x, y, z) = \mathbf{E}(x, y)e^{-ik_z z}$.

The software solves equation (2.6) as an eigenvalue problem with the eigenvalues given by k_z from which the effective indices $n_{\text{eff}} = \omega/k_z$ of the confined modes of the waveguide are derived.

The program was used to simulate the confined modes in a z-propagating waveguide diffused from a titanium stripe of width w on the surface of an x-cut crystal.
The refractive index variation $n(x, y)$ needed as input for the simulation can be expressed as a function of the titanium concentration according to $n_o(x, y) = n_o + K_{n_o} C(x, y)^{\gamma_o}$ or $n_e(x, y) = n_e + K_{n_e} C(x, y)$ [52–54]. The concentration was modeled as the product between a Gaussian profile across the direction perpendicular to the crystal surface (x) and the sum of two error functions on the y direction, as in the case of a diffusion from a finite source of witdh w in one dimension:

$$\frac{C_0}{2} \exp\left(-\frac{x^2}{4Dt}\right) \left[\operatorname{erf}\left(\frac{1}{\sqrt{4Dt}}\left(\frac{w}{2} - y\right)\right) \operatorname{erf}\left(\frac{1}{\sqrt{4Dt}}\left(\frac{w}{2} + y\right)\right)\right] \tag{2.7}$$

where $t = 2$h is the diffusion time, D is the diffusion coefficient calculated from the SIMS measured profile and C_0 is the titanium concentration at the surface obtained from the normalization of the SIMS profile area with the dose measured by RBS.

The results from the simulation are discussed together with the near field images in section 2.5.

2.5 Near Field (NF) Setup and Measurements

In order to measure the near field image of the mode sustained by the waveguides a new experimental setup was built.
The setup is sketched in fig.**??** and includes:

- a laser source from a He-Ne laser at a wavelength of 632.8nm with a nominal power

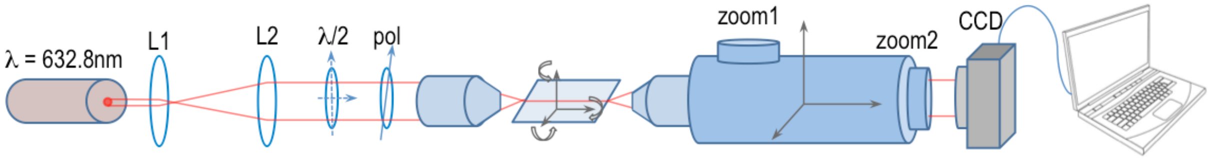

Figure 2.4: Scheme of the near field setup.

of 4mW;

- a half-wave plate and a polarizer to turn and select the polarization of the source in order to excite both the TE or TM modes of the waveguide;
- two confocal lenses used to increase the laser beam width from 1mm up to 4mm, as wide as the entrance pupil diameter of the objective; by this way the beam spot waist at the focus of the objective was minimized;
- a 20× objective to focus the laser beam before the coupling to the waveguide;
- a three-dimensional translational and rotational stage to move the sample;
- a microscope in horizontal position endowed with an objective 20× with a long working distance (1.2cm) and two different zoom levels, moved by a three dimensional translational stage;
- a LaserCam-HR camera by Coherent Inc. to record the near field image.

In the following, to describe the setup it will be used a reference framework with axes oriented on the same directions of the crystallographic directions of a sample with z-propagating waveguides aligned along the focused laser beam. Then z will be the direction of the focused and guided light beam, x the direction orthogonal to the sample surface and, as a consequence, y the axis parallel to the sample surface and perpendicular to the light beam.

Before building up the stage for the motion of the sample, the beam in the proximity of the objective focus was characterized by recording beam profiles at different distances with the camera. The camera sensor can be completely exposed by removing the protection covering so that it can be approximated very near to the objective exiting pupil in order to take images of the beam profile also below the focal length.

Both the projection on the x- and the y-axis of the recorded two dimensional profiles where

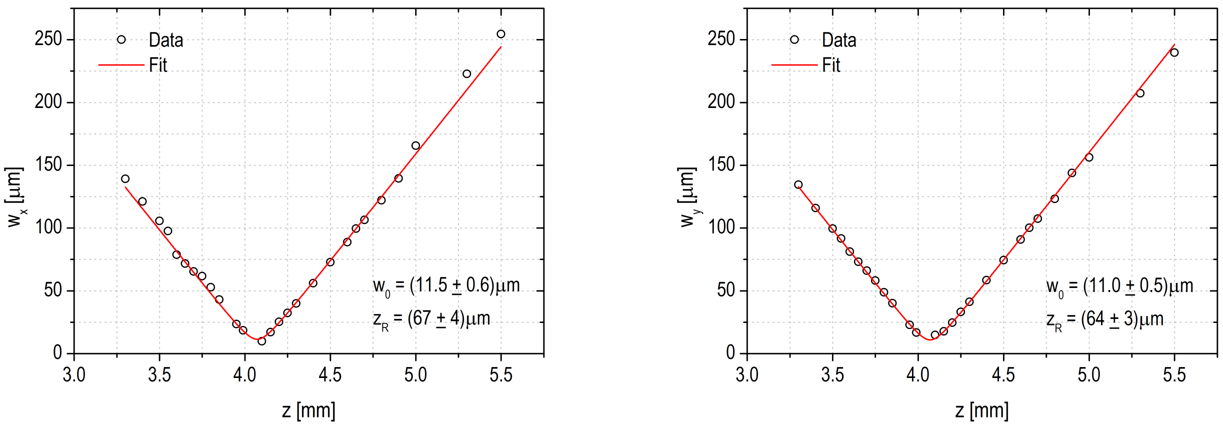

(a) **(b)**

Figure 2.5: Characterization of the Gaussian beam employed to excite the waveguides. The trend of the width of both the projections on (a) the (z,x) and (b) the (z,y) planes as a function of z are fitted by the function of eq.(2.8). The values for the calculated beam waist and the Rayleigh range are reported. Errors are smaller than the markers.

fitted by a Gaussian to calculate the beam width and verify the profile shape.

The trend with the distance from the focus of the beam waist along the two perpendicular directions is shown in fig.2.5. Both data sets were fitted by the function:

$$w(z) = w_0 \sqrt{1 + \frac{z}{z_R}} \tag{2.8}$$

describing the dependence on the distance z from the focus of the width $w(z)$ in the case of a focused Gaussian beam; w_0 is the waist of the Gaussian beam, that means the minimum width it reaches at the focus, and z_R is the Rayleigh range at which $w = w_0\sqrt{2}$.

From the fit, the waist w_0 and the Rayleigh range were obtained and are reported in the plots in fig.2.5. The values obtained from the two different orthogonal projection are perfectly compatible so that we can consider their average as the best estimation. In addition the numerical aperture of the beam can be calculated:

$$\begin{aligned} w_0 &= (11.3 \pm 0.6)\mu\text{m} \\ z_R &= (65.5 \pm 4)\mu\text{m} \\ NA &= \frac{w_0}{z_R} = 0.17 \pm 0.01 \end{aligned} \tag{2.9}$$

The best condition to get the maximum intensity transfer from the laser beam to the waveguide is a perfect match between the two field distributions. This can be obtained by employing an objective with a numerical aperture similar to that of the waveguide and with a beam waist of the same dimensions of the waveguide field distribution.
A precise calculus of the numerical aperture of a graded index waveguide with a asymmetric two-dimensional refractive index pattern as in the case of the titanium in-diffused waveguides is not straightforward. Nevertheless a quite rough estimate of the numerical aperture can be obtained defining an effective numerical aperture NA_{eff} from the maximum refractive index value in the core n_{max} and the refractive index of the cladding n_{clad}, as usually is made for graded index fibers [55]. For a z-propagating waveguide:

$$NA_{\text{eff}} = \sqrt{\frac{n_{max}^2 - n_{clad}^2}{2}} = \sqrt{\frac{(n_o + K_{n_o} C_0^{\gamma_o})^2 - n_o^2}{2}} = 0.13 \tag{2.10}$$

As it can be seen, although the beam waist is quite larger than the waveguide dimensions, the aperture of the employed objective is quite similar to the effective aperture of the waveguide. An objective with a smaller beam waist would have a larger numerical aperture. We preferred to match the numerical aperture rather than the beam waist to reduce the intensity fluctuations due to small translational mismatching.

The described setup was employed to measure both y- and z-propagating waveguides of different widths during the study for the optimization of the fabrication process. Here the results on the z-propagating waveguides needed for the aim of this work are presented.
Waveguides obtained from stripes of different width were realized and their near field image recorded. As can be seen in fig.2.6, depending on the nominal width of the stripes, multiple or single mode waveguides were obtained. The comparison with the results from the simulation shows that the number of modes is respected.

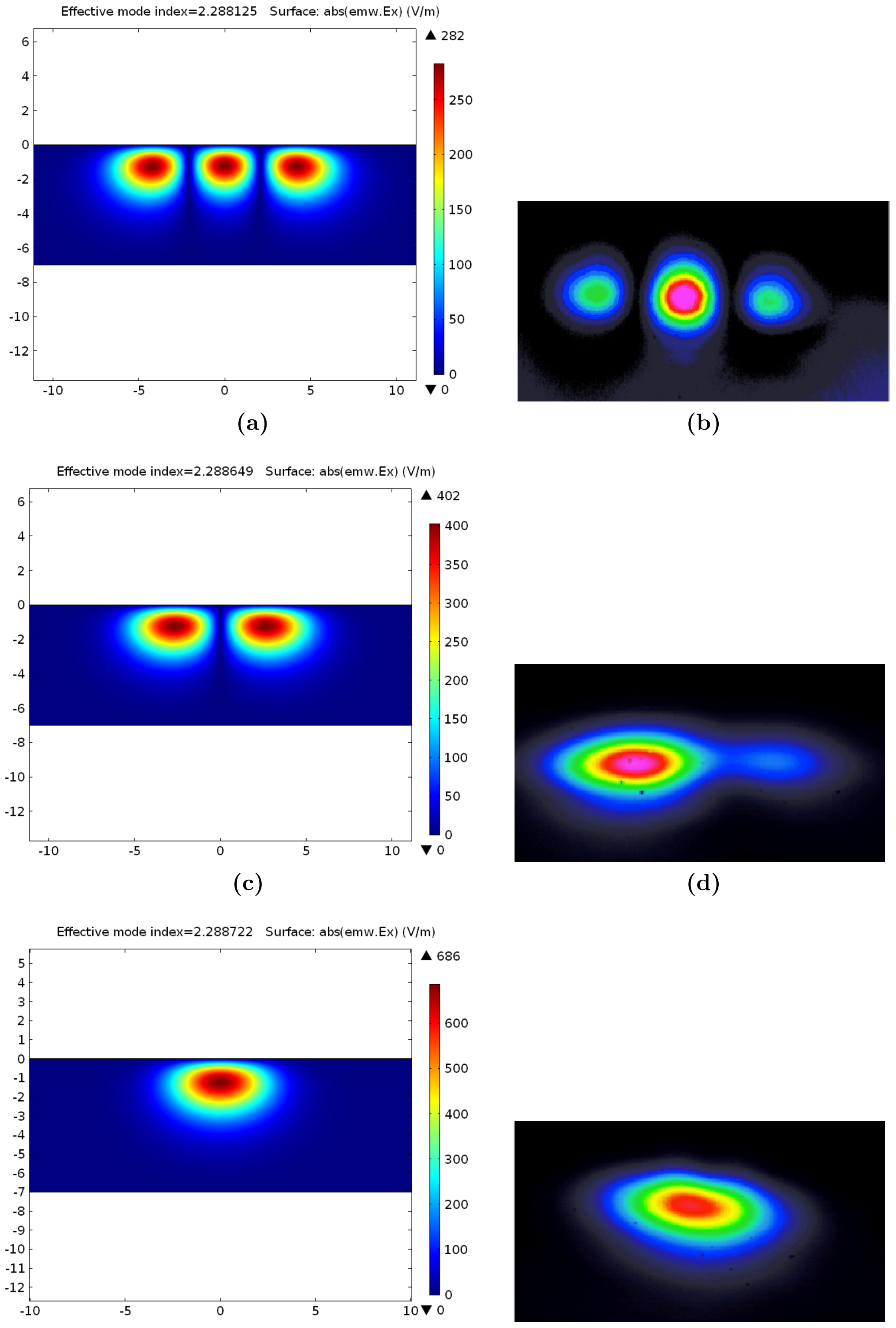

(a) (b)

(c) (d)

(e) (f)

Figure 2.6: Example of characteristic TE modes predicted by the simulation and measured with the near field setup, for waveguides of different nominal widths: (a), (b) 11.5μm, (c), (d) 10μm, (e), (f) 5μm. The images from the simulation show the electric field modulus, thus modes of order higher than the first do not perfectly match the simulated modes since the intensiity distribution depends on the waveguide length. In addition end-butt coupling makes difficult the excitation of a single mode and then near field images may represent a composition of different modes.

3 T-junction Droplet Generators for Lab-on-Chip Devices

3.1 The new age of Microfluidics

Microfluidics is the science studying the behavior of extremely small amounts of fluids with volumes from tens of nanolitres down to picolitres flowing inside confined geometries with a characteristic length of the order of tens of micrometres or less.

The first microfluidic technology was developed in the early 1950s when efforts to dispense small amounts of liquids in the nanolitre and picolitre range were made [56], providing the basis for today's inkjet technology [57]. A deeper interest on small amounts of fluids driven along tiny structures rose up in the 1980s when researchers tried to apply micromachining technology inherited from silicon microelectronics to the realization of microfluidic channels. After capillarity force was used for the realization of the first miniaturized gas chromatograph (GC) by Terry *et al.* on a silicon wafer [58], other devices were obtained exploiting the advantages of microfluidics and efforts were spent to realize several microfluidic structures, such as microvalves and micropumps [59, 60].

Nevertheless the actual boom of microfluidics started in the 2000s, when polymeric materials allowed to realize very easily prototypes of microfluidic devices at a reasonable cost [61, 62].

In the last years a renewed interest in more expensive materials such as silicon or glass is growing due to the need of devices able to avoid swelling, nonspecific bioadhesion and degradation problems of polymer based chips and to support both microfluidic stages and optical or electronical ones [63, 64].

Since its birth microfluidics has been employed in a plenty of applications ranging from chemical synthesis to information technology, from biological analysis to drug delivery. The reason for such a success relies on the fact that microfluidics provides an extremely steady control on the manipulated samples and a very low reagents consumption. Nevertheless it allows high throughput and parallelization reachable increasing the complexity of the devices without a significant increase in the device overall size.

The very small size of the channels in the usual range of flow rates employed lead to low Reynolds number[1] ($\mathrm{Re} < 100$) and then to laminar flow as well as typically large values of Peclet number[2] (measuring the ratio of the convective to diffusive transport): this is the key-path to get high control both in space and time over the transport of chemical or biological spiecies [65–67].

These are the main bricks at the basis of Lab-on-Chip (LOC) technology, the more promising field of microfluidics which has the aim to transfer all laboratory operations into small portable microfluidic devices.

The microfluidic channels of these devices are usually made of polymeric materials such as PDMS or PMMA and obtained by moulding on masters realized by photolitographic techniques [61, 62]; less often they can be realized by chemical etching, laser ablation, micromachining (or a combination of these techniques) on stiffer materials such as silicon or glass. Polymers are preferred since they are easier to shape and they are almost inexpensive. On the other hand silicon and glass, although more expensive, can offer more stable chips at high pressure conditions and above all they are more and more durable since they don't suffer deterioration like polymer materials. The employment of new materials for microfluidcs seems to be a challenge for recent research and many efforts have been spent espescially towards the applicability in biology and medicine and to the integration of multiple stages able to perform multiplexed analysis on liquid samples. In particular many micro-devices have been already realized, able to pull the fluids inside the channels, to manipulate small amounts of liquids, to mix and merge them, to catch and sort particles dispersed in the fluids, to perform analyses of diluted species and many others, but it is still a challenge the integration of all these stages in order to realize a single multi-purpose micro-device which gets rid of all external macro add-ons needed to make up for the lack of micro-technology solutions. In fact what is hardly highlighted in microfluidics applications is that although a plenty of micro-devices manipulating nanolitres droplets have been

---

[1] $\mathrm{Re} = \dfrac{\rho u L}{\mu}$, where ρ is the density of the fluid, u is its mean velocity, L is the characteristic linear dimension of the flow and μ is the fluid dynamic viscosity.

[2] $\mathrm{Pe} = \dfrac{Lu}{D}$, where L is the characteristic linear dimension of the flow, u is the mean velocity and D the mass diffusion coefficient of involved species.

realized, they usually need macro syringe pumps or pressure controllers to operate, or even there exist awsome devices treating biological samples but finally the analysis is carried out putting the chip under the objective of a "big" microscope.

In this thesis the very first attempt of realizing a fully integrated opto-microflduic platform on lithium niobate is presented and the complete integration on the same material of a microfluidic stage with an optical stage for droplet analysis is shown. This is a first step towards the integration of all desirable stages in a single micro-device since lithium niobate has been already showed to be suitable for the realization of pumping micro-systems [21, 68, 69], fluid manipulation devices [70, 71] and optical circuits [72] and in addition it is biocompatible [73].

3.1.1 Droplet Microfluidcs

At the early birth of microfluidics the perspected possibility to perform typical laboratory operations inside a microfluidic chip came up against the peculiarities of fluid flow inside microchannels.

The Reynolds number of such devices is typically very low, always below 100, due to typical fluid velocity that usually doesn't exceed the order of 1m/s and characteristic dimension of microfluidic channels normally ranging from 10μm to 300μm. The typical regime of microfluidics experiments is the laminar flow and this actually makes molecular diffusion the only way for mixing different fluids. This process is quite slow across typical distances of a microfluidic channel and so performing fast reactions inside a microfluidic chip is not achievable.

Moreover laminar flow together with the particular boundary conditions due to the constraint of zero fluid velocity at the solid walls of the channels leads to parabolic velocity profiles. The resulting velocity gradient along the direction perpendicular to the flow gives rise to axial dispersion of the injected liquid compounds and so to poor control on the concentrations of flowing reagents.

These difficulties started to be overcome at the beginning of this century thanks to the advent of droplet based microfluidics. The main idea is to confine the fluid of interest (containing chemical reagents, molecules or biological samples) inside droplets surrounded by another immiscible fluid phase used to carry droplets along the microfluidic channels. The fluid that makes up the droplets is generally called *dispersed phase* while the outer

fluid surrounding the droplets is indicated as *continuous phase.*
The main advantages of this approach are the following:

- if reactants are not soluble in the carrier liquid phase they are kept inside droplets and cannot diffuse through the liquid-liquid interface so that they can be conducted along the channels without losses or dispersion. Therefore droplets can either be used as isolated chemical reactors improving the safeness and monitoring of chemical reactions or as carriers of biological samples such as single cells [74], in order to obtain fast parallelization of biological essays;
- droplets can both be kept separated or merged, so both avoiding or allowing reactions and mixing [75–77];
- the flow profile inside a droplet moving along a channel promote mixing and reactants convection ensuring the uniformity of reactants concentration and making reactions faster [78];
- it has been demonstrated that droplets can be driven, manipulated and sorted by different methods employing particular channel geometries [79, 80], mechanical actuators [81], electric fields [82–84], acoustic waves [68], optical beams [71, 85, 86]. Therefore parallel processing and logical operation are possible [75].

These peculiar features of droplets have made microfluidics effectively employable in a broad range of applications. Among the most interesting and promising examples it has to be cited the chemical synthesis [87], the manipulation of single cells or DNA [74, 88] and drug delivery and screening [89, 90].

3.2 Techniques for generating droplets

A very wide variety of techniques have been developed to produce droplets inside microfluidic chips fitting different needs for different applications. What is common for all of them is the fundamental requirement for high reproducibility and very low dispersion in volume distribution. Other common targets to be achieved by the realization of a droplet generator are a high production frequency, the possibility of produce steady droplet in a wide range of volume, the versatility deriving from the possibility of employing the same device with different liquids and the simplicity of its usage.

A first distinction among the methods to generate droplets can be made between *passive* methods and *active* methods. The first ones are based merely on the interaction between two immiscible fluids constrained in a confined geometry and the separation of the dispersed phase into droplets doesn't require any contribution from energy sources other than those needed to make the fluids flow inside the channels. The size of droplets is tailored just by the control of inlet fluxes or pressure of the injected fluids.

These methods rely on an accurate geometrical design of the microfluidic channels, on a suitable choice of the fluids employed and on the selection or tailoring of the wettability properties of the employed materials. They constitue the simplest way to produce droplets with an extremely sharp volume distribution which can be controlled by changing the fluxes of both the dispersed or continuous phases.

On the other side active methods involve the exploitation of an external source of energy able to induce the formation of droplets. In the last years many techniques have been developed in order to provide the energy needed to the increase of surface during the formation of droplets from the dispersed phase. An incomplete list includes the employment of mechanical actuators such as valves [91], of external electric fields [92,93], of focused laser beams [94], of piezoelectric actuators [95], of pyroelectric materials [25]. These techniques usually allow a faster response in tailoring the droplets size than passive methods and sometimes give the possibility to generate droplet on demand [96, 97], but they are not always easily realizable on the same substrate where the microfluidic channels are engraved and obviously they require more sophisticated technologies and higher costs, so passive methods are often preferred.

In the following a more detailed description of passive methods will be presented while active methods will not be mentioned since not applied in this research. However it worth mentioning that one of the most interesting perspective of the employment of lithium niobate as a substrate for microfluidics is indeed the possibility of a complete integration of a large class of active methods to generate and manipulate droplets. In fact lithium niobate is a piezoelectric material and has already been used as an external source of surface acoustic waves in microfluidic chips based on polymeric materials [21, 69, 70]; as explained in chapter 2, it is also one of the best substrate to realize optical stages which could be used to interact with droplets [94]; electrodes can be easily realized on its surface by joint photolitography and metal evaporation to exploit its electro-optic, piezoelectric and pyroelectric properties [72]; tailorable electric fields can be also obtained after the formation of a space charge distribution by laser beam irradiation thanks to the photorefractive effect and it has already been shown that these fields can be used to manipulate droplets [12,71].

All type of passive methods require the control either on the fluxes of the continuous phase (Q_c) and the dispersed phase (Q_d) or on their inlet pressure (p_c and p_d). Ususally the flux is controlled by employing a syringe pump for the injection of fluids; on the contrary pressure regulators can be employed for a pressure-controlled experiment.

The most important feature of a passive droplet generator is the geometry of the channels near the region where droplets are produced. Thus a first classification of droplet generators can be made on the basis of the nature of flow field near pinchoff as sketched in Fig.3.1:

- *co-flowing*: the device geometry is characterized by two coaxial channels; the dispersed phase flows in the inner channel and when the channel interrupts it emerges into the continuous phase stream which is parallel to the dispersed phase flow. After an initial stage where the two phases flow together, droplets are generated by Rayleigh-Plateau instability. This technique is one of the first methods proposed to generate monodispersed liquid droplets in liquid [98] but soon it has been replaced by the similar but more stable and controlled flow focusing configuration;

- *flow focusing*: dispersed and continuous phase are forced into a narrow region in the microfluidic device and the continuous phase shrinks simmetrically the dispersed phase until pinchoff is reached. The advantages of this geometry are the high stability over a wide range of droplet production frequency (standard microfluidic chips reach frequencies of the order of 1kHz). Although this technique requires a higher fabrication complexity respect to the other passive methods it is the most used and it has been the most studied. However its operational principle is mainly driven by shear stress and the volume and frequency of produced droplets depend on many parameters related to fluid properties (for example viscosity ratio $\lambda = \mu_d/\mu_c$) so it is more difficult to provide a prediction for an all-purpose chip where different fluids could be employed.

- *cross-flowing*: the inlet channel containing the dispersed phase crosses at a wide angle the main channel where the continuous phase is flowing; in this case the dispersed phase obstructs the channel shrinking the continuous phase stream before droplet break-up takes place. Different geometries have been studied such as T-junction, Y-junction, multiple junctions. [99–101]

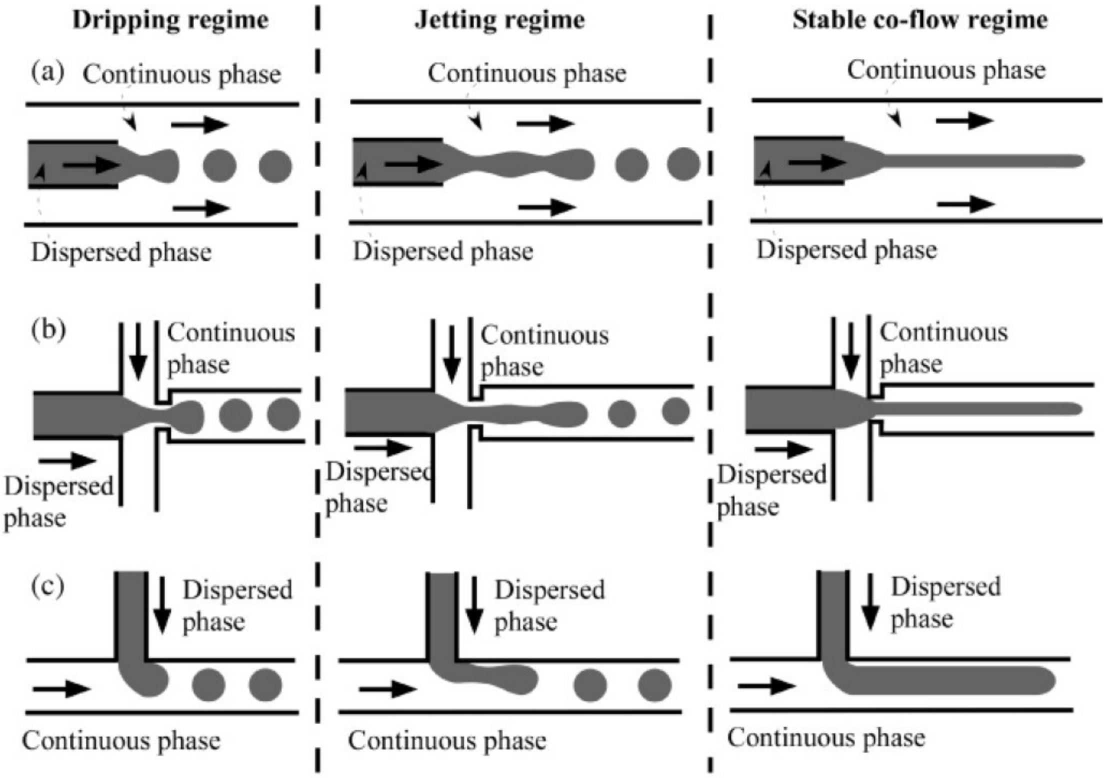

Figure 3.1: Representative sketch of three passive droplet generator types: (a) *co-flowing*; (b) *flow-focusing*; (c) *cross-flowing*. The three different typical operational regimes are shown from left to right: *dripping*, *jetting* and *coflow* regimes.

In general, in each of these geometries, size and frequency of droplets may depend differently on the densities of the injected fluids (ρ_c and ρ_d), on their viscosities (μ_c and μ_d), on their interfacial tension (σ), on the flux of the continuous and dispersed phase (Q_c and Q_d), on their wettability properties and so on their contact angle with channels surfaces (θ_c and θ_d). Depending on these parameters all the previously mentioned geometries can operate in three different regimes (Fig.3.1):

- *co-flow*: the two phases flow parallel to each other and no droplet are formed; this is the case when fluids velocities are small, interfacial tension is high and fluids have similar viscosities. In the particular case of cross-flowing geometry this regime can be favoured by a high wettability of both continuous and dispersed phase on the wall of the channels, this is why a wetting continuous phase and a non-wetting dispersed phase are preferred to produce droplets;

- *jetting*: after an initial co-flowing thread the dispersed phase starts to suffer a growing

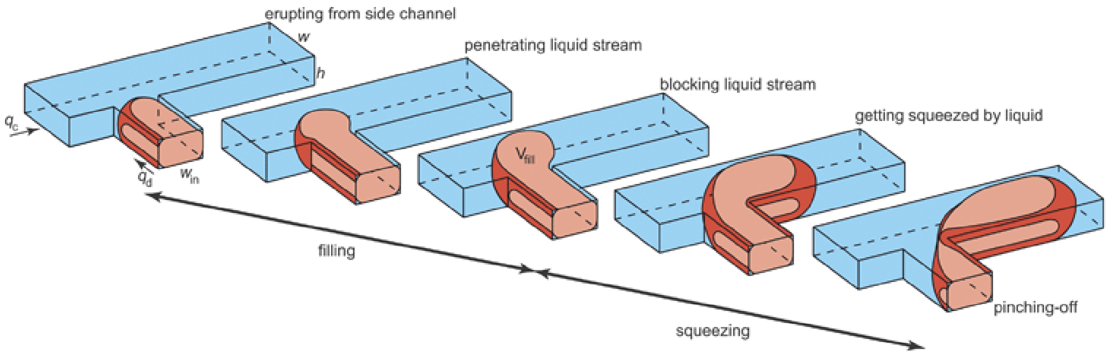

Figure 3.2: Sketch of the different stages of the droplet generation in a T-junction operating in the *squeezing* regime: at first the emerging tip fills the main channel blocking the flow of the continuous phase; then the increasing pressure upstream of the junction shrinks the neck of the dispersed phase until the breakup takes place.

instability which results in the break-up and the formation of droplets; this regime allows a very fast production of small droplets but suffers a wider volume dispersion;

- *dripping*: this is the most studied regime since in the majority of the devices it gives the possibility to produce monodisperse droplets at a high frequency; the leading force in the break-up is the viscous force exerted by the continuous phase on the dispersed phase;

In cross flowing geometries and, in particular, in a T-junction another regime is possible when the dispersed phase obstructs the main channel before break-up occurs (Fig.3.2). This regime is called *squeezing* regime and it can be obtained at a low flux of the continuous phase. It allows for the production of larger droplets also indicated as *plugs*, which fill entirely the main channel.

Since in the present work one of the aims is to illuminate the droplets with a waveguide placed in the upper limit of the channel, plugs are preferred on droplets and then the squeezing regime in a T-junction geometry will be the central topic of this research.

3.3 T-junction

The characteristic geometry of a T-junction consists in a microfluidic channel perpendicularly crossed by another channel which interrupts at the cross. Usually the continuous phase is injected through the first one, also called the main channel, while the dispersed phase comes from the second branch.

In most cases both channels have the same heigth h in the out-of-plane direction but they may have different widths which are normally set depending on the desired droplet dimension. In the following they will be indicated as w_c and w_d for the continuous and the dispersed phase channel respectively. Usually syringe pumps are used to inject fluids inside the channels in order to finely control the volume rates Q_c and Q_d of both phases; sometimes pressure controllers are employed and in this case flowmeters are added downstream to have a feedback on the actual injected fluxes.

Droplets are produced thanks to the forces exerted by the continuous phase on the dispersed phase entering the main channel. Since the dispersed phase starts to occupy a portion of the channel, the continuous phase is kept to flow in a narrower gap so it starts to flow faster and the pressure drop across the tip and the neck of the entering thread grows gradually. The effect is an increase both in the shear force, which is proportional to the continuous phase velocity, and the force driven by the pressure drop across the emerging droplet. The process concludes with the overcome of these forces on the capillary force tending to keep the droplet attached to the dispersed phase thread so that the final result is the droplet break-up (Fig.3.2).

The mentioned regimes of *dripping* and *squeezing* normally used to produce droplets are characterized by a different balance between the mentioned forces and, in particular, in the first one the main contribution to droplet pinch-off is given by the shearing viscous force while in the second one the break-up is driven by the pressure drop between the tip and the neck of the dispersed phase thread, since it obstructs the main channel increasing the resistance to the flow of the continuous phase. An important parameter to distinguish between different regimes in microfluic confined geometries is the capillary number:

$$\mathrm{Ca} = \mu_c u_c / \sigma$$

where μ_c and u_c are the viscosity and the average velocity of the continuous phase respectively and σ is the interfacial tension. Ca expresses the ratio between viscous shear stress and capillary pressure. Greater is Ca and higher will be the contribution of viscous shear forces on the separation of the dispersed phase, smaller is Ca and more important will be the role of other mechanisms opposing to the capillary force which acts to avoid the increase of the dispersed phase surface.

3.3.1 Theoretical Model for the T-junction

The study of liquid fluid flow generally moves from the hypothesis of continuum, that means fluid is considered as a continuum and all considered volumes have characteristic length much greater than the mean distance between molecules. All domain boundaries are given as sharp boundaries, neglecting molecular diffusion of a phase into another one so that, in three dimensions problems, boundaries are two dimensional surfaces. Molecular interactions are neglected and their effect is taken into account by capillarity, expressed as a surface tension force.

The flow of a single newtonian incompressible fluid[3] is described by the well-known Navier-Stokes equations together with the continuity equation:

$$\frac{\partial \mathbf{u}}{\partial t} + (\mathbf{u} \cdot \nabla)\,\mathbf{u} + \frac{1}{\rho}\nabla p = \frac{\mu}{\rho}\,\nabla^2\mathbf{u} + \mathbf{f} \tag{3.1}$$

$$\nabla \cdot \mathbf{u} = 0 \tag{3.2}$$

where $\mathbf{u}$ is the fluid velocity field, ρ is the density of the fluid, μ is the viscosity, p the pressure and $\mathbf{f}$ expresses the external forces acting on the fluid (for example $\mathbf{f} = \mathbf{g}$ to account for gravity).

In the case of microfluidics Reynolds number is very low (usually $Re \lesssim 1$) thus inertial forces can be neglected.

Moreover also gravity can be neglected in confined geometries since usually its contribution is negligible respect to that exerted by viscous forces.

For the case of a single fluid flow no-slip conditions are usually set at the boundaries: $\mathbf{u} = \mathbf{u}_{\text{wall}}$, that means the fluid flows at the same velocity of the boundary wall.

The case of two-phases fluid flow is more complicated: even supposing that $\rho_1 \approx \rho_2$ so that buoyancy can be neglected, viscosities μ_1 and μ_2 could be different and the moving interface between the fluids has to be taken into account.

The Navier-Stokes equations will be valid for both fluids separately inside their domain but more complex boundary conditions have to be formulated. A widespread alternative

---

[3] For a Newtonian fluid the stress tensor τ is assumed to be a linear function of the rate of strain $\varepsilon = \frac{1}{2}\left(\nabla\mathbf{u} + (\nabla\mathbf{u})^T\right)$; in the case of an incompressible fluid that means $\tau = 2\mu\varepsilon$.

The hypothesis of incompressibility states that $\rho(\mathbf{x}, t) = \rho$, from which the continuity equation $\frac{\partial \rho}{\partial t} + \nabla \cdot (\rho\mathbf{u}) = 0$ simplify to $\nabla \cdot \mathbf{u} = 0$.

formulation is to pose the two-phase flow problem on the whole domain occupied by both liquids providing that the viscosity μ will have a discontinuity located at the boundary Γ beetween the two phases (and similarly ρ if $\rho_1 \neq \rho_2$). The interfacial tension σ enters as a forcing term of the form $\mathbf{f}_\sigma = \sigma\kappa\mathbf{n}\delta_\Gamma$ which presents again a discontinuity (κ is the curvature of the interfacial surface):

$$\frac{\partial \mathbf{u}}{\partial t} + (\mathbf{u} \cdot \nabla)\,\mathbf{u} + \frac{1}{\rho}\nabla p = \frac{1}{\rho}\,\nabla \cdot (2\mu\varepsilon) + \sigma\kappa\mathbf{n}\delta_\Gamma \tag{3.3}$$

$$\nabla \cdot \mathbf{u} = 0 \tag{3.4}$$

Solving these equations can be done by complex numerical simulations such as lattice Boltzmann (LBE) [78, 102, 103], volume of fluid (VOF) [104], or computational fluid dynamics methods (CFD) [105] but this techniques imply huge calculations to be solved for each set of geometrical and physical properties of the case of study.

On the contrary simple scaling laws able to provide in advance the droplet volumes and production frequency of a droplet generator would be preferred for a faster planning of microfluidic chips. Nevertheless simpler laws could provide a deeper understanding of physical principles involved in two-phase cross-flow at the microscale. Since the first years of this century both experimental measurements and computer simulations have been explored to give an answer to this question but a unique simple formulation able to predict droplet size and frequency still lacks. In the following the main theoretical models proposed in the past on the scaling laws describing the production of droplets in the T-junction geometry are outlined as a base for the discussion of the experimental results presented in chapter 5.

The first attempt to give a physical explanation to the scaling behavior of droplet volume was provided by Thorsen *et al.* [99] who suggested that droplets are sheared off from the stream of the dispersed phase with a size determined by the competition between Laplace pressure approximated as $p_L \approx 2\sigma/r$ where r is the characteristic radius of curvature of the liquid-liquid interface, and the shear stress force acting on this interface which can be expressed as $\tau \approx 2\mu_c u/\varepsilon$, where ε is the characteristic radius of the gap between the dispersed phase entering the channel and the channel wall. Equating this two contributions an estimation of the characteristic size of a droplet can be readily obtained as $r \approx \sigma\varepsilon/\mu_c u$. A deeper insight on the squeezing regime was provided by Garstecki *et al.* [100] who disproved the model of Throsen showing that a considerable change in the continuous phase viscosity doesn't lead to a proportional change in the size of the droplets. They proposed a finer calculation of capillary pressure and viscous shear stress as well as an additional pressure term (sometimes called the *squeezing pressure*) due to the resistance to flow of the continuous fluid squeezed by the arising tip of the dispersed phase. The analysis on the order of magnitude of these terms led them to conclude that the squeezing pressure is the leading term able to overcome the capillary pressure in the droplet break-up. They also were the first to indicate the capillary number as the parameter to distinguish between the squeezing and dripping regime. This distinction was confirmed by the simulation performed by De Menech *et al.* [106] who set the critical separation value at $\mathrm{Ca}^* = 0.015$: at higher values of Ca the droplet breakup is dominated by the viscous shear stress and smaller droplets are produced, while at lower Ca the viscous shear stress tends to be negligible respect to the squeezing pressure and the generated droplets occcupy the entire width of the channel.

Finally Garstecki postulated a scaling relation for the droplet length along the stream direction in the case of squeezing regime supposing that during a first step the droplet fills the main channel reaching a length equivalent to the width w_c while the neck of the tip continue to occupy the entire width of the channel of the dispersed phase. After the emerging fluid completely obstructs the channel it is pulled by the continuous phase for a time t_{squeeze} needed to shrink the droplet neck until breakup. The velocity the neck shrinks at was estimated to be the average velocity of the continuous phase (u_c) so that $t_{\mathrm{squeeze}} = w_d/u_c = w_d w_c h/Q_c$ and the additional length got by the droplet during this time is $L = w_d Q_d/Q_c$. Consequently, the total length of a generated droplet rescaled by the width of the main channel can be expressed as:

$$L/w_c = 1 + \alpha \frac{Q_d}{Q_c} \tag{3.5}$$

where the coefficient α should be w_d/w_c but the authors left it as a fitting parameters to account for the fact that part of the continuous phase flows through the gutters suorronding the plug and this results in a partial reduction of the pressure upstream of the droplet.

This postulated relation was justified on a theoretical basis and extended to an intermediate squeezing-to-dripping regime by Christopher *et al.* [1]. They considered an emerging dispersed phase thread as sketched in Fig.3.3: the tip is depicted as a spherical shape with radius b connected to the dispersed phase by a neck with a width s which is $s = w_d$ at the beginning of the process.

Starting from an analysis similar to that of Garstecki on the forces involved in the breakup process they derived a scaling law for the droplet length. The involved forces acting on the liquid-liquid interface are:

- the capillary force given by the difference between the Laplace pressures at the upstream and the downstream ends of the emerging droplet multiplied by the projected area of the emergin interface bh:

  $$F_\sigma \approx \left[-\sigma\left(\frac{2}{b}+\frac{2}{h}\right)+\sigma\left(\frac{1}{b}+\frac{2}{h}\right)\right]bh = -\sigma h \tag{3.6}$$

  where the average curvature at the upstream end of the droplet is calculated as the sum of the curvature in the plane of the T-junction $\frac{2}{b}$ and the curvature in the out-plane section $\frac{2}{h}$. Similarly the curvature at the downstream end of the dispersed phase tip is given by the sum of an approximated curvature $\frac{1}{b}$ somehow smaller than the curvature of the advancing tip and the same curvature on the out-plane section $\frac{2}{h}$.

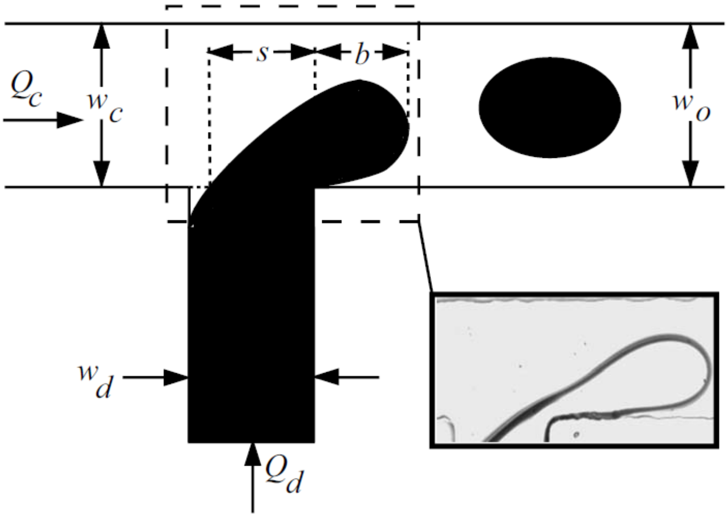

Figure 3.3: Schematic diagram of the emerging droplet according to the model of Christopher *et al.* [1]. The droplet emerges until it reaches a length b and a neck thicknesss s, as measured from the downstream corner of the T-junction. Cross-flow of the continuous phase liquid then forces the droplet neck to thin, during which time the droplet continues to grow due to injection of the dispersed phase liquid.

- the drag force due to the viscous shear stress applied on the emerging interface:

$$F_\tau \approx \mu_c \frac{\partial u}{\partial y} bh \approx \mu_c \frac{u_{gap}}{w_c - b} bh \approx \mu_c \frac{Q_c b}{(w_c - b)^2} \tag{3.7}$$

  where the shear stress rate has been approximated by the average velocity of the continuous phase in the gap between the liquid-liquid interface and the wall of the channel divided by the gap $w_c - b$ between the wall and the tip.

- the squeezing pressure force obtained from a lubrication analysis [107] for the pressure-driven flow in a thin gap with aspect ratio $(w_c - b)/b$:

$$F_p \approx \Delta p_c bh \approx \frac{\mu_c u_{gap}}{w_c - b} \frac{b}{w_c - b} bh = \frac{\mu_c Q_c b^2}{(w_c - b)^3} \tag{3.8}$$

During the growth of the droplet, while b is approaching w_c, the viscous shear stress and even more the squeezing pressure rise up till they overcome the capillary pressure opposing to droplet pinch-off. The hypothesis is that the breakup process starts when these forces balance:

$$F_\sigma + F_\tau + F_p = 0 \qquad \Rightarrow \qquad (1 - \bar{b})^3 = \bar{b} \cdot \mathrm{Ca} \tag{3.9}$$

where $\bar{b} = b/w_c$. So b is the droplet length achieved by the droplet before the neck starts to shrink under the push of the continuous phase. The additional length gained by the droplet during the shrinking process can be readily obtained multiplying the droplet advancing speed $u_{growth} \approx Q_d/(bh)$ by the time needed to shrink the neck $t_{\text{squeeze}} \approx w_d/u_c \approx w_d w_c h/Q_c$ so that the final length rescaled on w_c results:

$$\bar{L} = \bar{b} + \frac{\Lambda}{\bar{b}} \phi \tag{3.10}$$

where $\Lambda = w_d/w_c$ and $\phi = Q_d/Q_c$. The approximate volume of the droplet should be:

$$\bar{V} = \frac{V}{w_c^2 h} = \bar{L}\bar{b} = \bar{b}^2 + \Lambda\phi \tag{3.11}$$

Although the model predicts a dependence of the volume of the droplets on Ca which is actually observed in the experiments and which is not underlined by the model of Garstecki *et al.*, the theoretical trend doesn't trace the experimental behavior as observed by the authors. In fact they defined a rescaled droplet production frequency as:

$$\bar{f} = \frac{\mu_c w_c}{\sigma} f \tag{3.12}$$

suggesting a power-law dependence of $\bar{f}$ on the capillary number at a fixed flow rate ratio ϕ in the range $10^{-3} < Ca < 5 \cdot 10^{-1}$:

$$\bar{f} \propto \mathrm{Ca}^{1-\delta} \ , \quad \text{for } \phi = \ \text{constant} \tag{3.13}$$

with $(1 - \delta)$ experimentally determined to be 1.31 ± 0.03 independent of the viscosity of the fluids and on the channel width ratio $\Lambda = w_d/w_c$. Since $\phi = Q_d/Q_c$ is choosen to be constant and $Q_d = fV$ where V is the volume of a single droplet, the rescaled droplet volume $\bar{V} = \frac{V}{hw_c^2}$ will be:

$$\bar{V} = \frac{\phi \mathrm{Ca}}{\bar{f}} \propto Ca^{\delta} \ , \quad \text{for } \phi = \text{constant} \tag{3.14}$$

with $\delta = -0.31 \pm 0.03$. This power law dependence disagrees either with the theoretical model presented by the same authors and with the theory of Garstecki *et al.* [100] and with that of Van Steijn *et al.* [2] which is going to be presented in the following.
Other theoretical scaling laws similar to those of Christopher and Grastecki were later proposed adjusting the parameters to the experimental evidences observed by each author, but in many cases the experimental data were reproduced only by adding free parameters thus betraying the quest for a simple law [108].

A significantly different approach based on purely geometric considerations was proposed by van Steijn *et al.* [2] to describe the generation of droplets in the squeezing regime at low capillary numbers (Ca < 0.01) and provided that channels width ratio is not extensively small ($w_d/w_c \geq 0.33$).
They reconstructed the three dimensional volume of the droplet by extrusion from its two dimensional projection on the T-junction middle plane. They approximated the upstream

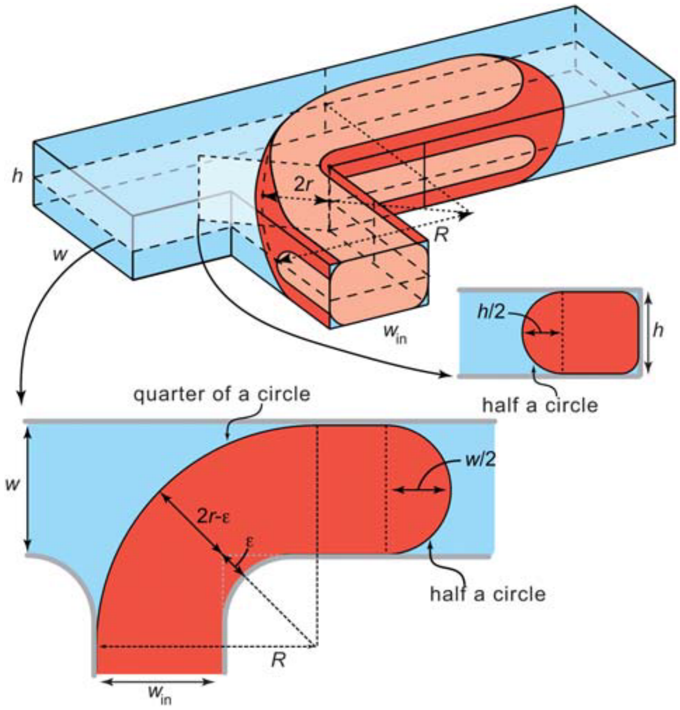

Figure 3.4: Geometrical reconstruction used by Van Steijn *et al.* [2] to calculate the size of the droplet using two-dimensional views. The top-view image shown on the bottom left shows that the receding interface takes the shape of a quarter of a circle with radius R, while the front of the droplet is described with half a circle with radius $w_c/2$. The curvature of the corners is taken into account by the distance ε. In the T-junction studied in this thesis ε can be neglected. The curvature in the plane perpendicular to the top-view image was supposed to be $h/2$.

border of the neck of the emerging dispersed phase as a quarter of a circle with a radius R and the advancing tip as half a circle with radius $w/2$ as in Fig.3.4.

The curvature of the lateral surface of the dispersed phase thread is supposed to be $h/2$ at the gutters. The extrusion volume obtained was described as a function of the surface A and the perimeter l of the projection on the T-junction plane:

$$V = h\mathcal{A} - 2\left(\frac{h}{2}\right)^2\left(1 - \frac{\pi}{4}\right) l \tag{3.15}$$

The width of the neck was indicated as $2r$. Similarly to Garstecki and Christopher they divided the growth process of the droplet before break-up into two steps: a first *filling* step during which the emerging droplet increases its volume till it occupies the whole width of the channel and a second *squeezing* step required for the shrinking of the neck before the ultimate pinch-off (Fig.3.2).

In the first step the droplet achieves a volume V_{fill} which was calculated simply by assuming that the droplet horizontal section could be represented by a quarter of circle of radius R near the neck and half a circle of radius $w_c/2$ at the tip, touching each other. In Fig.3.5 the two possible cases depending on the geometrical ratio w_d/w_c are sketched. By geometrical considerations R_{fill} and V_{fill} can be derived as follows:

$$R_{\text{fill}} = \max(w_d, w_c)$$

$$V_{\text{fill}} = \begin{cases} \frac{3\pi}{8} - \frac{\pi}{2}\left(1 - \frac{\pi}{4}\right)\frac{h}{w_c} & \text{for } w_d \leq w_c \\ \left[\frac{\pi}{4} - \frac{1}{2}\arcsin\left(1 - \frac{w_c}{w_d}\right)\right]\frac{w_d^2}{w_c^2} - \frac{1}{2}\left(\frac{w_d}{w_c} - 1\right)\sqrt{2\frac{w_d}{w_c} - 1} + \frac{\pi}{8} + & \\ -\frac{1}{2}\left(1 - \frac{\pi}{4}\right)\left[\left(\frac{\pi}{2} - \arcsin\left(1 - \frac{w_c}{w_d}\right)\right)\frac{w_d}{w_c} + \frac{\pi}{2}\right]\frac{h}{w_c} & \text{for } w_d > w_c \end{cases} \tag{3.16}$$

After the filling period the droplet starts to grow along the main channel with a rate fixed by the inlet flow Q_d. The time $\Delta t_{\text{squeeze}}$ left to this step is the time for the neck width $2r$ to shrink down to the minimum limit $2r_{\text{pinch}}$ at which breakup takes place.

In a previous paper [109] the same authors validated with the comparison to experimental data the idea that the breakup takes place when the Laplace pressure difference between the neck of the droplet and its tip becomes negative so that a reverse flow happens and, for a very short time during pinch-off, the continuous phase comes back through the gutters. According to this picture, imposing the capillary pressure to zero the pinch-off radius r_{pinch} can be determined. From:

$$\Delta p = \sigma\left[\frac{2}{h} + \frac{2}{w_c} - \frac{1}{R_{\text{pinch}}} - \frac{1}{r_{\text{pinch}}}\right] = 0 \tag{3.17}$$

it can be derived:

$$r_{\text{pinch}} = \frac{hw_c}{2\left(h + w_c - \frac{hw_c}{R_{\text{pinch}}}\right)} \tag{3.18}$$

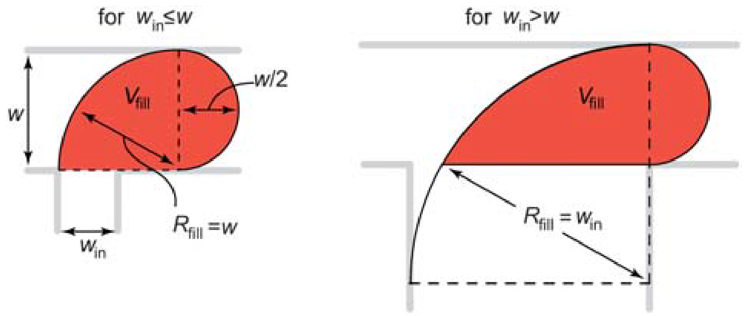

Figure 3.5: Shape of the droplets at the end of the filling period in case $w_d \leq w_c$ (left) or $w_d > w_c$ (right).

which is independent of σ. The pinch off radius R_{pinch} can be obtained upon geometry considerations (see Fig.3.4):

$$R_{\text{pinch}} = w_c + w_d - \left(\frac{hw_c}{h+w_c} - \varepsilon\right) + \left[2\left(w_d - \left(\frac{hw_c}{h+w_c} - \varepsilon\right)\right)\left(w_c - \left(\frac{hw_c}{h+w_c} - \varepsilon\right)\right)\right]^{1/2} \tag{3.19}$$

where ε represents the curvature radius of the channel corners provided that they are not sharp.

Therefore the time interval $\Delta t_{\text{squeeze}}$ corresponds to the time needed to the continuous phase to push the dispersed phase till the radius of curvature of the neck reaches the value R_{pinch}.

During the squeezing step, the increase in the volume occupied by the continuous phase upstream of the droplet will be:

$$\frac{\mathrm{d}V_c}{\mathrm{d}t} = Q_c\left(1 - \frac{Q_{gutter}}{Q_c}\right) \tag{3.20}$$

where Q_{gutter} is the flow rate of the continuous phase going beyond the droplet through the gutters. At the same time the increase in the area occupied by the continuous phase projection in the in-plane section is $\mathrm{d}A = 2\left(1 - \frac{\pi}{4}\right)R\mathrm{d}R$ while its perimeter changes by $\mathrm{d}l = \frac{\pi}{2}\mathrm{d}R$, so that using equation (3.15):

$$\frac{\mathrm{d}V_c}{\mathrm{d}t} = 2h\left(1 - \frac{\pi}{4}\right)\left(R + \frac{\pi h}{8}\right)\frac{\mathrm{d}R}{\mathrm{d}t}\ . \tag{3.21}$$

Equating equation (3.20) and (3.21) and integrating from t_{fill} to t_{pinch}:

$$\Delta t_{\text{squeeze}} = \left(1 - \frac{\pi}{4}\right)\left(1 - \frac{Q_{gutter}}{Q_c}\right)^{-1}\left[\left(\frac{R_{\text{pinch}}}{w_c}\right)^2 - \left(\frac{R_{\text{fill}}}{w_c}\right)^2 + \frac{\pi}{4}\frac{h}{w_c}\left(\frac{R_{\text{pinch}}}{w_c} - \frac{R_{\text{fill}}}{w_c}\right)\right]\frac{hw_c^2}{Q_c} \tag{3.22}$$

The volume gainned by the droplets during the squeezing step will be:

$$V_{\text{squeeze}} = \Delta t_{\text{squeeze}} Q_d \tag{3.23}$$

and the final rescaled volume of the droplet is:

$$\frac{V}{hw_c^2} = \frac{V_{\text{fill}}}{hw_c^2} + \frac{V_{\text{squeeze}}}{hw_c^2} = \frac{V_{\text{fill}}}{hw_c^2} + \alpha_V \frac{Q_d}{Q_c} \tag{3.24}$$

where:

$$\alpha_V = \left(1 - \frac{\pi}{4}\right)\left(1 - \frac{Q_{gutter}}{Q_c}\right)^{-1}\left[\left(\frac{R_{\text{pinch}}}{w_c}\right)^2 - \left(\frac{R_{\text{fill}}}{w_c}\right)^2 + \frac{\pi}{4}\frac{h}{w_c}\left(\frac{R_{\text{pinch}}}{w_c} - \frac{R_{\text{fill}}}{w_c}\right)\right] \tag{3.25}$$

Authors showed that this model predicts the linear dependence of the droplet volume on the flow rate ratio for different T-junction aspect ratios ($w_d/w_c = 0.33, 0.67, 1, 1.33, 3$) but, as can be noted, it doesn't account for the dependence of the droplets volume on Ca, instead verified by Christopher's experiments.

An exhaustive theory able to provide a scaling law for the droplet volume over the entire range covered by the capillary number in the suqeezing regime and describing the dependence on the geometry seems to lack still now. Therefore the realization and the study of the behavior of microfluidic T-junctions produced by new techniques and with new materials could provide further information useful to gain new insight towards the complete theoretical understading of the involved physical rules.

4 T-junction Realization

4.1 Techniques for Microfluidic Channels Fabrication

Although microfluidics was born in silicon transferring micro-fabrication techniques from electronics, nowadays the most employed materials for the realization of the channels are polymers. Thermal reticulating polymers like PDMS and PMMA, or light curing polymers like SU8, are widely used since standard moulding and photolitographic techniques respectively allow to obtain any two dimensional pattern needed for microfluidics applications. The degradable nature of polymers didn't slow down the wide spread of these techniques since polymeric devices are very cheap and fabrication processes have a good reproducibility so that for example a single silicon mould can be employed for the realization of tens of identical PDMS devices.

These characteristics made polymer based microfluidics very promising for the realization of cheap throwaway devices for medical or biological applications [110–112].

On the other hand a fresh research field is growing in side of disposable microfluidics which has the aim to conceive durable multitasking integrated chips able to provide more sophisticated analyses and samples manipulation, requiring optical and electronic stages which cannot be realized on polymers and which are too expensive to rely on their poor durability.

Many efforts have been spent to integrate polymeric microfluidic channels with silicon based electronics [113] or glass based optics [114] but clearly these solutions add fabrication difficulties, have lower reproducibility and do not get rid of all polymers disadvantages. The need for more durable, chemical resistant and biological compatible materials is due also to the not always stressed drawbacks of polymer-based microfluidics. PDMS for example is demonstrated to give issues in cell cultures: it absorbs hydrophobic molecules leading to a change in the concentration of biological samples flowing inside the channels and even leaching of uncured oligomers from the polymer network has been proved [115].

Depending on the specific application, issues with polymeric materials can be also encountered due to polymers porosity as explained by Zheng *et al.* [116].
These are the reasons for the renewed interest on the technological transfer from other research fields on solid materials to the fabrication of microfluidic structures. Among the most lucky examples are the chemical etching and mechanical micromachining of silicon inherited from microelectronics [117, 118] exploited also for realizing waveguides and ring-resonators for sensing optical stages, and the employment of femtosecond laser damaging inherited from optics able to join waveguides and microchannels in the same glass substrate [119].

The same technological process has not started yet for lithium niobate. As already stressed lithium niobate could be a valid alternative to glass and silicon for the integration of multiple stages able to produce, manipulate, sort droplets and analyze their contents; however in literature the only attempts to engrave microfluidics channels directly on lithium niobate were presented in the last four years by our colleagues at the University of France-Comté, Besançon (France) [120, 121] and by our group [122]. Therefore the research project described in this thesis presents one of the very first try to embed microfluidics in lithium niobate, a challenging task which required more than few efforts spent.
Many techniques have been employed for micro-fabrication on lithium niobate in the past, specially on the field of optics for ridge waveguides realization [43, 44] or surface patterning for photonic crystals, wavelength conversion, Bragg reflectance or diffraction [123], but there exist very few studies reporting the realization of structures of hundreds of micrometers in such a material [120, 121]. Therefore the starting point is considering all the different techniques used for micro-fabrication in lithium niobate and evaluating if they match the requirements for the realization of microfluidic channels. During this work many techniques have been taken into account considering advantages and drawbacks which are outlined in what follows.

Chemical Etching. Chemical etching is one of the most used technique for $LiNbO_3$ microstructuring, specially for the realization of ridge waveguides [44]. Lithium niobate has an extremely high chemical stability, thus a solution of hydrofluoric acid (HF) is needed to etch its surface. Although this technique allows to obtain surfaces with optical quality the etching rate of the process is very low, of the order of 1μm/h at room temperature along the face perpendicular to the -z crystallographic direction and down to few nm/min for the other surfaces, so that several tens of hours are needed for the realization of microfluidic channels in the best conditions. Moreover the dependence of the etching rate on the surface crystallographic direction makes difficult the realization of steep U-shaped channels on those surfaces where the etching rate is lower.

Different techniques have been studied to make faster the process but none is able to reach depth of more than few microns: proton exchange (PE) allows to increase the etching rate of one thousand times but the proton diffusion reaches a maximum depth of 3μm [124]; ion beam damage has also been proposed to enhance the effect of hydrofluoric acid up to an etching rate of 100nm/s but again the damage due to Ti ions implantation can reach only a depth of 2μm [125].

Reactive Ion Etching. RIE has been effectively used to etch $LiNbO_3$ using SF_6, CF_4 and CHF_3 plasmas at rates up to 50nm/min and a $LiNbO_3$ selectivity of 0.25 [126]. Even better results were obtained by Inductive Coupled Plasma (ICP) with an etching rate of 190nm/min [127]. Several hours would be needed for engraving a 100μm deep microfluidic channels but the quality of the surfaces makes this technique suitable to embed microfluidics in lithium niobate. However no attempts to engrave structures as deep as tens of μm have been reported yet to the best of the author's knowledge, thus an experimental investigation is needed to make real this opportunity. Due to the unavailability of the instrumentation this technique was not studied inside the framework of this thesis.

Focused Ion Beam Litography. FIB technique allows to obtain an optimal roughness of the channel walls (down to few nanometers as recently reported by Sridhar *et al.* [128]). Nevertheless the etching rate seems to be more suitable for nanofluidics rather than microfluidics since 30s are needed to engrave a nanochannel with dimensions $100\mu\text{m}\times0.1\mu\text{m}\times0.1\mu\text{m}$.

Mechanical Micromachining. Mechanical dicing and milling are among the most used technique to engrave micro-structures in silicon for opto-electronics due to their fast and easy operation. The employment of these techniques on lithium niobate was not investigated in the past and only since the last few years references can be found in literature. This is probably due also to the fact that lithium niobate is a very hard but brittle material and a very accurate study of process parameters has to be performed in order to engrave the material without scratches and cracks. Moreover its pyroelectricity and its piezoelectricity can contribute to material stresses during the material micromachining process. The only examples reported in literature are the employment of dicing saws as those described in detail in section 4.2 and a very recent study on lithium niobate micromilling where a CNC milling machine is used to engrave cilindrical holes with a diameter of 500μm and a depth of 450μm with an average roughness of 500nm [129].

Laser Ablation. Laser ablation is nowadays a widespread technique for the realization of optical waveguides and optical circuits [130–132] but it is being exploited also as a good alternative to etching and mechanical micromachining for the realization of microfluidic channels since it allows to design almost any two-dimensional pattern on the surface of the sample and to finely control the depth of the engraved structures. Moreover laser irradiation has been effectively employed to carry out also embedded channels in silica by chemical etching the substrate after the material to be removed was damaged by laser irradiation [133].
The employment of this technique to engrave microstructures has been mainly devoted to silicon or fused silica glass, while focused laser techniques are used on lithium niobate mainly for amorphisation or refractive index change to design waveguides and optical circuits [134] rather than for the ablation of the material. Nevertheless results similar to those needed for microfluidics are reported to realize U-shaped and V-shaped hollows for the placing and the passive coupling of fibers [135].
Employed laser sources are Ar-ion lasers [136], excimer UV-light lasers [137] or Ti:Sapphire femtosecond lasers [138, 139].
In fact laser ablation on lithium niobate is a good candidate for the realization of microfluidic channels since provides a fast removal of the material and ensures a quite low roughness of the walls and flexibility in the circuit design.
A deeper experimental investigation of this technique for the realization of extended microfludics channel is given in section 4.3.

4.2 Mechanical Micromachining

Mechanical micromachining is one of the most employed techniques in optical devices technology when optical grade smooth surfaces are needed since it generally provides good quality surfaces in the shortest fabrication time. Although this technique is poorly used to engrave lithium niobate, its easiness and reproducibility of operation make it attractive when deep microfluidic channels have to be engraved.

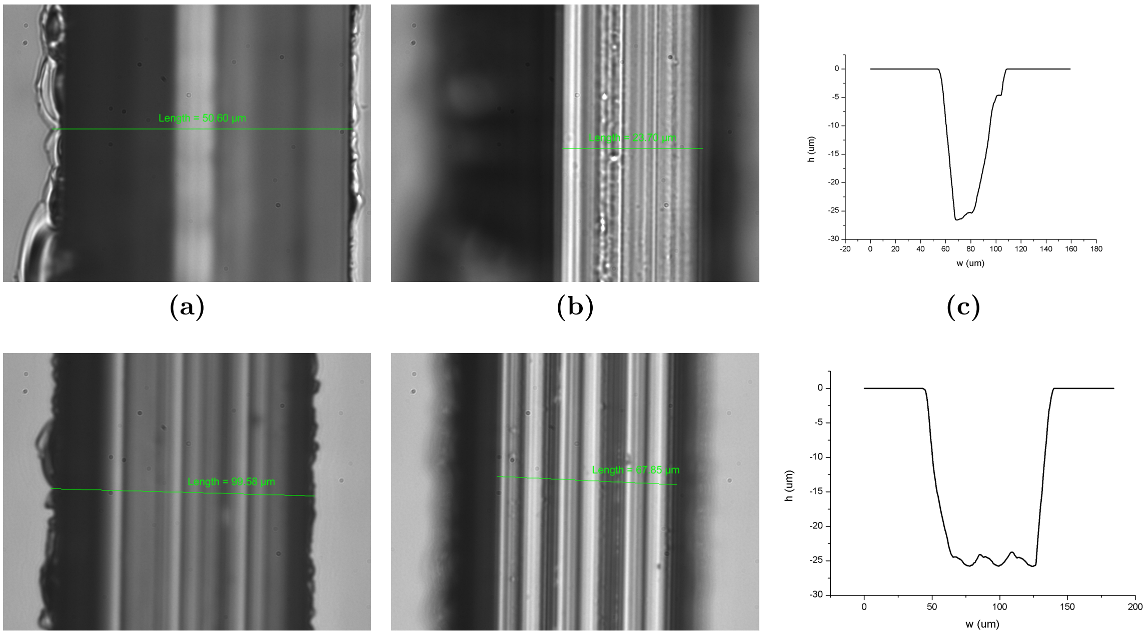

(a) **(b)** **(c)**

(d) **(e)** **(f)**

Figure 4.1: Microscope images and profilometer measurements of channels engraved with the ADT 7100 Series - 2" VECTUS dicing saw. The first horizontal set of images refers to a single saw scan, while the second one shows a channel obtained by three subsequent scans as can be easily understood by the profile of the channel bottom.

This is why the first technique tested during this research was an optical grade dicing with a Dicing Saw ADT 7100 Series – 2” VECTUS in collaboration with the MISTER lab of the IMM CNR in Bologna. The saw has a nominal width of 60μm so that to obtain 100μm or 200μm wide channels more scans are needed.

Microscope images and profilometer scans are shown in fig.4.1 while in fig.4.2 SEM images are reported. Although the side walls are very smooth they don’t reach an optical quality; in addition the lower average roughness of the bottom of the channels obtained in the performed test to obtain a channel with a width of 100μm was $R_a = (530 \pm 10)$nm which is not the best achievable result as will be shown in what follows. Another important defect produced by this type of saw is the poor quality of the edges on the upper part of the channel which presents scratches and cracks. Avoiding these defects is a very important feature to be reached for the realization of the device described in this wok since the aim is to realize waveguides by diffusion of titanium from the surface of the crystal, thus the waveguides will be placed in the very first microns below the surface.

Another type of blade DISCO DAD 321 precision saw was tested later for microma-

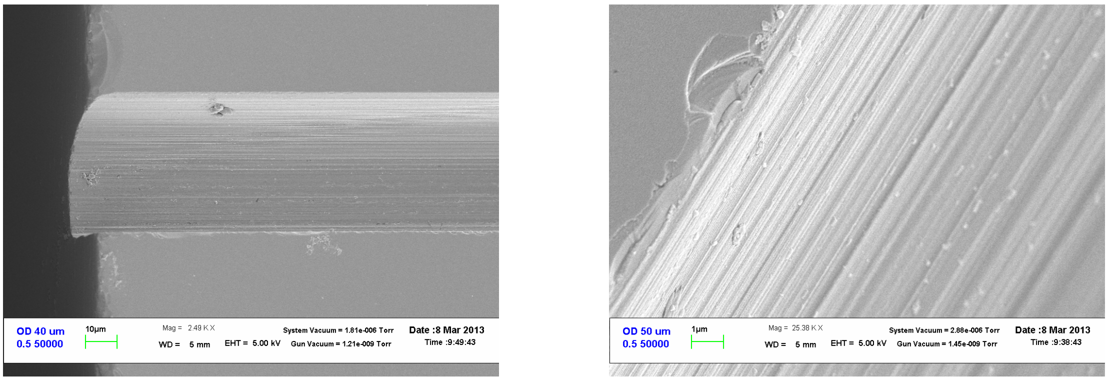

Figure 4.2: Examples of SEM images of the microfluidic channels engraved with the ADT 7100 Series - 2" VECTUS dicing saw.

chining of lithium niobate in collaboration with the University of France-Comté, Besançon (France). This polymeric blade with diamond particles has a diameter of 56mm and a thickness of 200μm. The parameters for providing the best surface quality were a rotating speed of 10000rpm and a cutting speed of 0.2mm/s. A constant and high flow of water was employed to keep the sample and the blade at a low temperature during the process and get rid of crystal residuals.

The obtained microchannels were characterized by optical microscopy and profilometry (fig.4.3). As can be seen from microscope images the quality of the edges at the top of the channel is higher than that obtained with the blade described previously.

Test samples were then eroded from one side until one of the side walls of the channel was erased in order to make both bottom and lateral surface reachable by the tip of an atomic force microscope (AFM). The morphology was studied by topology measurements performed in contact mode with a Veeco CP-II AFM which showed an average roughness of (19 ± 6)nm and (6.8 ± 0.5)nm for the bottom and lateral surfaces respectively.

This is the lower roughness obtained in this work for the side walls of the microfluidic channels, nevertheless the polymeric blade gives no chance to obtain a T-junction since the curvature of the blade makes the last part of the channel ($\sim$ 2.4mm for a channel 100μm deep) having a decreasing depth. This technique was thus employed to realize cross-junctions with four branches.

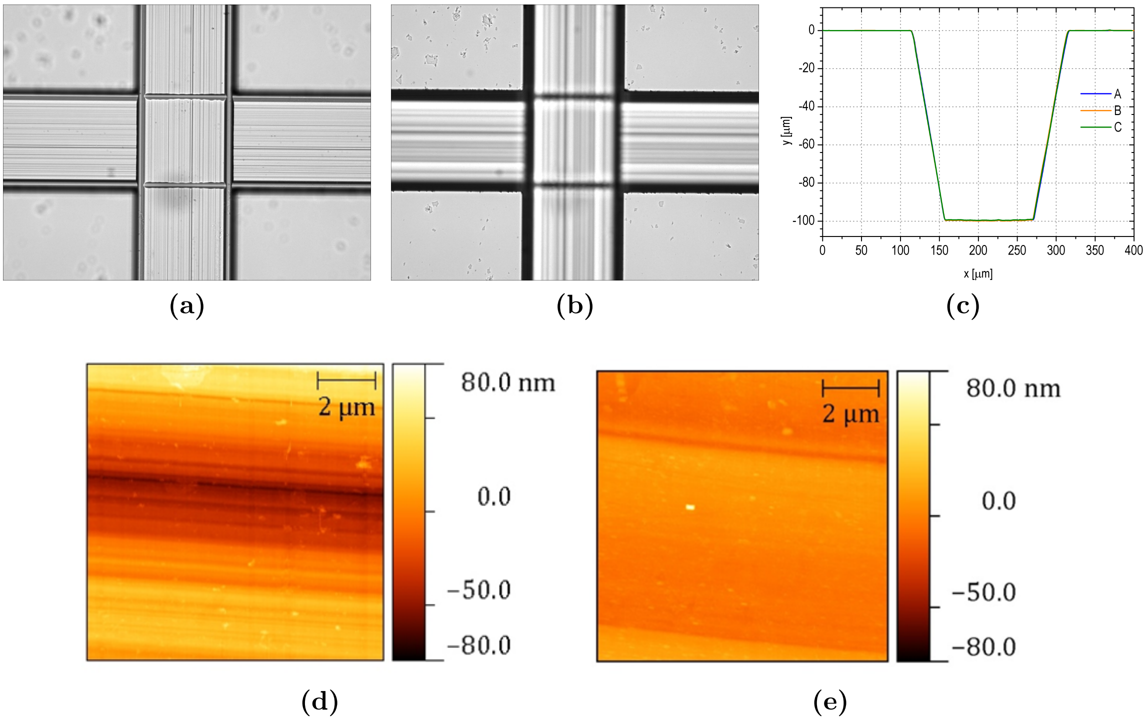

(a) (b) (c)

(d) (e)

Figure 4.3: Characterization of the microfluidic channels engraved on $LiNbO_3$ with a dicing saw DISCO DAD 321. (a),(b) Micrographs of the bottom and the top edges respectively of two crossing microfluidic channels; (c) superposition of profiles collected from three different positions along the two microfluidic channel showing the high reproducibility of the channel geometry; (d),(e) $10\times10\mu m^2$ AFM images of the bottom and the side of the channel respectively: the average roughness are 19 ± 6nm and 6.8 ± 0.5nm.

4.3 Laser Ablation

In this section the results from laser ablation tests performed on lithium niobate samples and the optimization of the process parameters are described.

The realization of the channels was perfomed by our collaborators of the *"Nonlinear Photonics Group"* of prof. Cornelia Denz at the Institute of Applied Physics of the Univeristy of Munster (Germany) while the characterization of the samples was made at the Physics and Astronomy Department in Padova.

A Ti:Sapphire femtosecond laser with an operating wavelength of 800nm, a pulse repetition rate of 1kHz and a pulse duration of 120fs was focused on the surface of the samples by a 50× ultralong working distance microscope objective (NA=0.55). The crystal was placed on a three dimensional translational stage controlled by computer driven step motors able to move the sample in all directions with a resolution of few tens of nanometers.

Samples from lithium niobate polished Y-cut commercial wafers by Crystal Technology were employed to perform the ablation tests. The crystal was moved through horizontal and vertical steps of 10μm and 15μm respectively in order to scan with the focused laser beam the volume to be engraved.

Several systematic tests were performed varying the scanning speed of the laser beam between 50μm/s and 1000μm/s and its pulse energy in the range $1 \div 20\mu$J. The engraved channels were U-shaped grooves along the lateral edge of the sample in order to make possible to observe both their bottom and their side walls with a microscope. Microscope images taken with a Nikon Plan 10x/0.25 objective are listed in figg.4.4, 4.5, 4.6, 4.7.

The grooves have an horizontal section of $(200 \times 250)\mu\text{m}^2$ and the scanning depth was set to 100μm. Irrespective of that different depths have been obtained depending on the employed pulse energy. For example looking at the channels engraved at a speed of 50μm/s, the channel engraved at a pulse energy of 2μJ has a heigth of 80μm while that engraved with a laser pulse of 10μJ reaches a depth of 129μm. The sublimation of the material from the surface of the sample requires an energy greater than a certain threshold. Since the horizontal and the vertical step of the translational stages are fixed, if the threshold energy is not reached in a sufficiently large area of the focused Gaussian beam, part of the material covered by a single scan line is not removed and it prevents the ablation of further layers by absorbing light at the following scan steps. A way to overcome this problem could be decreasing the horizontal and vertical steps between two adjacent scan lines but this makes increase quadratically the time needed for the realization of the channels.

Scanning speed also affects the ablation process: differences are not as remarkable as between different pulse energies but a more effective removal of the residuals can be noted in the grooves engraved with a lower scanning speed which have also steeper side walls specially at lower energies, while a faster scan avoids scratches on the edges at higher energies.

A defect which is evident in all the engraved structures is the presence of dark residuals deposited on the surfaces which affect the transparency of the crystal. Standard sonication lasting several hours in different solvents like ethanol, acetone, and acid and basic solutions ($HCl_{(aq)}$, $NaOH_{(aq)}$) were proved to be ineffective in removing this defects. This is probably due to the fact that those dark zones have a similar composition to the original crystal.

The only way to get rid of darker zones was a bath in a solution containing fluorhydric acid. In particular an EtOH:HNO3:HF 8:2:1 solution was used since it was demonstrated to give a better quality of the etched surface than a simple HF aqueous solution [44].

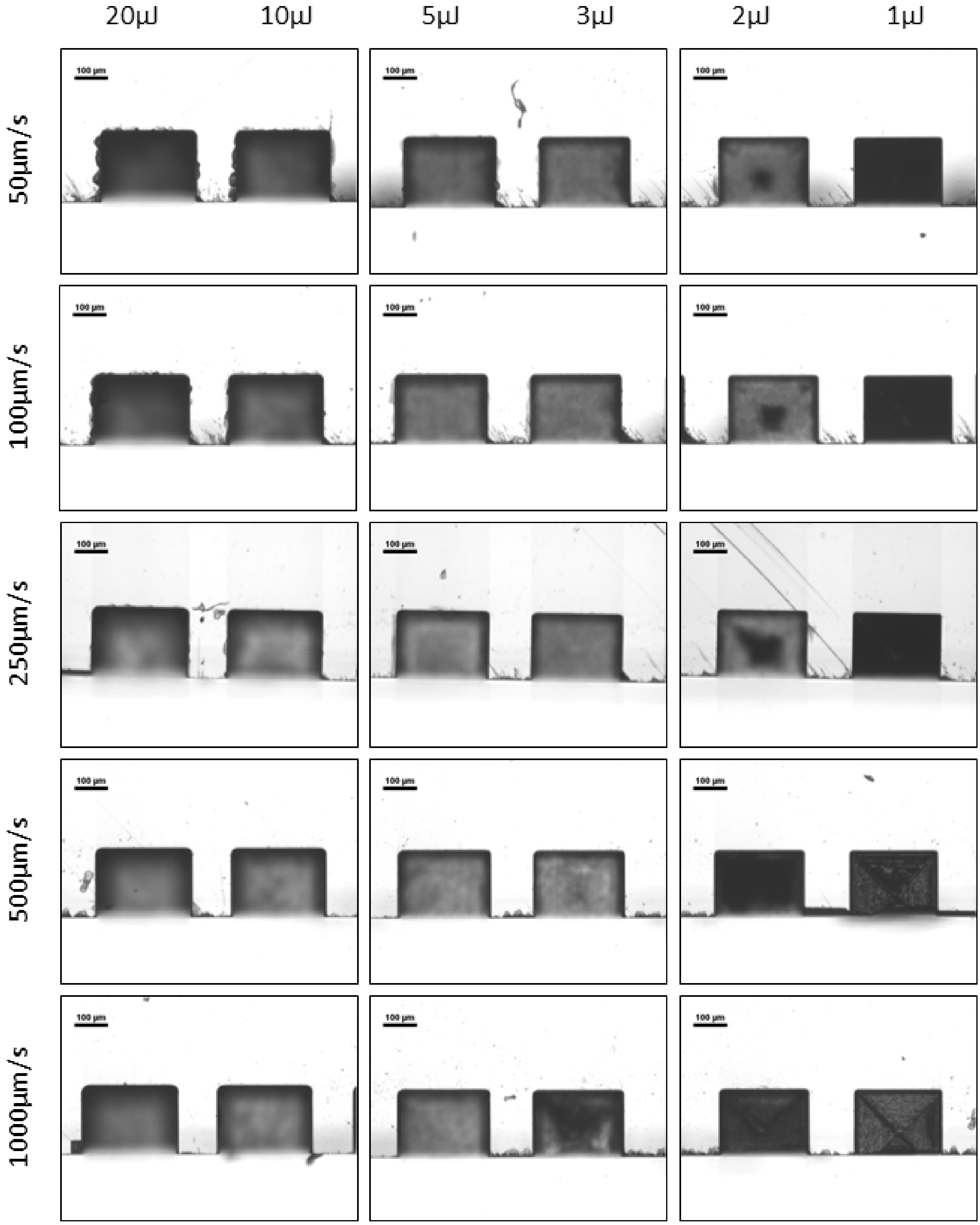

Figure 4.4: Microscope images of the top edge of U-shaped channels obtained by femtosecond laser ablation on a y-cut lithium niobate sample at different energies and scan speeds.

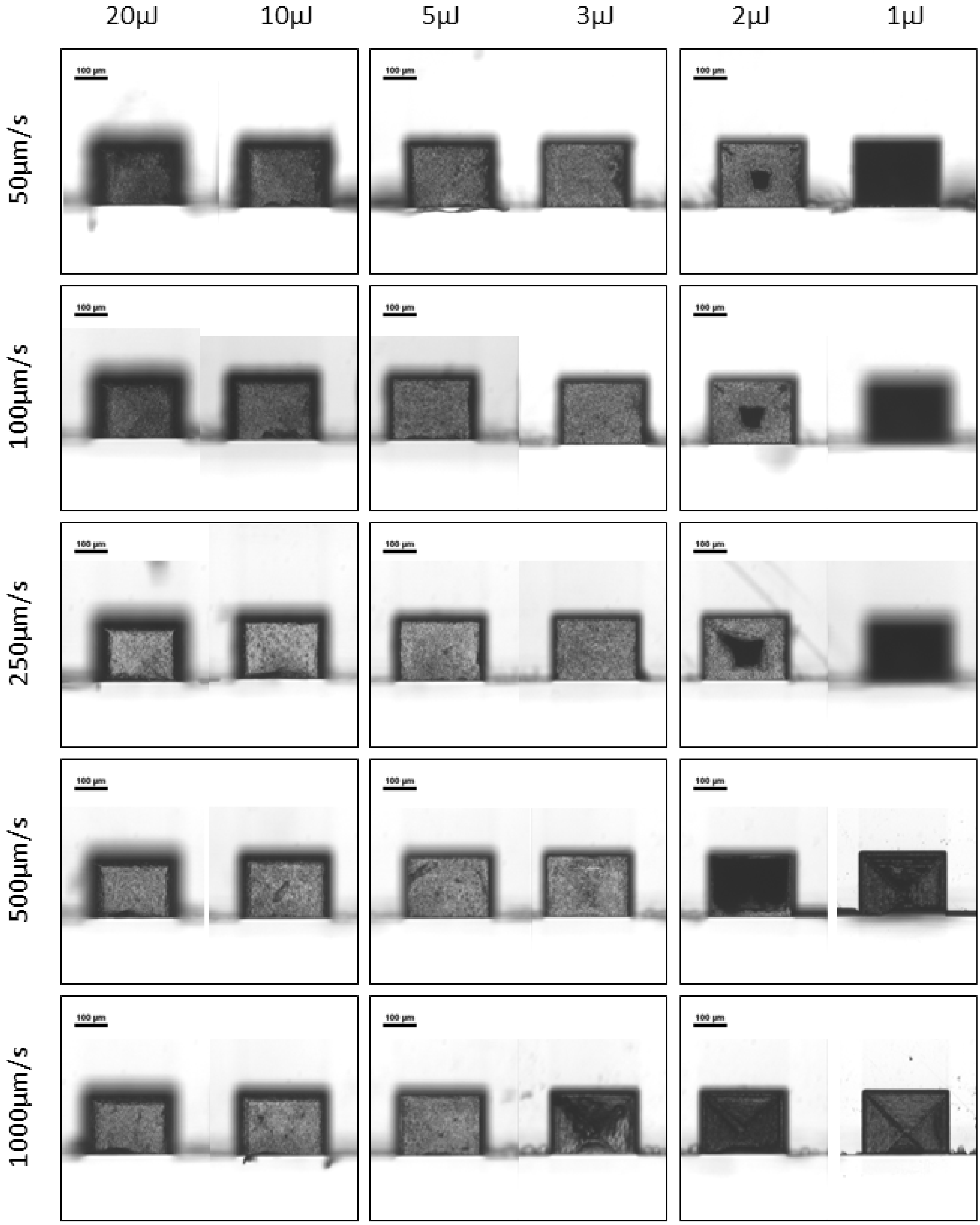

Figure 4.5: Microscope images of the bottom surface of U-shaped channels obtained by femtosecond laser ablation on a y-cut lithium niobate sample at different energies and scan speeds.

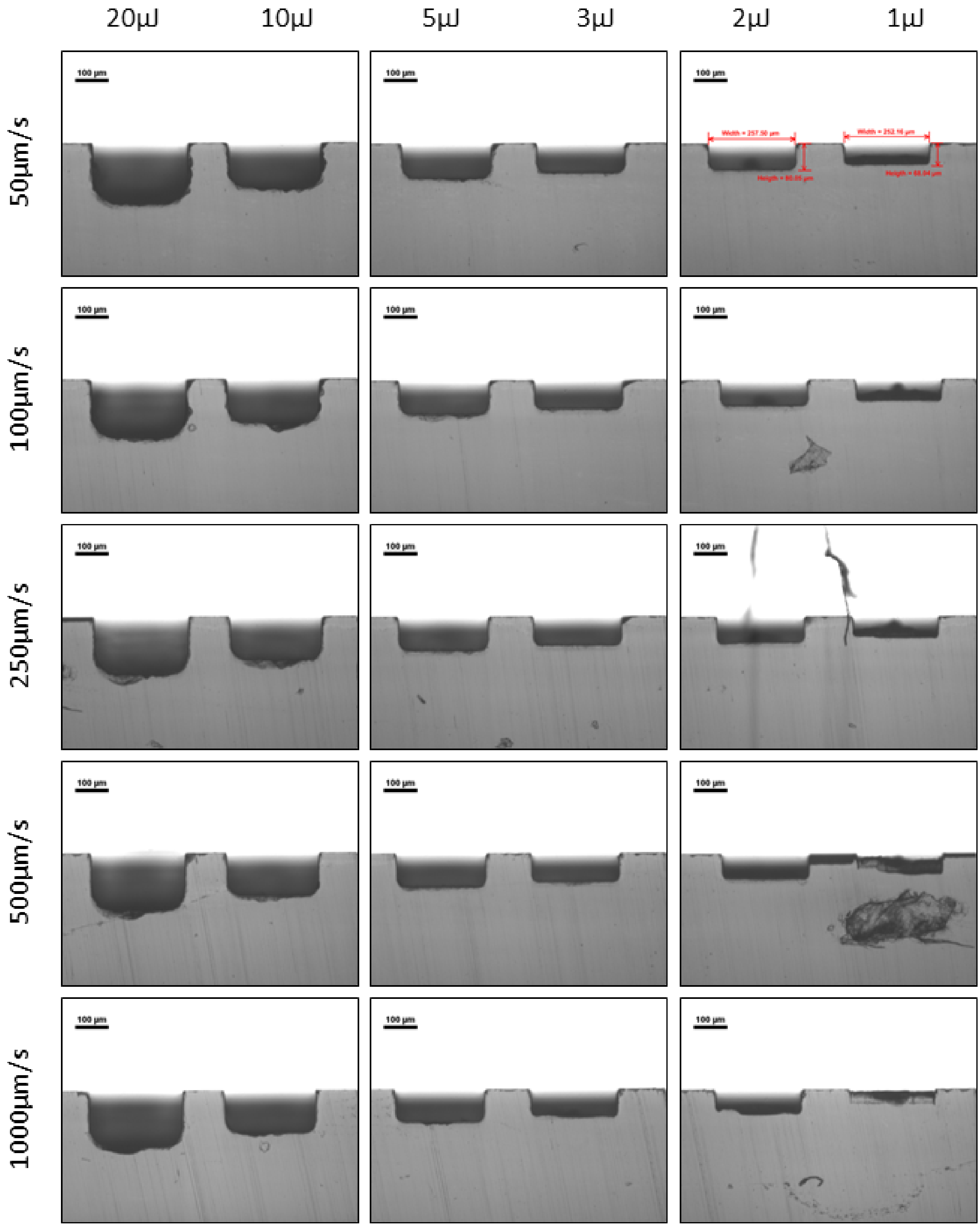

Figure 4.6: Microscope images of the lateral edge of U-shaped channels obtained by femtosecond laser ablation on a y-cut lithium niobate sample at different energies and scan speeds.

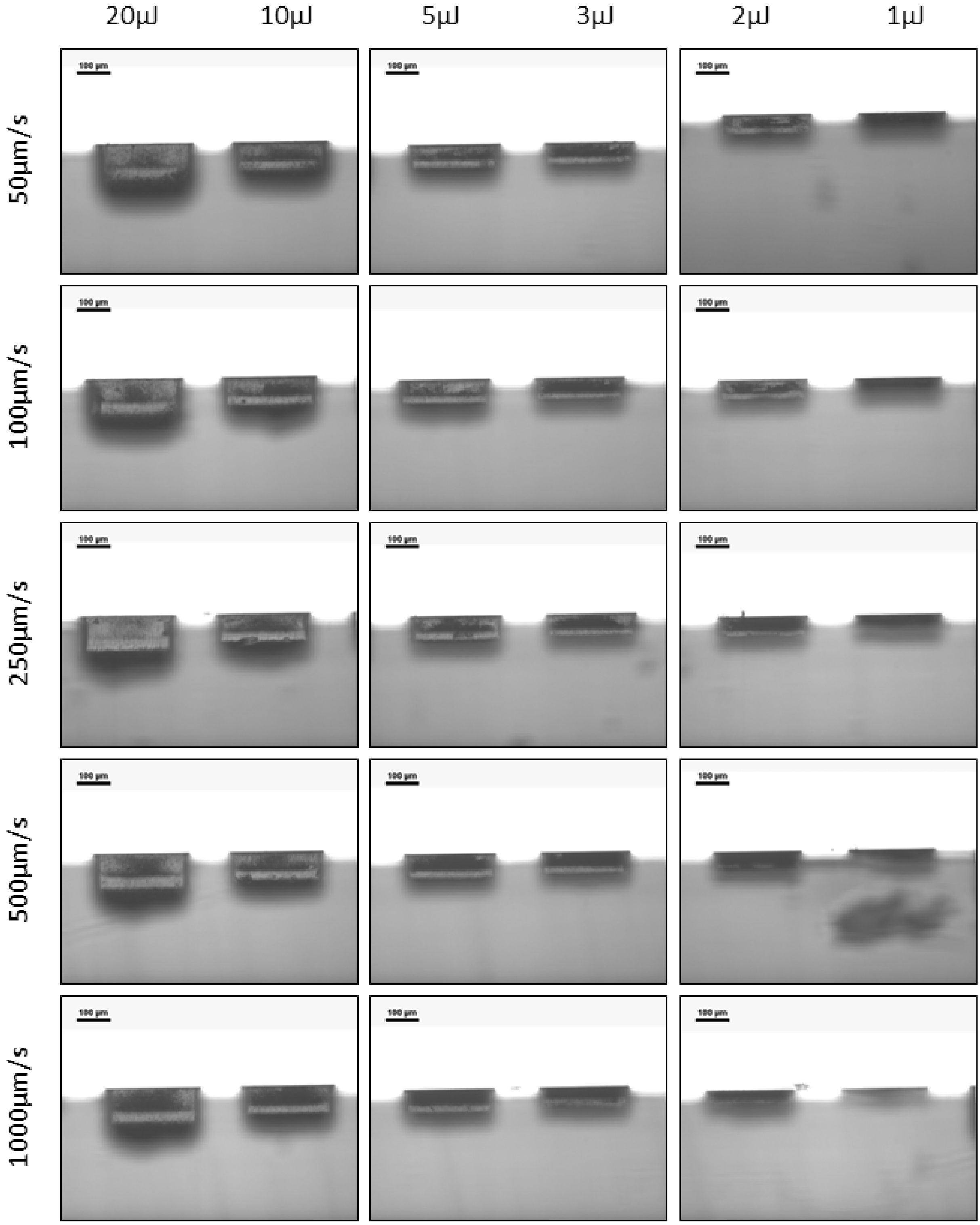

Figure 4.7: Microscope images of the side wall of U-shaped channels obtained by femtosecond laser ablation on a y-cut lithium niobate sample at different energies and scan speeds.

A study on the time needed to etch the dark zones without damaging the quality of the channel surfaces was performed observing the channels after different dipping times: 5, 10, 35, 95, 300 and 720 minutes. As can be seen from the example in fig.4.8, after a dipping time of 5min a large part of residuals are removed and between 10min and 35min of etching all samples recover their transparency; however a too much lasting etching results in a damage of the surface which starts before an hour and a half and ends in a complete opaque surface for etching times longer than few hours.

Optical microscopy was useful to exclude too much higher or too much lower pulse energies but cannot give sufficient information to choose the best parameters in order to have a surface as smooth as possible. A further test was thus performed engraving grooves with a different aspect ratio in order to be able to reach the surfaces with the tip of an atomic force microscope and investigate their roughness without masking the laser probe reflecting on the cantilever.

U-grooves 600μm wide along the edge of the samples, extending 150μm in the direction parallel to the surface and with a depth of 150μm were engraved on a new sample. A restricted set of energies and scanning velocities was selected choosing among the parameters which showed to give the best transparency of the side walls together with a higher energy of 50μJ: $E = 5, 20, 50\mu$J and $v = 100, 500, 1000\mu$m/s.

Since the aim of this work is the coupling of a waveguide perpendicular to the microfludic channel the roughness of the side walls of the engraved channel has to be as low as possible to avoid diffraction and signal loss, thus an accurate AFM analysis of the side walls surface was performed. Few images of a 10×10μm^2 area are reported in fig.4.9 while wider images with and area of 30×30μm^2 are listed in fig.4.10. Small bulges are present on the surface and looking at the 10×10μm^2 areas their dimension seems to increase with pulse energy. Vertical cracks aligned to the direction of the engraving laser beam appear at higher energies and lower speeds. They are much more evident in the image of the 30×30μm^2 areas. The average roughness of the side walls calculated from the mean value of a series of more than 5 sampled 10×10μm^2 areas are reported as a function of scanning speed and pulse energy in fig.4.11. The roughness increases with pulse energy and has a minimum at an intermediate scanning velocity.

The parameters $E = 5\mu$J and $v = 500\mu$m/s were chosen to engrave the T-junctions described in this work since they gave the lower value of roughness: $R_a = 170 \pm 11$nm at the bottom of the channel and $R_a = 50 \pm 3$nm at the side wall.

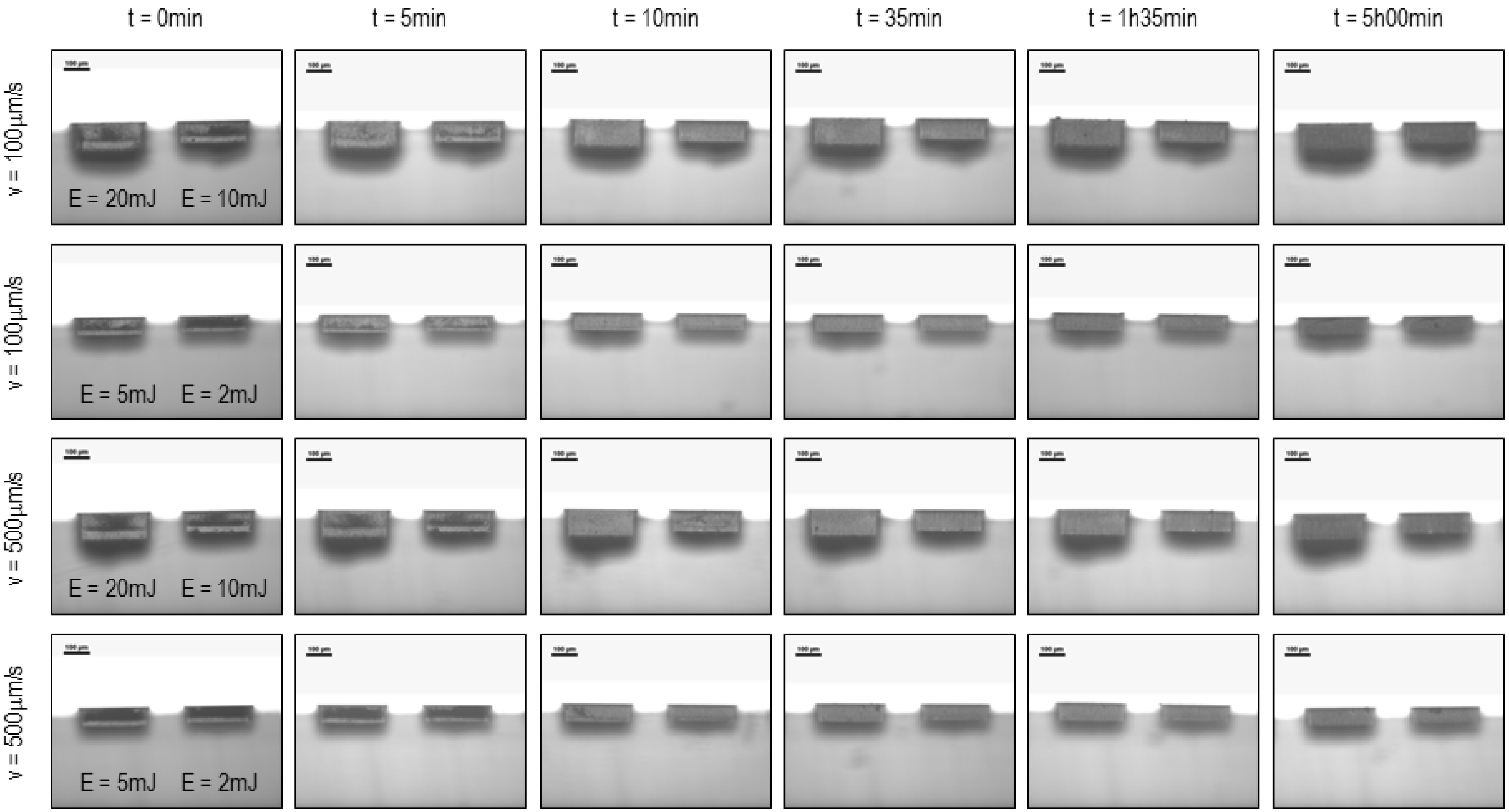

Figure 4.8: Images of side walls modification after different etching times: 5, 10, 35min, 1h35min, 5h. Examples for four pulse energy values (2, 5, 10, 20μJ) and two scan speed values (100, 500μm/s) are reported.

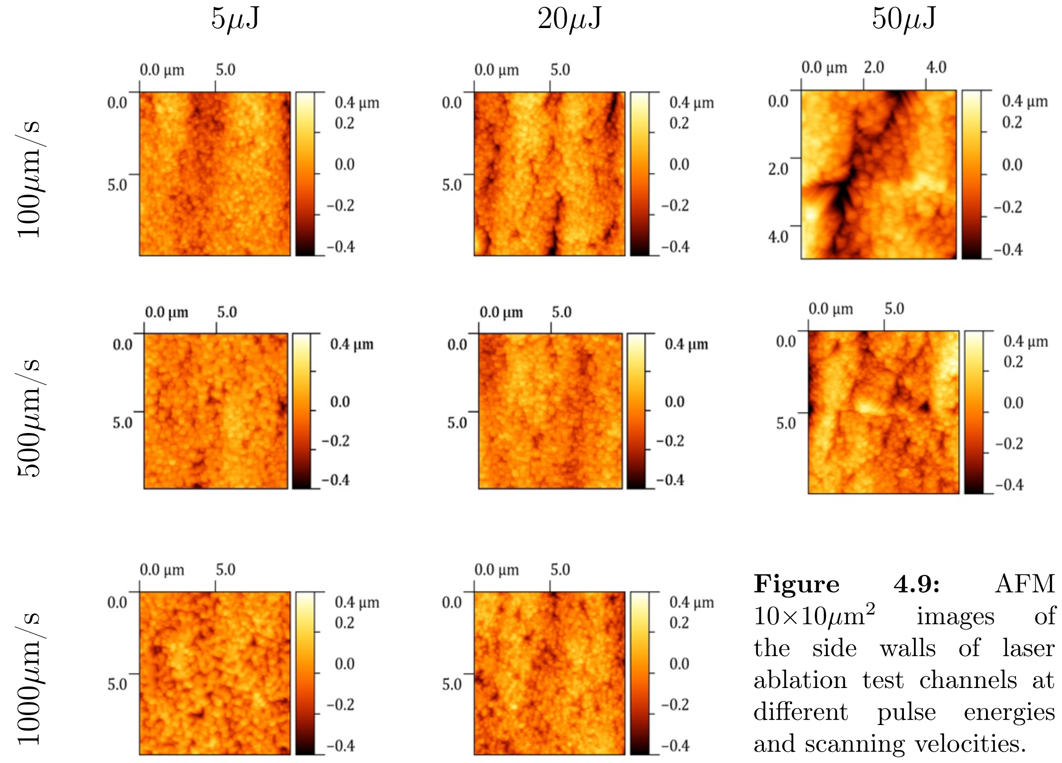

Figure 4.9: AFM $10\times10\mu m^2$ images of the side walls of laser ablation test channels at different pulse energies and scanning velocities.

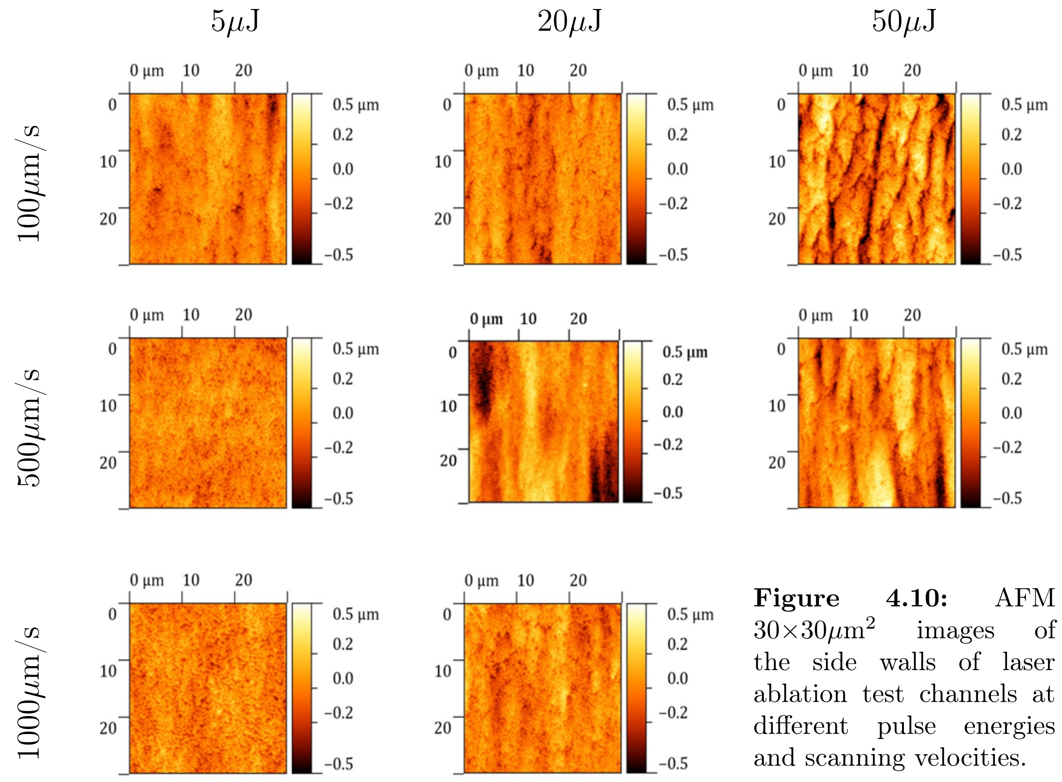

Figure 4.10: AFM $30\times30\mu m^2$ images of the side walls of laser ablation test channels at different pulse energies and scanning velocities.

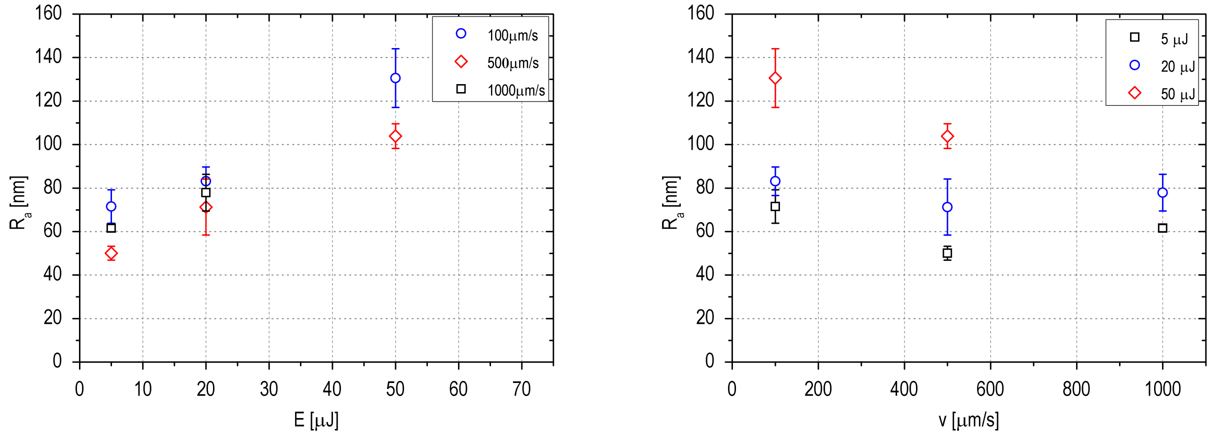

(a) **(b)**

Figure 4.11: Trend of the average roughness with (a) the pulse energy and (b) the scan velocity during the ablation process.

4.4 Microfluidic Chip Sealing

All the techniques described in the previous sections allow to engrave microfluidic channels on the surface of the crystal. In order to complete the microfluidic device they have to be closed and inlets and outlets for the fluids need to be integrated.

Different solutions have been tested during the work for this thesis little by little improving the resistance to the pressure for a higher droplet production frequency and the chemical resistance to solvents needed to ensure an all-purpose device. In the following some of these techniques are briefly described.

4.4.1 PDMS Layer Sealing

The first technique employed to seal the microfluidic channels was replied from the most used technique in literature i.e. the bonding of a polydimethylsiloxane (PDMS) layer to the lithium niobate crystal [140].

A specific curing agent was diluted at a concentration of 0.1(w/w) in few grams of Sylgrad$^{\circledR}$184 prepolymer by Dow Corning. A silicon wafer was made highly hydriphobic after functionalization in a vaccum chamber at room temperature with gaseous trichloro-perfluorooctyl-silane[1] and used as the basis of a mold where MASTERFLEX$^{\circledR}$ silicone tubing by Cole-

---

[1] trichloro-perfluorooctyl-silane: $CF_3(CF_2)_5CH_2CH_2SiCl_3$, CAS Number 78560-45-9; Mm = 481.54g/mol; density 1.3g/ml.

Parmer (OD = 4mm; ID = 0.8mm) were displaced at the right distances on the silicon basis for the inlets and the outlet. A ~5mm thick layer of the prepolymer solution was poured in the mould and after 2h curing in an oven at 70°C the reticulated PDMS covering was done. The removal of the solidified PDMS layer from the substrate was easy thanks to the hydrophobic functionalization of the silicon basis.

The engraved lithium niobate sample was cleaned in a sonicating acetone bath and in an UVO-cleaner for 15min. It underwent, together with the PDMS covering, an O_2-plasma treatment inside a FEMTO plasma system chamber at an RF power of 200W for 60s, with an oxygen flow rate of 10sccm at a pressure of $3 \cdot 10^{-3}$mbar. Immediately the crystal and the sealing were kept attached matching the inlet and outlet tubing with the microfluidic channels endings. As in the case of other oxides (silica, quartz) a condensation reaction takes place between the outer hydroxyl groups present at the surface of both materials resulting in a tight O-Si-O covalent bonding between the crystal surface oxygen atoms and the silicon atmos of the polymeric chains. This reaction is favoured after the plasma treatment because PDMS exposed to the oxygen plasma develops silanol groups (Si-OH) at the expense of methyl groups ($Si\text{-}CH_3$) [140].

This type of sealing showed to be resistant to fluid flow rates up to 400μl/min before starting to leak, that means a pressure of about 2.4atm in our T-junction device. Nevertheless it was perfect for the first tests on the microfluidic devices since it could be easily removed by pulling out the covering by hands little by little exploiting the elasticity of PDMS and possible residuals hardly bonded to the surface of the lithium niobate crystal could be removed in a basic bath of $NaOH_{(aq)}$ at a temperature of 70°C for few hours. The disadvantages of employing a PDMS layer as the cover of the microfluidic device are:

- the progressive degradation suffered by the polymer, which affects its transparency and its elasticity after few weeks at ambient conditions;

- its not negligible swelling when common solvents like ethanol, acetone, toluene but also many oils like hexadecane, decane and mineral oil are fluxed inside the channels;

- its poor resistance to chemical agents (PDMS starts dissolving in acetone, toluene or poorly acid and basic solutions);

- its poor stiffness which could affect the reproducibility of the produced droplets.

4.4.2 Glass Sealing Type 1

Another type was designed in order to avoid considerable swelling and poor stiffness of the PDMS layer.

A microscope silica slide was cut with the same geometry of the lithium niobate crystal and three holes were drilled with a drill diamond coated bit at the same positions where the channels ended. Then three pieces of MASTERFLEX® silicone tubing were placed on the holes and few drops of Sylgrad®184 prepolymer prepared as described in the previous section were let slip aside the tubings till they reach the glass slide. After 2h in an oven at 70°C the tubings were tightly bounded to the glass cover by the reticulated PDMS.

At this point a thin film of prepolymer $(4.7 \pm 0.1)\mu$m high was deposited by spinning at a speed of 6000rpm for 90s on a silicon wafer functionalized as those used for the PDMS layer sealing and put inside a vacuum chamber. A magnet was attached at the glass cover prepared earlier and it was put inside the same chamber making it hanging over the thin prepolymer layer from the top of the chamber thanks to another external magnet.

After a $8 \cdot 10^{-1}$mbar pressure was reached the external magnet was pulled away so that the glass cover felt down on the prepolymer layer. The vaccum was needed to avoid air microdroplets which aroused if the glass cover was placed on the prepolymer layer at ambient pressure and which would have made riddled the upper wall of the channels. After curing again in the oven the cover was removed from the silicon basis with the thin PDMS layer entirely covering its lower surface.

Finally this cover can be bonded to the lithium niobate crystal after O_2-plasma treatment as made for the previous PDMS layer covering. The advantages of this new technique are the highly improved stiffness due to the rigidity of the glass slide and a higher pressure resistance (tested flow rates up to ~2ml/min without leakage, may be the flow rate limit is even higher). The disadvantages are that the thin layer of PDMS is present also on the top wall of the microfluidic channels so that we observed it suffers degradation when solvents were flown but also it starts to flake off even after several hours of hexadecane flowing, probably after excessive swelling.

4.4.3 Glass Sealing Type 2

In order to get rid of the PDMS on the upper wall of the channel it was decided to use the polymer to glue only the borders of the microfluidic chip. A framework along the whole

border of the glass cover was then eroded with a sandblaster and after being cleaned it was placed in contact with the lithium niobate sample. Hexadecane was slowly fluxed along the tubings of the covering till it reached the lithium niobate substrate and it filled by capillarity the thin interlayer present between the crystal and the glass but not the thicker space in between the glass eroded area and the lithium niobate sample. At this point a small amount of PDMS was laid around the cover in order to fill the higher gap under the eroded area and then cured at at 70°C for 2h.
This sealing type had a high resistance to pressure and no polymers facing the microfluidic channel. Nevertheless it was observed that during the droplet generation, when flow rates higher than few tens of μl/min were reached, water starts to percolate through the thin gap between the cover and the crystal, filled earlier with hexadecane, and the stability of the droplet production was compromised.

4.4.4 Glass Sealing Type 3

Apart from PDMS which suffers swelling and degradation, other polymers can be used to glue together two oxides. An efficient adhesive polymer employed to bound glass or plastic surfaces is the Norland Optical Adhesive 68 (NOA68) by Norland Products Incorporation. It is a clear, colorless, liquid photopolymer which becomes 100% solid after curing under UV light at a $350 \div 380$nm wavelength. It is resistant to acid solutions (tested by manufacturer in 10% $H_2SO_{4(aq)}$, 5%$H_2PO_{4(aq)}$, 5% $CH_3COOH_{(aq)}$) and to many organic solvents (hexane, toluene, methanol, trichloroethylene). Since in its solid phase after curing it cannot be effectively bonded to the lithium niobate crystal with plasma treatment as the PDMS, another technique has been conceived. A glass cover endowed of inlet and outlet tubings realized from a microsope slide as explained in section 4.4.2 was cut sligthly narrower than the lithium niobate crystal. It was placed on the lithium niobate sample and kept deep in contact with it by a clump. On the exposed borders of the crystal surface a small amount of NOA was deposited all around the glass cover and during a time lasting about 24 hours the polymeric adhesive filled the thin space between the sample and the cover by capillarity reaching the microfluidic channels edges. Surface tension avoids NOA to flow inside the channels since they are much larger than the thin layer between the surfaces where NOA stays confined (100μm of the channel height compared with the few microns of the gap between the crystal and the glass).

Name	Type	Width (w)	Depth (h)
TJ1	T-junction	$(126 \pm 2)\mu$m	$(89 \pm 6)\mu$m
TJ2	T-junction	$(125 \pm 3)\mu$m	$(100 \pm 1)\mu$m
CJ1	Cross-junction	$(202 \pm 1)\mu$m	$(99.1 \pm 0.4)\mu$m
CJ2	Cross-junction	$(205 \pm 1)\mu$m	$(98 \pm 1)\mu$m

Table 4.1: List of droplet generators devices described in this thesis together with the channels width and depth.

After UV light exposure and oven baking as indicated by Norland Products Incorporation a sealed, completely solid chip is done.

This technique ensures a pressure resistance at least as high as the previous one with the further advantages that NOA is very stiff after curing and then no elastic deformations of the gluing layer are possible opposing to a PDMS layer. Moreover the chemical resistance is considerably improved and there is no polymeric layer at all on the top wall of the channel.

4.5 Realized T-junctions and Cross-junctions

The microfluidic droplet generators, which are described in this work, were realized both by laser ablation and by optical dicing with the DISCO DAD 321 dicing saw.

A T-junction geometry was performed by laser ablation, with a main channel 18mm long and a perpendicular channel injecting the dispersed phase 6mm long. The versatility of the technique allowed to engrave also three reservoirs of rectangular shape at the beginning and the end of the channel with a side of length 1mm (see fig4.12).

The width and the heigth of the T-junction were measured with a profilometer KLA Tencor P-10 and the corresponding values are reported in table 4.1.

Both the T-junctions were sealed with a PDMS layer with integrated tubings (see section 4.4.1).

A cross-junction geometry was instead performed by the dicing saw since the saw could not engrave a channel with a constant depth which interrupts abruptly. An example of such a geometry is reported in fig.4.12. The width of the channels was set to 200μm due to the saw thickness and the nominal depth was 100μm. The measured values of their effective channels width and height are reported in table 4.1.

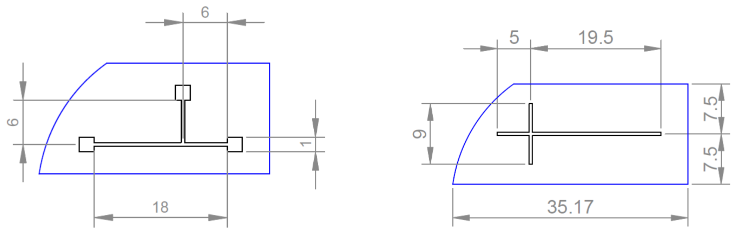

Figure 4.12: Schemes of samples engraved with the laser ablation technique (on the left) and the dicing saw (on the right). Quotes are expressed in millimetres. Curved edges are due to the shape of the commercial wafer grown by Czochralski technique from which samples were cut.

Both these devices were sealed with a glass cover sealing type 3 (see section4.4.4).

4.6 Lithium Niobate Wettability Study

One of the most important characteristic of a material which has to be employed in microfluidics applications is the wettability, i.e. the interaction between the fluids and the surface of the material.

Wettability is the result of microscopic interactions between the surface and the molecules of the fluid and it usually depends on chemical composition and physical morphology of the surface, as well as on the chemical and physical properties of the fluid such as surface tension, molecules polarization and molecules polarizability.

The standard way to characterize wettability is the measurement of the static contact angle: a small droplet of the liquid is deposited on the surface and the angle θ between the solid surface and the liquid-air interface is measured at the equilibrium. According to Young's law [141] the cosine of this angle, also called *wettability coefficient* (k), depends on the interfacial tensions at the liquid-solid (σ_{ls}), solid-gas (σ_{sg}) and liquid-gas (σ_{lg}) interfaces:

$$k = \cos(\theta) = \frac{\sigma_{sg} - \sigma_{ls}}{\sigma_{lg}} \tag{4.1}$$

and it is usually employed as an estimation of the wettability of a surface [142]. Higher is the contact angle and lower is the wettability, lower is the contact angle and higher the tendency of the fluid to spread and wet the surface.

In droplet microfluidics it is fundamental that the dispersed phase has a high contact angle while on the contrary the continuous phase should completely wet the solid. This condition makes the dispersed phase to be never in contact with the solid walls of the channels since it is constantly surrounded by a thin film of the continuous phase which wets the solid surface. In this case the droplet breakup process inside a microfluidic droplet generator is mostly governed by the interaction between the fluids and the geometrical confinement rather than by the wetting properties of the fluids on the solid surface. Moreover the absence of direct contact between the dispersed phase and the channel walls prevents the interaction of droplet contents with the material which makes up the channel walls. This peculiarity is fundamental to avoid adsorption of substances carried by the droplets in biological applications as well as to prevent the degradation of the channel walls if droplets contain aggressive chemical species.

This work had the aim to make flow water droplets inside the microfluidc channels since, among the most interesting employments of optofluidics, biological applications seems to get the best acknowledgments and most of biological samples need to be dispersed in water solutions.

The requirement for a continuous phase which is immiscible with water has a plenty of available solutions among oils; hydrocarbons such as decane, dodecane, hexadecane, mineral oil are normally used in microfluidics, as well as silicone oils or also vegetal oils.

All oils have usually similar wettability properties on the same substrate since they interact mostly by means of Van der Waals forces; some marked differences could be dependent on their polarizability in the presence of strongly polarized surfaces.

A detailed study of water and hexadecane wettability of lithium niobate was performed in order to characterize its properties linked to its employment in microfluidics applications and to discover possible phenomena linked to its well-known anisotropy in surface energy [143].

Measurements were conducted by depositing a liquid droplet with a volume fixed at 500nL from the needle of a syringe on the surface of the crystal and taking a picture of the droplet from two perpendicular directions. The images were analysed with an image analysis software in order to measure the contact angle of the droplets.

Measurements were performed on a set of more than 10 deposited droplets and they were repeated on the three surfaces relative to a different cut of the crystal, i.e. on each surface perpendicular to a different crystallographic axis (x-cut, y-cut and z-cut). The experiment was also repeated both for the surface pointing towards the positive direction of a crystallographic axis ($+x$, $+y$, $+z$) and for the opposite one ($-x$, $-y$, $-z$).

The pictures were taken pointing the cameras along the other two crsytal axes parallel to

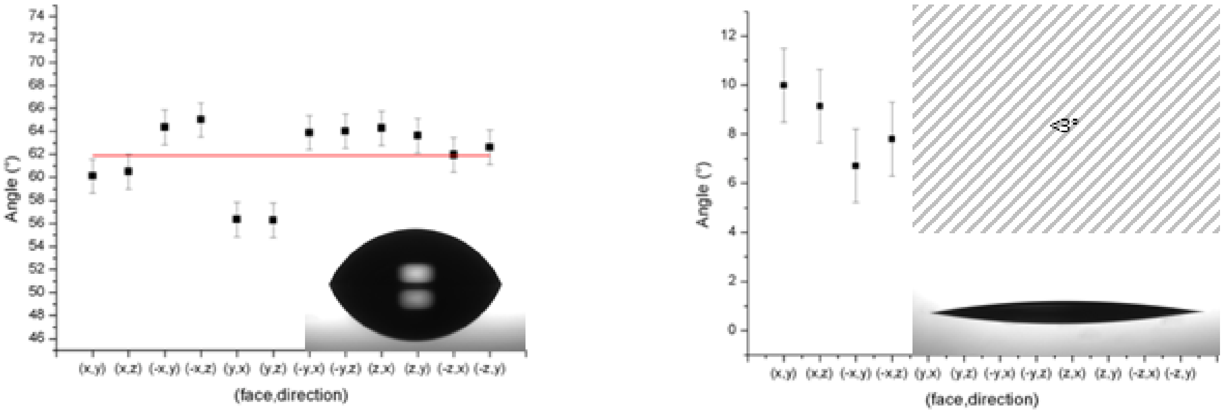

Figure 4.13: Contact angle (CA) measurements on lithium niobate surface for different crystals cuts and different cristallographic directions for water (on the left) and hexadecane (on the right). The red line represents the average of all CA determinations.

the cut surface.

Commercial double polished wafers of lithium niobate from Crystal Technology were used and before each measurement their surfaces were cleaned by a standard procedure putting them for 15 min in subsequent sonicating baths of: soap and DI water, DI water, isopropanol and acetone.

The results of the measurements are reported in fig.4.13. As can be seen hexadecane wets completely all the surfaces of the crystal since the contact angle is always less than 10°. Water instead has an average wetting angle of 62°±1° that indicates a moderate hydrophobicity of lithium niobate.

The contact angle measured along the two perpendicular directions parallel to the surface, that means from the two perpendicular cameras, are always comparable indicating that deposited droplets are not pinned along a direction more than the other. On the contrary some differences between crystal cuts are present, nevertheless these discrepancies are not so significant to imply a different behavior of the crystal surfaces for microfluidics applications and they are compatible with different humidity or temperature conditions inside the laboratory which could not be controlled.

The moderate hydrophobicity and the high oleophilicity could stand for the effective applicability of lithium niobate for generating water droplets in hexadecane but a higher hydrophobicity is needed to make this crystal comparable with standard polymeric materials such as PDMS and PMMA employed in microfluidics which has a water contact angle typically ranging from 100° to 120°.

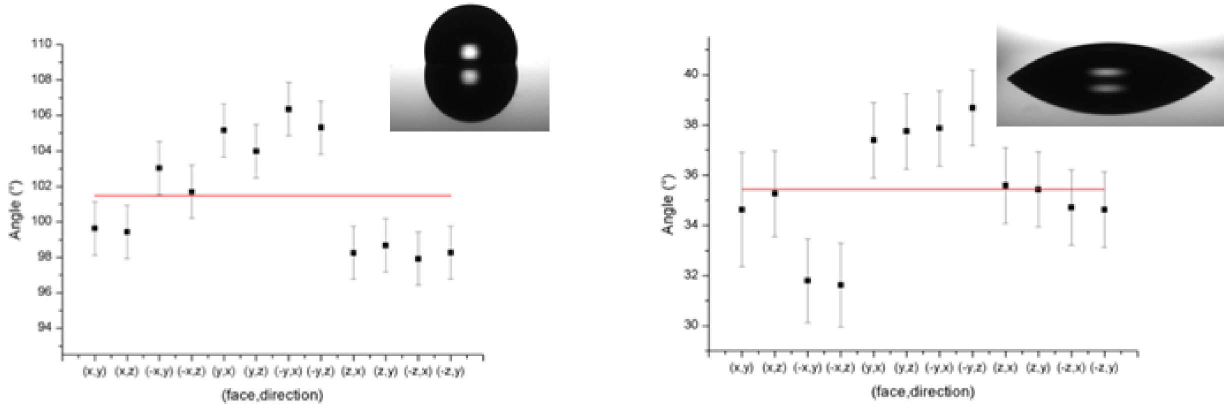

Figure 4.14: Contact angle measurements on lithium niobate surface for different crystals cut and different cristallographic directions after functionalization with a solution of OTS in toluene at a concentration of 100μM, for water (on the left) and hexadecane (on the right). The red line represents the average of all CA determinations.

Consequently the possibility of functionalizing the surface of the crystal was taken into account and a functionalization process was studied. Crystals were exposed to UV irradiation and then dipped in a solution of octadecyltrichlorosilane (OTS)[2] in toluene at a concentration of 100μM. The UV light exposure allows to clean the surface and promote the formation of -OH ligands on the surface in order to better favour the condensation reaction needed for the bonding of the OTS molecules with the surface oxygen atoms [144, 145]. The result is a Self Assembled Monolayer (SAM) of OTS on the surface of the crystal which displays long hydrocarbon chains with a high hydrophobicity [146]. The crystals were finally rinsed with acetone in order to remove possible unreacted OTS residuals.

The contact angle measurements on functionalized lithium niobate crystals are shown in fig.4.14. As can be seen contact angles of water and hexadecane were both raised: the first reaches an average value of $(101 \pm 1)°$ and the second one goes up to $(35 \pm 1)°$. These results are perfectly comparable with literature values for PDMS which exhibits a contact angle of water around $100° \div 110°$ and a contact angle of hexadecane of $\sim 35°$ [147].

A last observation is on the dispersion of the measurements obtained on the different crystal surfaces and directions: also in the case of a surface exhibiting OTS molecules the data are scattered with a deviation from the average value similar to that of the case of bare lithium niobate but with a completely uncorrelated trend. This fact confirms that the dispersion of measurements is due to the poor reproducibility of laboratory conditions

---

[2] octadecyltrichlorosilane: $CH_3(CH_2)_{17}SiCl_3$; CAS Number 112-04-9; Mm= 387.93g/mol; density 0.984g/ml.

rather than to different surface properties of the crystal cuts.

4.7 Microfluidic Channels Functionalization

The sealings described earlier imply the top wall of the microfluidic channel to be made up of a different material rather than lithium niobate[3]. This makes the upper wall of the channels having different wetting properties from the other ones. Moreover the first tests on the realized T-junctions and cross-junctions after sealing showed they could not effectively produce water droplets in oil. The injected fluids enter a co-flow regime which prevents the formation of droplets (see fig.4.15). In addition water pinned somewhere indicating the absence of the needed oil film at the surface.

This is due to the too low hydrophobicity of lithium niobate which could have been decreased also by the plasma treatment and the UV light exposure needed during the sealing.

The solution was the functionalization of the microfluidic channels with octadecyltrichlorosilane following the preliminar wettability study discussed in 4.6. A 100μM octadecyltrichlorosilane solution in toluene was fluxed through the channels at a flow rate of 20μl/min for 15min. Then pure toluene was fluxed to remove the residual unreacted molecules. Heating the device at 65°C for 30min ensured the evaporation of the remaining toluene. In the case of the sealing type 1 the PDMS suffered swelling and it was imppossible flowing toluene for more than 1min; nevertheless it seems to recover its shape without damages after the thermal treatment at 65°C and the functionalization gave similar results anyway.

The image of flowing droplets inside the channels after functionalization is shown for comparison in fig.4.15.

To avoid excessive PDMS swelling other solvents like hexadecane and mineral oil were tested instead of toluene but the functionalization seemed to be short lasting indicating that OTS chains did not react at the channels surface but probably were just adsorbed. On the contrary in the case of toluene the functionalization was tested after several weeks and several days of continuous flow and no changes in the behavior of the droplet generators were observed.

---

[3] The techniques presented in the previous sections require PDMS or glass on the top wall of the channel. However this is not mandatory for the glass sealing type 3 (section 4.4.4) since glass can be replaced by a $LiNbO_3$ crystal without drawbacks.

Figure 4.15: Effect of the functionalization on the production of droplets. Starting from the top the micrographs refer to: the laser ablated T-junction before the functionalization process, and the same T-junction generating droplets after the functionalization; the cross-junction obtained with the DISCO DAD 321 dicing saw before the functionalization and the same generating droplets after it was functionalized. As can be seen in both cases droplets cannot be generated without tailoring the wetting properties of the channels surfaces.

5 Microfluidic Characterization

5.1 Experimental Set-up

The study of the droplets flowing inside the microfluidic channels was performed controlling the flow rates injected in the microfluidc chip and exploiting a fast imaging system, based on the recording of image sequences with a fast camera connected to a microscope. The same setup was used to analyse the performance of two microfluidic T-junctions obtained by laser ablation. The laser-ablated T-junction were both sealed with a PDMS layer as described in section 4.4.1 The whole experimental set-up is sketched in Fig.5.1.

Two independent automated syringe pumps PHD 2000, Harvard Apparatus were used to inject the fluids inside the microfluidc channels through flexible polyethylene tubings by Deutsche & Neumann with an internal diameter of 0.5mm and an external diameter of 1.0mm resistant to acids, bases, alchools and salt solutions up to 80°C. The tubing were connected to the syringes and the microfluidic chip through larger MASTERFLEX® silicone tubing by Cole-Parmer (OD=4mm; ID=0.8mm).

The syringe pumps pull the plunger of a syringe at a fixed speed thanks to a stepper motor. They work in a flow rate range from 0.0001μl/min to 220.82ml/min and they can be used both to infuse or withdraw. The range of flow rates explored during the experiment spread from $Q_c = 5\mu$l/min to $Q_c = 300\mu$l/min for the continuous phase while the dispersed phase flow rate Q_d ranged from 0.1 to 2 times that of the continuous phase. The injected fluids were hexadecane [1] as the continuous phase and DI water as the dispersed phase. A surfactant (SPAN®80)[2], was added to the continuous phase to reduce the interfacial tension σ between the two fluids. The surfactant concentration was set to 0.08% (w/w), which is above the critical micelle concentration (for SPAN®80 in hexadecane CMC=0.03%(w/w

---

[1] Hexadecane: $CH_3(CH_2)_{14}CH_3$, CAS number: 544-76-3, Mm = 226.44g/mol, viscosity 3cP, density 0.77g/cm^3 @ 25°C.

[2] $C_{24}H_{44}O_6$, CAS number:1338-43-8, Mm:428.62g/mol

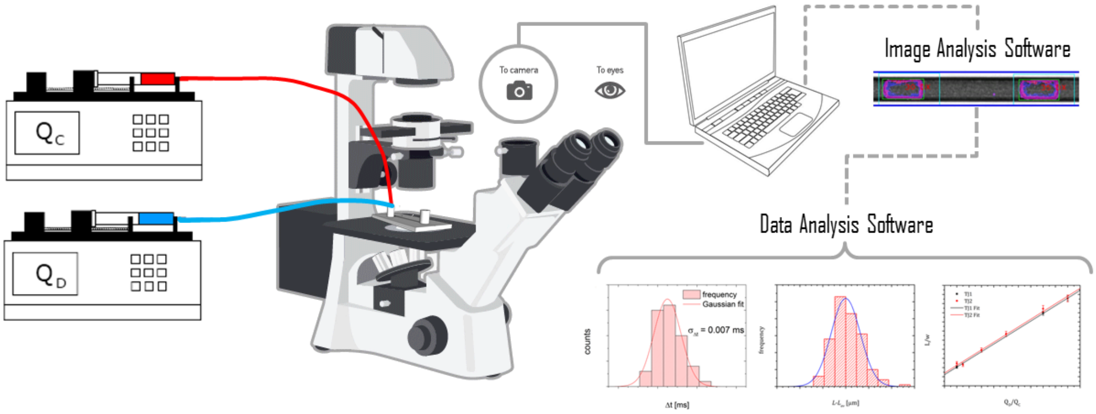

Figure 5.1: Sketch of the experimental setup employed for the measurment and the analysis of droplet length and production frequency.

[148]).

5.2 Image Recording Details and Image Analysis Software

The microscope employed in the experiment was an inverted microscope Eclipse Ti-E, Nikon with a plan 4x/0.10 objective with a 30mm working distance.

A fast camera Phantom VRI v7.3 was used to record the image sequences. The resolution of the images was 800 × 600 and a calibration was performed to determine the spatial resolution of the image which was found to be 3.46μm/px. The illumination conditions and the exposure time of a single frame were maintained fixed for each measurement while the frame rate was varied depending on the velocity of the droplets in order to get more than 10 subsequent pictures for a same flowing droplet before it exited the field of view. The exposure time was set at 20μs, short enough to avoid motion blur when higher fluxes were employed (droplets reached velocities up to $\sim$ 1m/s).

The analysis of the images was performed with the aid of an ad-hoc software developed by Enrico Chiarello, in the framework of the LaFSI group at the Department of Physics of the University of Padova.

The software is based on the analysis of the contrast of the images and is able to recognize the droplets flowing in the channel calculating their length, speed and passage time respectively. The length of a droplet is determined from each single frame while the speed and the time instant when it crosses the center of the field of view are derived by fitting its position at each frame as a function of the frame number.

The output of the software gives for each droplet its length measured in pixels, its speed in pixels/frame and the time of its passage from the center of the image in frame number.

A part of my PhD thesis was dedicated to the development of a data analysis software for the elaboration of the experimental data coming from the image analysis software, in order to perform the statistical analysis presented in the following sections.

Before discussing the results of this study, a brief discussion on the sources of errors which are due to the experimental set-up has to be mentioned.

5.3 Error contributions to droplet length and frequency determination

The two main sources of this type of errors are the quality of the image and the pumping system.

The image quality is limited by the width of the camera pixels, which is $r_{\mathrm{px}} = 3.46\mu\mathrm{m}$ with the microscope objective used in this work. Moreover, the droplet boundary could not be located exactly within a given pixel but with an uncertainty σ_{px} related to the image resolution. In order to estimate σ_{px}, it can be considered the pixel length as the maximum uncertainty connected to the border location. Consequently, by assuming an uniform probability distribution, σ_{px} can be estimated as $\sigma_{\mathrm{px}} = \frac{r_{\mathrm{px}}}{\sqrt{12}} = 0.999\mu\mathrm{m}$. Then the uncertainty on the measurement of the droplet length is $\sigma_{L,\mathrm{px}} = \sigma_{\mathrm{px}}\sqrt{2}$ that comes from the error propagation law applied to the difference between the positions of the advancing and the receding menisci. On the contrary we can suppose the contribution of this error source is negligible in the measurement of the time interval between two consecutive droplets because the time of passage of a droplet at the center of the image is calculated as the intercept of the linear fit of more of 10 positions of the advancing meniscus as a function of time.

The syringe pumps employed to inject the fluids inside the microfluidc channel have a high control on the injected flow rate (accuracy within 0.35% and reproducibility within 0.05% declared by the manufacturer), however the syringes used to pump the fluids could have not a regular diameter along all their length and also the tubing connecting the syringes to the microfluidic chip inlets can suffer small elastic or plastic deformation under the imposed pressures ranging from some tenth of a bar up to about 1 bar.

All this features can add systematic errors to the measured length of the droplets and their production frequency which are difficult to estimate at each measurement. Sometimes this error can be avoided waiting enough time for the system to stabilize, otherwise it has to be taken into account later as an additional contribution.

In order to study this problem few measurements were performed fixing the flow rates of the dispersed and continuous phase and collecting three image sequences of about 2000÷3000 droplets at three different times: 1 minute after having set the fluxes, then again after 15 minutes and the last time after 30 minutes.

As can be seen in the example shown in Fig.5.2 there are some fluctuations on the measured time interval between two subsequent droplets Δt with a period of the order of more than 30 seconds, sufficiently long for the passage of about 1500 droplets. These fluctuations affect also the volume of the generated droplets since the dispersed phase flow rate Q_d is fixed. In a recording of a set of about 100 or even 200 droplets these fluctuations cannot be distinguished and so the relative error on the calculated average length or the calculated average time interval between droplets cannot be isolated.

Recording images sequences lasting up to few minutes for each flow rate value in the range of interest was not possible due to the high storage memory needed to record so many images with a sufficient high quality. Consequently only some tests at different flow rates ($(Q_c[\mu\text{l/min}],\ Q_d[\mu\text{l/min}]) = \{(5,5),(10,10),(20,20),(50,50)\}$) were performed and an estimation of the systematic error due to long lasting fluctuations was derived. As it can be seen in the plots of the time interval between two subsequent droplets as a function of the droplet number reported in Fig.5.2, the amplitude of the high frequency fluctuations decreases significantly after 15 min constant flow and the main deviation from the mean value is due to the low frequency fluctuation. Therefore 15 minutes were found to be a good compromise as a standard time to wait at each future measurement to dump the high frequency oscillations.

After 30 min there is a small decrease in the amplitude of the long period fluctuation but it still stands with the same frequency and it has an amplitude much greater than the dispersion of the higher frequency fluctuations.

In a measurement lasting about 100÷200 droplets this fluctuation acts as a random source

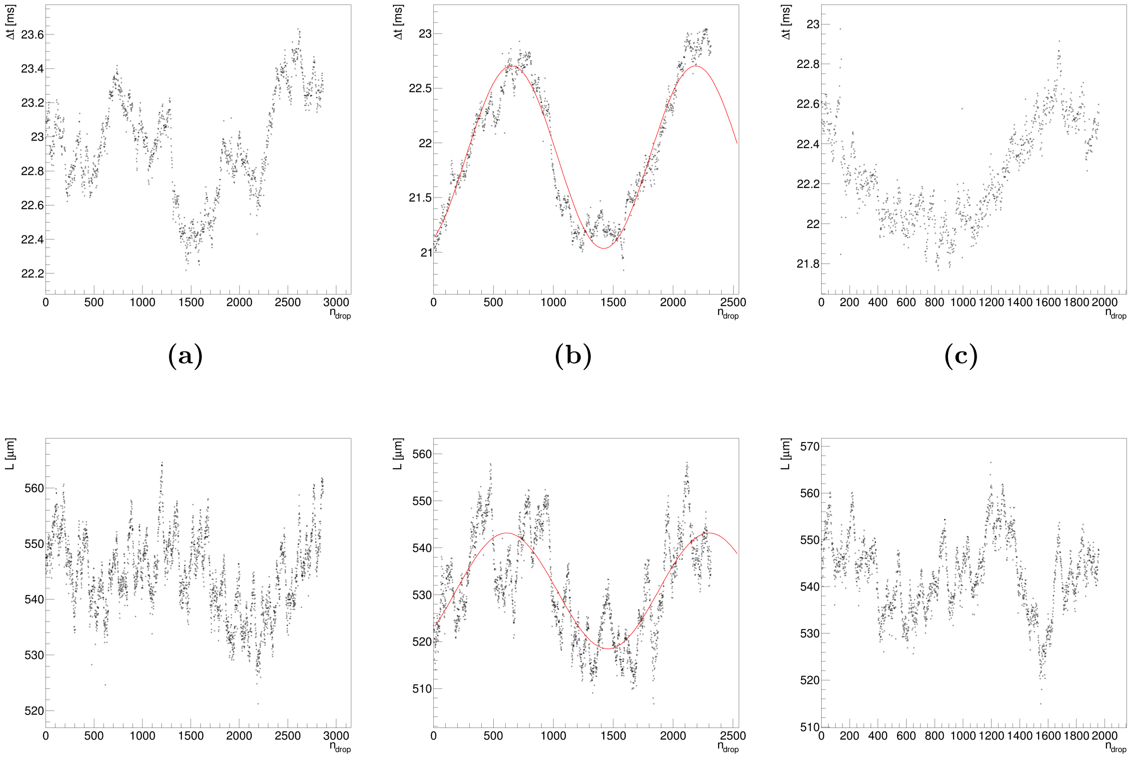

(a) (b) (c)

(d) (e) (f)

Figure 5.2: The figure shows the contribution to the dispersion of both the production frequency and the droplet length due to the fluctuations of the pumping system. In (a),(b) and (c) measurements of the time interval between two subsequent droplets lasting the passage time of more than 2000 droplets are shown as a function of the droplet number n_{drop}. In (d),(e) and (f) the droplet length measurements taken during the same experiment are shown. All plots refer to flow rates $Q_c = 10\mu\text{l}/\text{min}$ and $Q_d = 10\mu\text{l}/\text{min}$; (a) and (d) were taken after 1min wait since the fluxes were set; (b) and (e) after 15min wait; (c) and (f) after 30min wait. The red curves represent the sinusoidal fit of measurements taken after 15min wait.

of error in the determination of the average Δt which depends on the moment the measurement is performed. Since the long period fluctuation can be approximated as a sinusoidal, the probability density distribution of the measured time interval is supposed to have the form:

$$p(\Delta t) = \begin{cases} \dfrac{1}{\pi} \dfrac{1}{\sqrt{A^2 - (\Delta t - \overline{\Delta t})^2}} & , \quad \forall \Delta t \in \left]\overline{\Delta t} - A, \, \overline{\Delta t} + A\right[\\ 0 & , \quad \text{elsewhere} \end{cases} \tag{5.1}$$

where $\overline{\Delta t}$ is the mean value and A is the sinusoid amplitude. An estimation of the dispersion of Δt can be obtained as the square root of the second moment of the distribution $p(\Delta t)$:

$$\sigma_{\Delta t,\text{pump}} = \left[\int_{-\infty}^{+\infty} d\left(\Delta t\right)\ p(\Delta t) \left(\Delta t - \overline{\Delta t}\right)^2 \right]^{1/2} = \frac{A}{\sqrt{2}} \tag{5.2}$$

The amplitude of the sinusoidal oscillation was calculated for each tested couple of flow rates after 15min wait by fitting the measured Δt as a function of the droplet number (see Fig.5.2b) and it was verified to be of the same order for all tested fluxes. The dispersion $\sigma_{\Delta t,\text{pump}}$ was calculated for all long time recording tests taken after a 15 min wait and the highest one $\sigma_{\Delta t,\text{pump}} = 0.59$ ms was chosen as an estimation of the random error due to oscillating pumping.

The same procedure was followed for the estimation of the random error on the average length. In this case the low frequency fluctuations amplitude was not so high respect to the contribution of the higher frequency fluctuations, but they are surely caused by the same source since the frequency is exactly the same (see Fig.5.2e). The random error due to this contribution was estimated to be $\sigma_{L,\text{pump}} = 8.73\mu$m.

5.4 Droplet Generator Performances

An efficient and versatile microfluidic droplet generator should produce droplets in a wide range of volumes and frequencies with a very sharp distribution both of the droplet volume and the time interval between subsequent droplets.

A tiny distribution of droplet volume indeed allows for a very precise control of dispersed analyte quantities or reagents dilution and so it is the most important task for a microfluidic droplet generator.

Obviously in a passive microfluidic device, at a fixed flow rate, droplet volume is linked to droplet production frequency so that the time interval between two subsequent droplets should have a very tiny distribution to ensure a steady operation.

In order to test the performances of the T-junctions described in this work image sequences of more than 100 droplets with the capillary number Ca ranging from $5 \cdot 10^{-4}$ to 0.07 and different flow rate ratio $\phi = Q_d/Q_c$, from 0.1 to 1, where recorded to study the length and the frequency distributions.

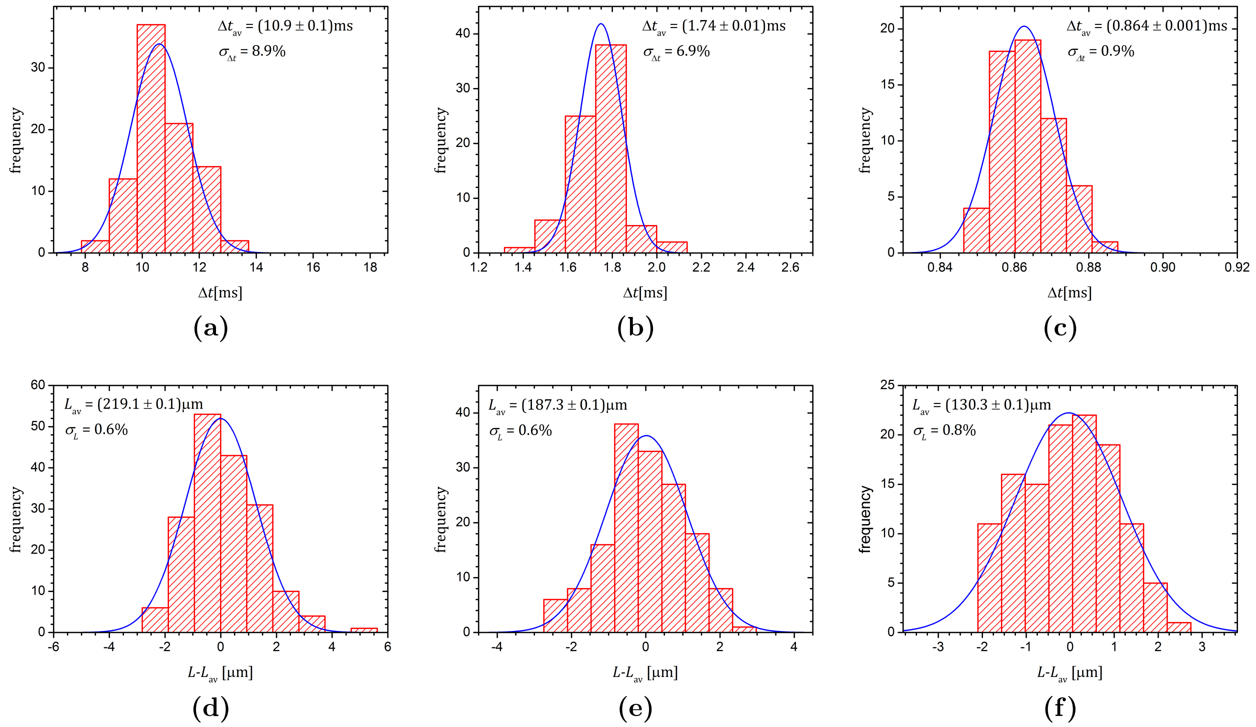

(a) (b) (c)

(d) (e) (f)

Figure 5.3: Histograms of the time interval between subsequent droplets (a,b,c) and of the deviation from the average droplet length (d,e,f) together with their Gaussian fit at the following flow rates: (a,d) $Q_c = 30\mu\mathrm{l/min}$, $Q_d = 9\mu\mathrm{l/min}$; (b,e) $Q_c = 90\mu\mathrm{l/min}$, $Q_d = 45\mu\mathrm{l/min}$; (c,f) $Q_c = 300\mu\mathrm{l/min}$, $Q_d = 80\mu\mathrm{l/min}$. The distribution are quite sharp and do not show any marked deviation from the normal distribution. The only one which seems to have a different shape is the most sharp distribution, that relative to the length at the highest flow rates: this is probably due to the fact that the overall dispersion is comparable to the random error due to the image quality which have a uniform distribution and in this case probably it is no more negligible compared to the intrinsic length dispersion of the deivce.

Droplet frequency: as explained in section 3.3.1 the droplet generation frequency (f) depends on the flow rates of the immiscible liquids and the highest achievable value of f is limited by the maximum pressure the microfluidic channels are able to sustain. The maximum frequency reached with the T-junction described in this work was $f_{max} = 1157 \pm 9\mathrm{Hz}$ at flow rates $Q_c = 300\mu\mathrm{l/min}$ and $Q_d = 80\mu\mathrm{l/min}$.

At each fixed couple of values of the flow rates the average droplet production frequency was calculated as the average of the distribution of the time interval between two subsequent droplets. In order to highlight possible asymmetries in their distribution and avoid correlations, only time intervals referring to distinct pairs where taken into account, i.e. $\Delta t_j = t_{2j} - t_{2j-1}$ with $j = 1, 2, 3, ..., N/2$ and N is the total number of droplets. No large deviations from the Gaussian distribution shape were

observed at all tested frequencies (from 92Hz up to 1157Hz) and the dispersion of the time interval distributions was always below 10% (see Fig.5.3).
Three examples of the behavior of Δt_j as a function of the ordinal number of droplet is shown in Fig.5.4: the absence of clear systematic drifts in this plot was verified for each flow rates couple and it confirms that the passage time of about 200 droplets is short enough to avoid that the fluctuations due to the pumping system are visible.

Droplet length: the length of the droplets (L) was measured in pixels as the distance between the very first border of the advancing meniscus and the last contour of the receding meniscus and then converted in micrometers according to a previous calibration of the image with a standard calibration sample.
The length dispersion was obtained as the standard deviation of the length distribution and it was less than 3% for all tested flow rates, in most cases less than 2%, perfectly aligned to microfluidic standards (see table 5.1). Three example at three different droplet production frequencies spanning the whole tested range are reported in Fig.5.3(d),(e),(f). As can be seen the length dispersion does not change significantly with the frequency so that the performances of the T-junction does not depend strongly on flow rates ensuring a high versatility of the device. It is worth mentioning that the previously discussed systematic error due to the pumping fluctuations and affecting the droplet length determination influences mainly the mean value of the length distribution rather than its dispersion.In fact if the recording time of a measurement is quite shorter than the fluctuation characteristic period of the pumping system, all measured droplet lengths in a same record will be affected approximately by the same error in the injected flow rates. Therefore length distribution dispersion is a good estimation of the device performances.

5.5 Comparison with Theoretical Models

The comparison of the experimental results with the other described in the literature and with the theoretical scaling laws is useful both for a better understanding of the physical behavior of the device and for providing a prediction of its operation as a function of those

Geometry	Material	Fluids	Volume range [nL]	Volume dispersion	Ref.
T-junction	$LiNbO_3$ sealed with PDMS	Water in Oil	$0.8 \div 10.4$	<3%	This work
T-junction	PDMS + external glass to improve stiffness	Water in Oil	$0.2 \div 2.5$	<6%	[1]
flow-focusing	Polyurethane	Monomers in Water	$0.1 \div 5$	<3%	[149]
T-junction	PDMS	Water in Oil	$1 \div 70$	<3%	[2]
Multiple T-juntion	Glass sealed with PDMS	PCR-mix in Oil	$2 \div 4$	<4.8%	[150]
T-junction	Silicon sealed with Glass	Oil in Water	$0.2 \div 20$	<2%	[151]

Table 5.1: Performances comparison between the droplet generator presented in this work and other devices reported in literature.

external variables that can be controlled by the user.

The first observation to be made is the identification of the droplet production regime. As stated before this work is directed to the coupling of a channel waveguide to the microfluidic channel for illuminating droplets, thus bigger plugs touching the channel walls are preferred and the squeezing regime is the right way to obtain such type of droplets. Although the before mentioned tests on the volume dispersion and frequency of the droplets were performed in a wide range of flow rates covering both the squeezing and an intermediate squeezing-to-dripping regime, the following detailed analysis that is going to be presented here was limited to the squeezing regime. The employed fluxes were $Q_c = 5$, 7, 10, 12, 20, 30, 35, 40μl/min and $Q_d = \{0.1, 0.2, 0.3, 0.5, 0.7, 1, 1.5, 2\}\times Q_c$.

The identification of the droplet production regime can be deduced by two ways:

- by looking at the droplet while it is generated: as described in section 3.2 in the case of squeezing the dispersed phase entering the main channel tends to obstruct the entire channel before it is pulled by the continuous phase until breakup. The produced droplets have a length bigger than the width of the channel since they fill

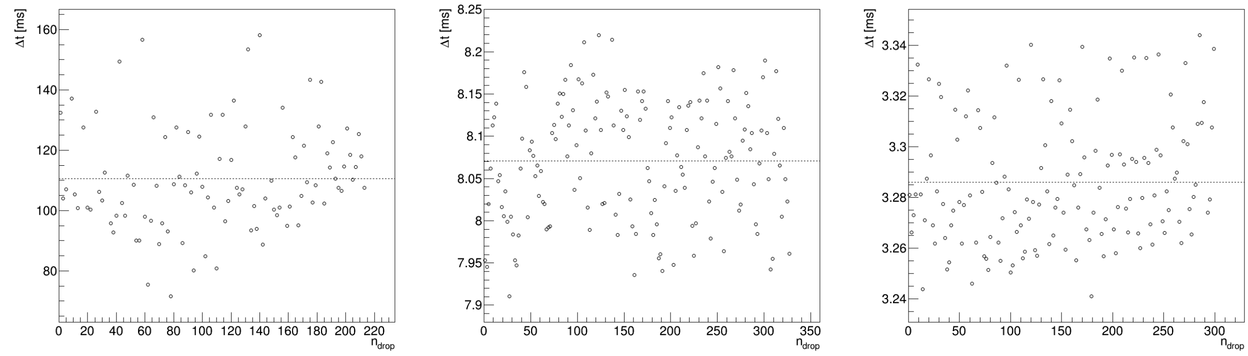

(a) **(b)** **(c)**

Figure 5.4: Examples of the distribution of the time interval between subsequent droplets (Δt) plotted as a function of the droplet number (n_{drop}) for: (a) $Q_d = 1\mu\text{l/min}$, $Q_c = 10\mu\text{l/min}$; (b) $Q_d = 30\mu\text{l/min}$, $Q_c = 20\mu\text{l/min}$; (c) $Q_d = 70\mu\text{l/min}$, $Q_c = 35\mu\text{l/min}$. The dashed line represents the average value $\overline{\Delta t}$.

it entirely; on the contrary in the dripping regime the shear force is quite intense to tear off the droplet before it obstructs completely the main channel and the generated droplets usually have a mean radius smaller than the main channel width. In the whole tested range the droplets have always a length bigger than w_c and they seem to obstruct the major part of the main channel before the dispersed phase neck starts to shrink. Some examples are shown in Fig.5.5: as can be seen the neck of the dispersed phase detaches from the lateral wall of the vertical channel only after the tip has invaded almost completely the main channel;

- by studying the dependence of the droplet volume by the capillary number: as it can be deduced by comparing the works of Thorsen *et al.* [99] and Garstecki *et al.* [100] both squeezing and dripping regime are possible in a T-junction depending on the value of the capillary number and each regime is characterized by a different dependence of the droplet volume V on Ca. As proved later by de Menech *et al.* [106] via a numerical simulation based on a phase-field model, there is a quite sharp transition from the squeezing to dripping at about Ca = 0.015 and the slope of the decreasing droplet volume against Ca increases abruptly. Therefore the value of Ca and the trend of V can be used as an identifier for the droplet production regime. In the analysis presented in this section, all tested values of Ca are lower than 0.015 so that all results should be referred to the squeezing regime.

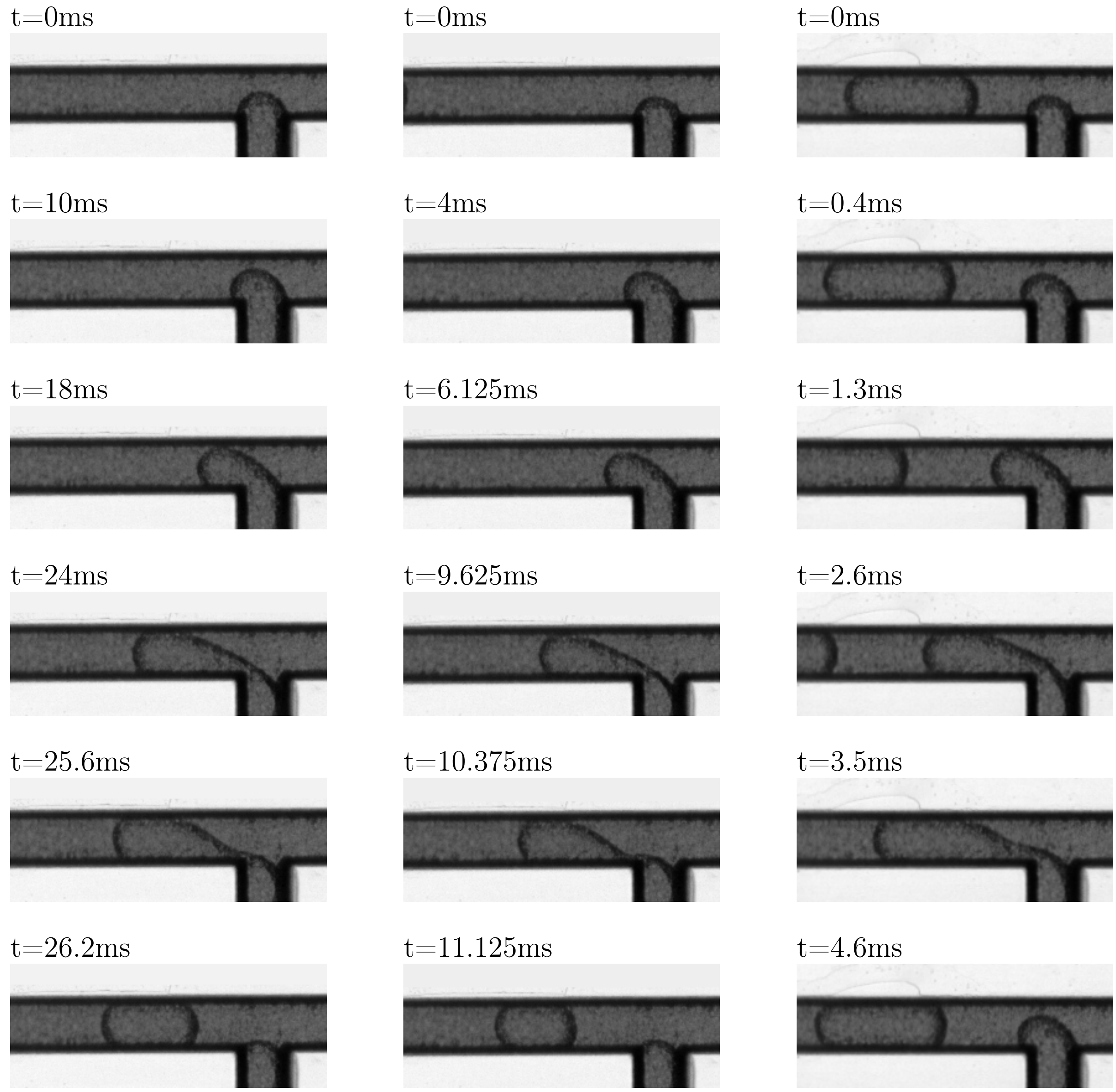

(a) $Q_c = 20\mu\text{l/min}$ $Q_d = 2\mu\text{l/min}$

(b) $Q_c = 40\mu\text{l/min}$ $Q_d = 4\mu\text{l/min}$

(c) $Q_c = 40\mu\text{l/min}$ $Q_d = 40\mu\text{l/min}$

Figure 5.5: Microscope images of droplet breakup sequence at three different set of flow rates. As can be seen comparing the third and the fourth images of each vertical sequence, the dispersed phase tip obstructs almost completely the main channel before the neck starts to shrink.

5.5.1 Analysis of the Droplet Production Frequency

The droplet production frequency f was analyzed at each fixed value of $\phi = Q_d/Q_c = \{0.1, 0.3, 0.5, 0.7, 1.0, 1.5, 2.0\}$ as a function of Ca with the continuous phase flow rate Q_c spanning from $5\mu\text{l/min}$ up to $40\mu\text{l/min}$. As observed by Christopher *et al.* [1] (see section 3.3.1) a linear dependence of $\log(\bar{f})$ on $\log(\mathrm{Ca})$ was found, where $\bar{f} = \frac{\mu_c w_c}{\sigma} f$ is the rescaled frequency (see eq.(3.12)). Some points at low Ca and low ϕ appear to deviate from the expected linearity (see in particular Fig.5.6(a),(b),(c),(d)). It is important to stress that these points are referred to the lowest flow rates set in this work which are surely those affected by the largest uncertainty due to pumping system fluctuations. Nevertheless they present a systematic deviation from the expected trend providing that Ca and ϕ are sufficiently low. This effect involves values of Ca out of the range $10^{-3} < Ca < 0.5$ investigated by Christopher *et al.* [1] and also below the range $\mathrm{Ca} > 9.7 \cdot 10^{-4}$ described in the paper by Garstecki *et al.* [100][3]. This could stand for a new regime at low capillary numbers but a deeper investigation is needed to state that.

Then linear fits of $\log(f)$ against $\log(\mathrm{Ca})$ were performed for all data collected with no surfactant added to the continuous phase, excluding the points with $Ca < 9.7 \cdot 10^{-4}$ which could refer to another regime (Fig.5.6). The results show angular coefficients $(1 - \delta)$ independent of ϕ. A similar result was obtained in the case of surfactant added to hexadecane where there was no need to exclude points since Ca is always greater than 10^{-3} due to the lower interfacial tension σ (Fig.5.7). The average slope of the fitting lines were found to be comparable to the case without surfactant.

Therefore it can be stated that the exponent $(1 - \delta)$ of the power law linking $\bar{f}$ to Ca is independent of the interfacial tension σ and an average value can be obtained from all calculated slopes: from the data collected in this work the average exponent is $1 - \delta = 1.29 \pm 0.01$. The results are summarized in Fig.5.8.

Recalling the relation proved in Christopher *et al.* [1] it has to be expected that the rescaled droplet volume $\bar{V} = \frac{V}{h w_c^2}$ will be proportional to Ca^{δ} for each fixed value of ϕ.

---

[3] These ranges are not explicitly reported in the original papers but have been obtained by calculating Ca from the reported viscosities, interfacial tensions, continuous phase flow rates and geometrical dimensions of the devices described in those papers.

5.5.2 Analysis of the Droplet Length

In literature the most stressed scaling relation describing the T-junction is the linear dependence of the droplet length (or volume) on the flow rates ratio $\phi = Q_d/Q_c$. Plots of the average rescaled length of droplets $\bar{L} = L/w_c$ as a function of the flow rate ratio ϕ and measured at different values of the continuous phase flow rate Q_c are reported in Fig.5.9 in the case of pure hexadecane as continuous phase ($\sigma = 41\text{mN/m}$) and in Fig.5.10 when the Span$^{®}$80 surfactant was added at a concentration 2.7 times the C.M.C. ($\sigma = 15mN/m$).

Apart from the points at the lowest flow rates ratios for the series at $Q_c = 5\mu\text{l/min}$ with no surfactant, which seems to be a systematic deviation from linearity, the other points appear to agree with a linear relation between $\bar{L}$ and ϕ. It has to be noticed that a lower interfacial tension gives rise to shorter droplets since less energy is needed to increase liquid-liquid surface and a larger ratio of droplet surface over droplet volume is allowed. Although measured average length shows good linearity, the intercepts of the lines differ from unity and depend on the capillary number Ca since they depend on the continuous phase flow rate Q_c and also on the interfacial tension σ. Therefore the model of Garstecki et al. [100] cannot effectively describe these results.

A dependence of the intercept of the linear relation between $\bar{L}$ and ϕ was presented by Christopher *et al.* [1] (see eq.(3.9),(3.10)). However, as the authors observed, their model doesn't reproduce the actual dependence of the droplet volume on Ca.

A deeper insight on the question of the intercept is thus needed. In order to easily compare the experimental results to the theoretical models mentioned in section 3.3.1 let the discussion switch from the rescaled length $\bar{L}$ to the rescaled volume $\bar{V} = \frac{V}{w_c^2 h}$. Suppose that the droplet flowing in the main channel could be approximated as made by Van Steijn *et al.* [2] (see eq.(3.15)), then its length can be used to calculate the volume of the droplet which will show a similar linear dependence on ϕ. The same conversion can be applied to the intercept β of each fitting line of the relation $\bar{L}(\phi)$ at a different Q_c (i.e. at a different Ca), obtaining the intercept for the rescaled volume, that means $\bar{V}_{\text{fill}} = \frac{V_{\text{fill}}}{h w_c^2}$.
Now plotting $\bar{V}_{\text{fill}}$ as a function of Ca the power law experimentally verified for the droplet volume is recovered also for the intercept (see Fig.5.11):

$$\bar{V}_{\text{fill}}(\text{Ca}) = \bar{V}_{\text{fill}}^{(0)} \text{Ca}^{\delta} \tag{5.3}$$

The red line represents the above relation imposing $\delta = -0.29$ as deduced by the discussed analysis on the relation $\log \bar{f} = (1-\delta)\log \mathrm{Ca} + \mathrm{constant}$ and leaving $V_{\mathrm{fill}}^{(0)}$ as a free parameter. The empirical law seems to reproduce correctly the trend of the experimental data. It is important to stress that this behavior seems to be independent of the interfacial tension σ since in both cases with or without surfactant added to the continuous phase, $\bar{V}_{\mathrm{fill}}(\mathrm{Ca})$ follows the same trend.

In the graph the intercepts predicted by the main theoretical models mentioned previously are reported as a comparison. At the highest values of the capillary number the data are quite in a good agreement with the theoretical models, in particular with those of Garstecki *et al.* [100] and Van Steijn *et al.* [2]; the power law dependence of $\bar{V}_{\mathrm{fill}}$ on Ca becomes clear only at very low values of Ca, below $5 \cdot 10^{-3}$. This could explain why it has been neglected in the past since very low flow rates have to be reached for this effect to be effectively observed and normally low fluxes implies low droplet production frequency which is not a target for most applications.

The last question is the slope of the fitting lines describing the trend of the droplet length with the flow ratio ϕ. Again, following the predictions of Van Steijn *et al.* (see eq.(3.15)), the length can be used to estimate the volume and the slope α becomes α_V in the equation $\bar{V}(\phi) = \beta_V + \alpha_V\phi$. Looking at the dependence on Ca of the slope α_V it cannot be derived any clear trend (see Fig.5.12). The easiest hypothesis is to assume α_V to be constant over all the range of Ca describing the squeezing regime as supposed by most theoretical models: Garstecki *et al.* [100] supposed $\alpha = 1$ in the absence of flow in the gutters but they left it as a free parameter of order 1 to account for that; Christopher *et al.* [1] stated $\alpha = \frac{\Lambda}{\bar{b}} = \frac{w_d}{w_c}\bar{b}$ and under the hypothesis that $V \approx Lbh$ they deduced $\alpha_V = \Lambda$ which in the case of the present study is 1; Van Steijn provides an equation to calculate α_V depending on the geometry (see eq.(3.25)) which gives for the T-junction described here $\alpha_V = 1.27$. Thus a quite simple law can be proposed to express the dependence of the droplet volume both on Ca and ϕ:

$$\bar{V} = \bar{V}_{\mathrm{fill}}^{(0)}\,\mathrm{Ca}^{\delta} + \alpha_V\,\phi \tag{5.4}$$

This empirical law confirms the expected linear relation between the droplet volume and the flow rate ratio ϕ characterizing the squeezing regime, as demonstrated by previous works on the T-junction. However it also includes in the intercept the dependence of $\bar{V}$ on Ca at fixed ϕ, firstly observed experimentally by Christopher *et al.* [1].

An additional information from this empirical law is that the dependence on Ca relies only on the first term which refers to the volume gained by the droplet before it is almost completely filling the main channel. That means the ratio between viscous and capillary forces is fundamental in the very first stage of droplet formation and affects markedly the droplet volume at very low values of Ca. To the best of the author's knowledge this result has not previously reported and could stand for a starting point towards an extension of existing theoretical models to low capillary numbers.

5.6 Device Reproducibility

In order to test the reproducibility of the whole fabrication process a reduced set of measurements were performed on a second device with the same characteristics of that employed in the analysis discussed in this chapter. All steps from the laser ablation to the sealing and the functionalization were repeated at the same conditions for both devices so that they represent two copies of the same microfluidic chip. The measurements of the dimensions of the channels were $w_c = 125.1 \pm 0.8\mu$m, $h = 99.5 \pm 0.7\mu$m for the T-junction used in the previous analysis (TJ2) and $w_c = 126.3 \pm 0.6\mu$m, $h = 90 \pm 2\mu$m for the other (TJ1).

The length of the produced droplets was measured for both devices using hexadecane with 1%(w/w) SPAN$^{®}$80 surfactant added as the continuous phase and DI water as the dispersed phase at $Q_c = 10\mu$l/min and 30μl/min, varying the dispersed phase flow rate Q_d from $0.1{\times}Q_c$ to $1.0{\times}Q_c$. The results are shown in Fig.5.13: again the linear relation between $\bar{L}$ and ϕ is verified and as can be seen the devices show a perfectly matching response in the tested flow rate range. This is the proof of the reproducibility of fabrication steps as a whole.

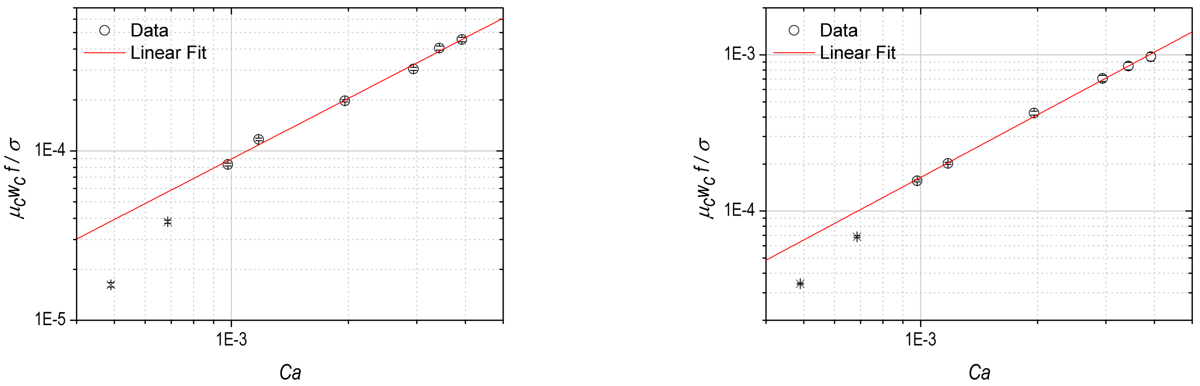

(a) $\phi = 0.1$ **(b)** $\phi = 0.3$

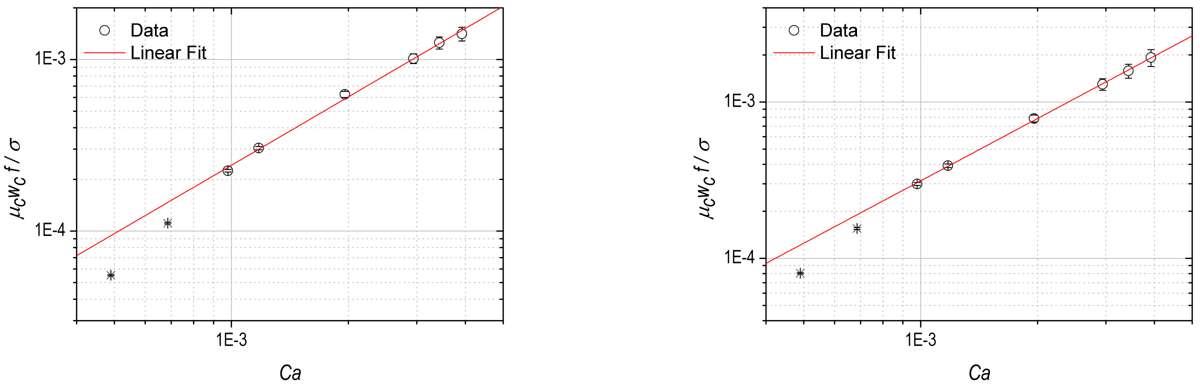

(c) $\phi = 0.5$ **(d)** $\phi = 0.7$

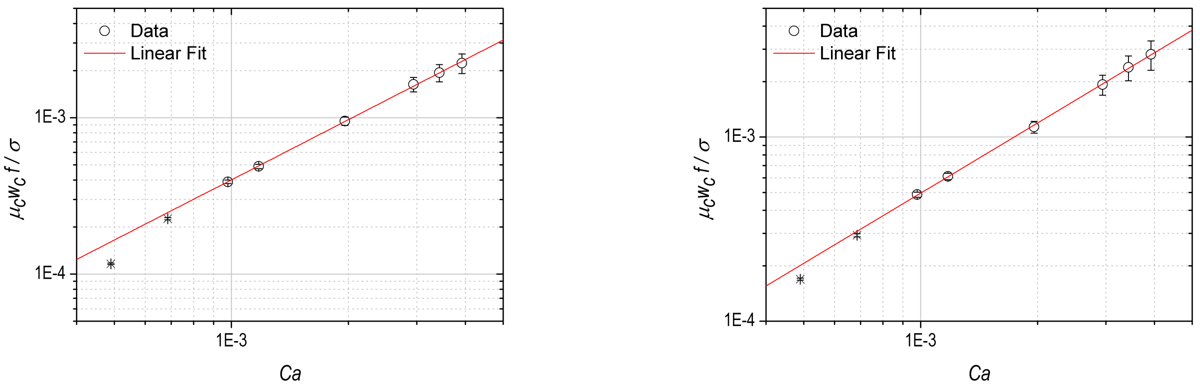

(e) $\phi = 1.0$ **(f)** $\phi = 1.5$

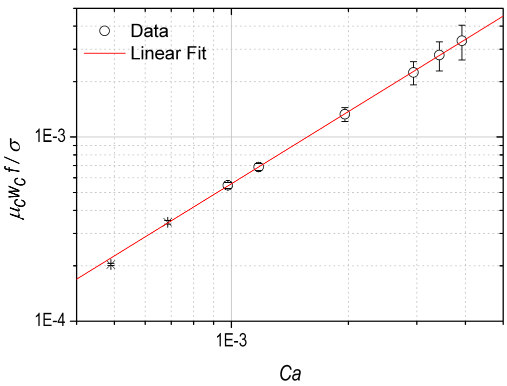

(g) $\phi = 2.0$

Figure 5.6: Analysis of droplet production frequency in the case of pure hexadecane as continuous phase (no surfactant added, $\sigma = 41\text{mN/m}$). The plots show the rescaled frequency $\bar{f} = \frac{\mu_c w_c}{\sigma} f$ as a function of Ca at fixed flow rate ratios ϕ. The red line represents the linear fit of the experimental data performed excluding the points at Ca$< 9.7 \cdot 10^{-3}$ which are indicated with a cross ($\times$).

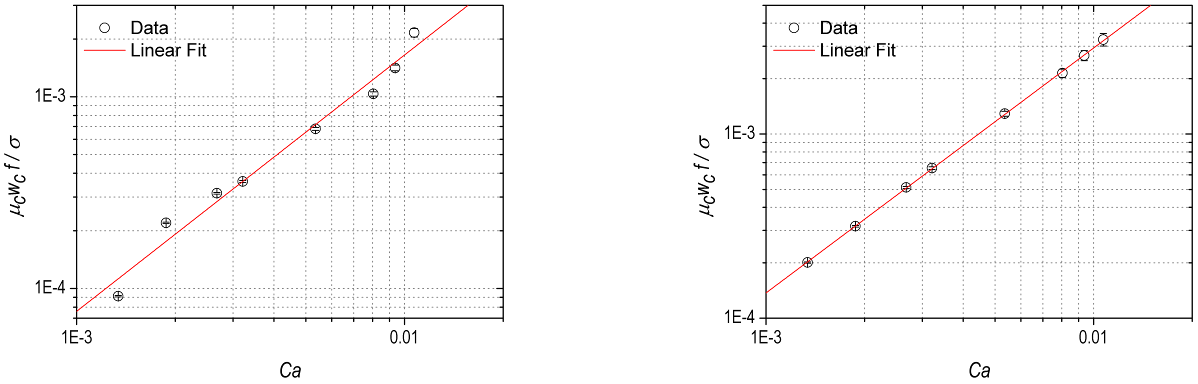

(a) $\phi = 0.1$ **(b)** $\phi = 0.3$

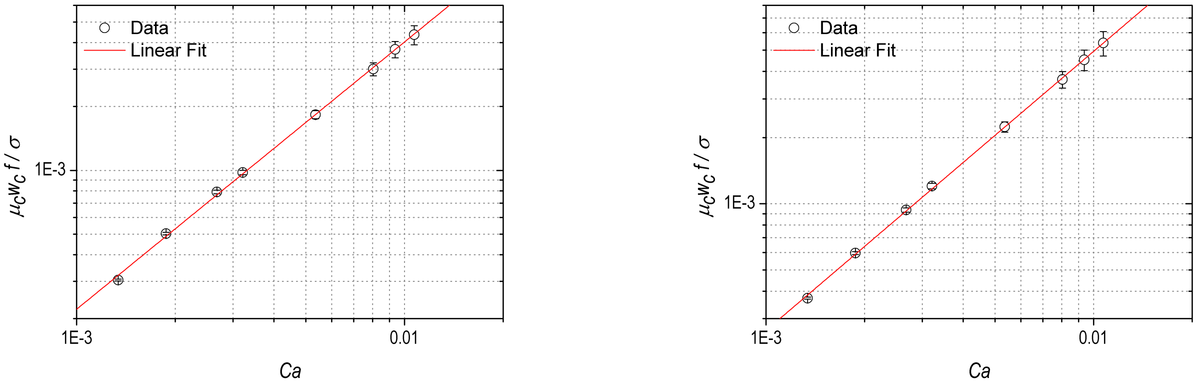

(c) $\phi = 0.5$ **(d)** $\phi = 0.7$

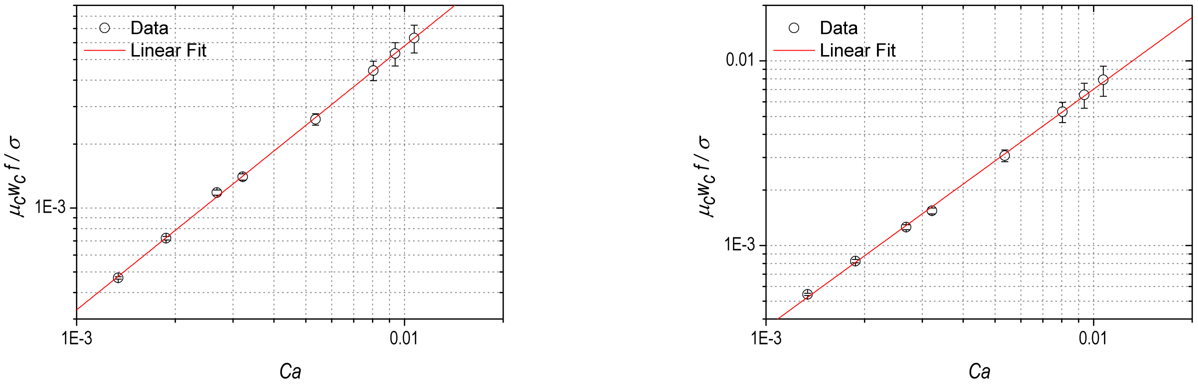

(e) $\phi = 1.0$ **(f)** $\phi = 1.5$

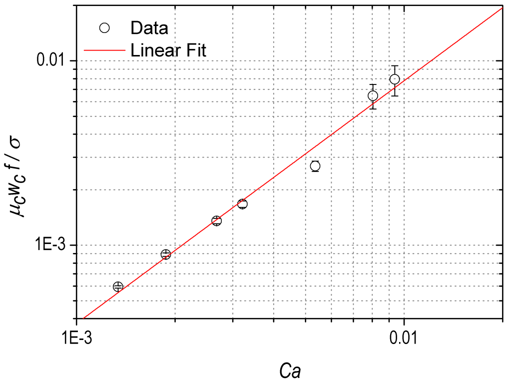

(g) $\phi = 2.0$

Figure 5.7: Analysis of droplet production frequency in the case of hexadecane with added 0.08%(w/w) SPAN®80 as continuous phase (σ = 15mN/m). The plots show the rescaled frequency $\bar{f} = \frac{\mu_c w_c}{\sigma} f$ as a function of Ca at fixed flow rate ratios ϕ. The red line represents the linear fit of the experimental data.

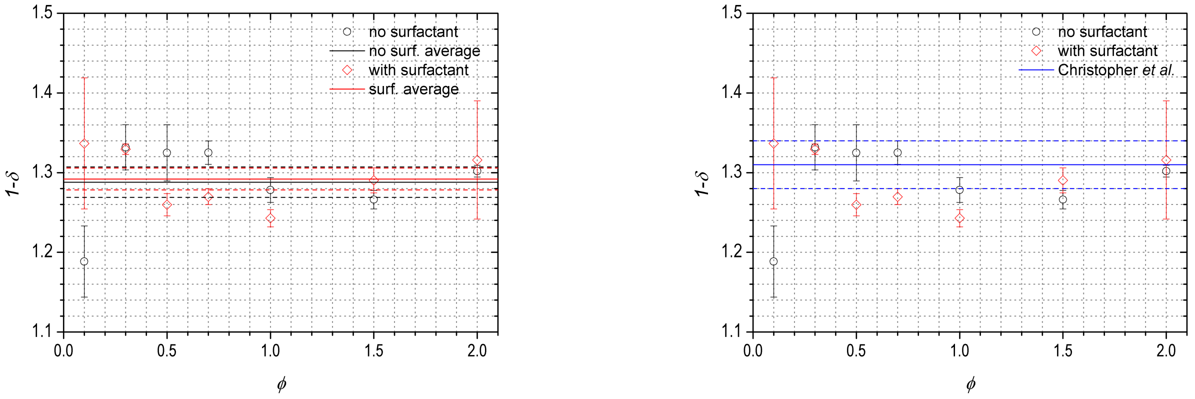

(a) **(b)**

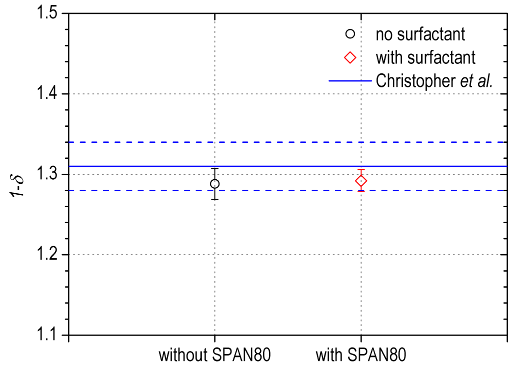

(c)

	Average	CL with [1]	Mutual CL
no SPAN$^{\circledR}$80	1.29 ± 0.02	54%	86.4%
with SPAN$^{\circledR}$80	1.29 ± 0.01	59%	
overall	1.29 ± 0.01	53%	

(d)

Figure 5.8: Details on the study of the exponent of the power law linking $\bar{f}$ to Ca: (a) $(1-\delta)$ determined from fits at different fixed ϕ for the case without (black points) or with (red points) SPAN$^{\circledR}$80 added to the continuous phase, together with their averages. Dotted lines represent the calculated error on the average of $(1-\delta)$; (b) comparison of all $(1-\delta)$ determinations with the value found by Christopher *et al.* [1]; (c) comparison between the $(1-\delta)$ averages obtained in the case without or with surfactant and the value found by Christopher *et al.* [1]; (d) averages with their confidence level with the value of Christopher *et al.* and between theirself.

(a) $Q_c = 5\mu\text{l}/\text{min}$ **(b)** $Q_c = 7\mu\text{l}/\text{min}$

(c) $Q_c = 10\mu\text{l}/\text{min}$ **(d)** $Q_c = 12\mu\text{l}/\text{min}$

(e) $Q_c = 20\mu\text{l}/\text{min}$ **(f)** $Q_c = 30\mu\text{l}/\text{min}$

(g) $Q_c = 35\mu\text{l}/\text{min}$ **(h)** $Q_c = 40\mu\text{l}/\text{min}$

Figure 5.9: Analysis of rescaled droplet length in the case of pure hexadecane as continuous phase (no surfactant added, $\sigma = 41\text{mN}/\text{m}$). The plots show the rescaled length $\bar{L} = \frac{L}{w_c}$ as a function of ϕ at fixed continuous phase flow rate Q_c. The red line represents the linear fit of the experimental data (data excluded by the fit are indicated with a cross ($\times$)).

(a) $Q_c = 5\mu\mathrm{l/min}$ **(b)** $Q_c = 7\mu\mathrm{l/min}$

(c) $Q_c = 10\mu\mathrm{l/min}$ **(d)** $Q_c = 12\mu\mathrm{l/min}$

(e) $Q_c = 20\mu\mathrm{l/min}$ **(f)** $Q_c = 30\mu\mathrm{l/min}$

(g) $Q_c = 35\mu\mathrm{l/min}$ **(h)** $Q_c = 40\mu\mathrm{l/min}$

Figure 5.10: Analysis of rescaled droplet length in the case of hexadecane with added 0.08%(w/w) SPAN®80 as continuous phase ($\sigma = 15\mathrm{mN/m}$). The plots show the rescaled length $\bar{L} = \frac{L}{w_c}$ as a function of ϕ at fixed continuous phase flow rate Q_c. The red line represents the linear fit of the experimental data.

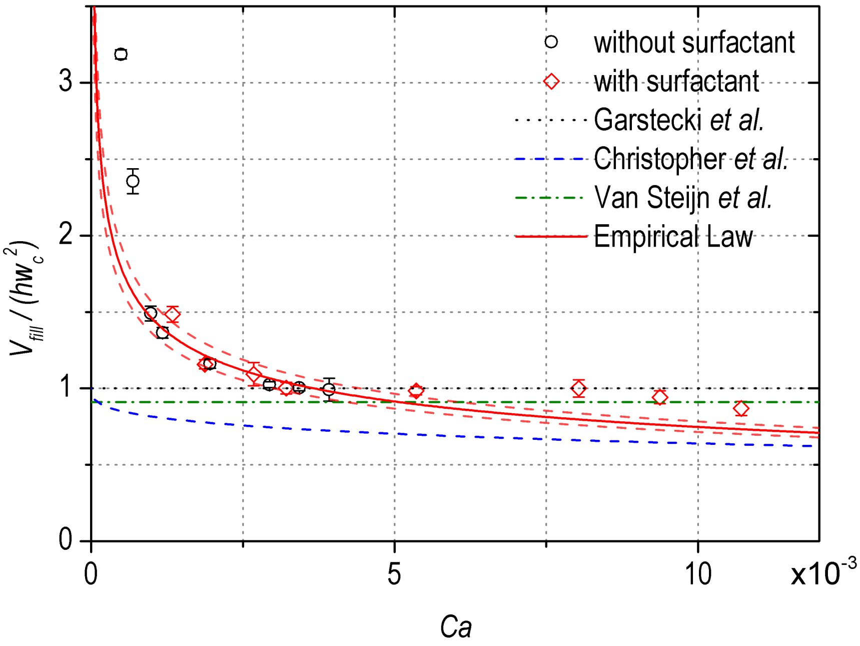

Figure 5.11: Plot of $\bar{V}_{\text{fill}}$ as a function of Ca. The red line represents the power law $\bar{V}_{\text{fill}} = \bar{V}_{\text{fill}}^{(0)}\text{Ca}^{\delta}$ where $\delta = -0.29$ is taken from the overall average in table of Fig.5.8d and the red dashed line represents the uncertainty due to $\sigma_\delta = 0.01$. The other lines represent the theoretical models from the literature described in section 3.3.1.

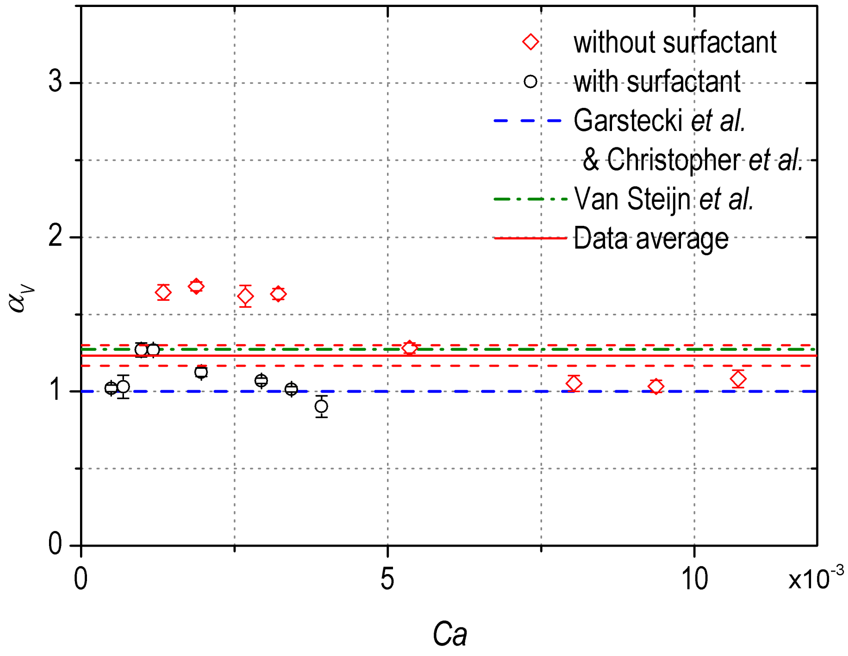

Figure 5.12: Plot of α_V as a function of Ca. The red line represents the average $\alpha_V = 1.23 \pm 0.07$ of the experimental data and the red dashed line represents the uncertainty on the calculated average value. The other lines represent the theoretical models from the literature described in section 3.3.1.

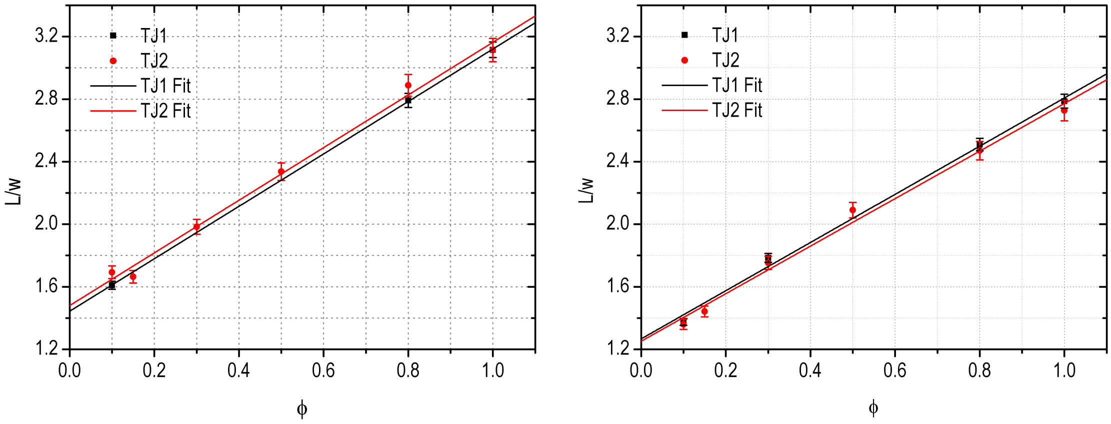

(a) $Q_c = 10\mu\mathrm{l/min}$ **(b)** $Q_c = 30\mu\mathrm{l/min}$

Figure 5.13: Comparison of the rescaled length obtained at (a) $Q_c = 10\mu\mathrm{l/min}$ and (b) $Q_c = 30\mu\mathrm{l/min}$ of hexadecane with 1% SPAN®80 with two different devices fabricated by laser ablation and sealed with PDMS with the same fabrication steps and under the same conditions.

6 Optofluidic Coupling

6.1 First tests

The first tests on the coupling of the light from the waveguides to the microfluidic channels were performed on small lithium niobate samples obtained from an x-cut commercial wafer. At first a series of z-propagating optical waveguides were realized by the process described in chapter 2 and the transmitted light was recorded with the near field setup.

A single microfluidic channel was engraved on the surface perpendicularly to the waveguide, dividing it into two facing parts, one injecting the light signal and the other one collecting the output. By this way the optimal alignment of the input and output waveguides was ensured. The same approach was used on a series of parallel waveguides.

Both laser ablation and mechanical dicing techniques were exploited to engrave different samples. The collecting objective employed in the near field setup was chosen with a working distance of 1cm. By this way it was posssible to pull the objective towards the sample and point its focus inside the crystal as far as the channel walls without knocking the sample surface.

The first test on the coupling of the signal across the microfluidic channels were performed on the open channels without any sealing, with the same configuration of the near-field setup employed for the characterization of the waveguides (see section 2.5).

The key parameter to be studied in this opto-fluidic system is the light transmitted across the microfluidic channel.

In the case of the laser ablated channels, the light injected in the input waveguide was efficiently confined and propagated till the lateral wall of the microfluidic channel. It was experimentally verified that a well defined image could be indeed recorded pointing the objective focus to the channel side surface. Nevertheless no intensity was measured exiting from the outer face of the sample indicating that no excitation of the outlet waveguide was possible.

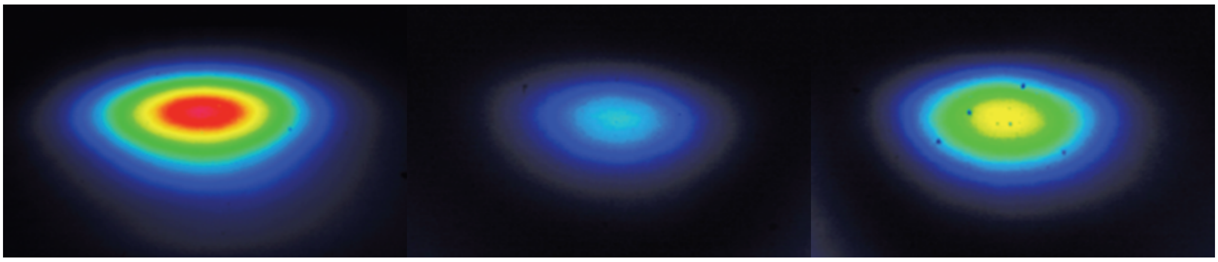

(a) $I/I_0 = 100\%$ **(b)** $I/I_0 = 38\%$ **(c)** $I/I_0 = 76\%$

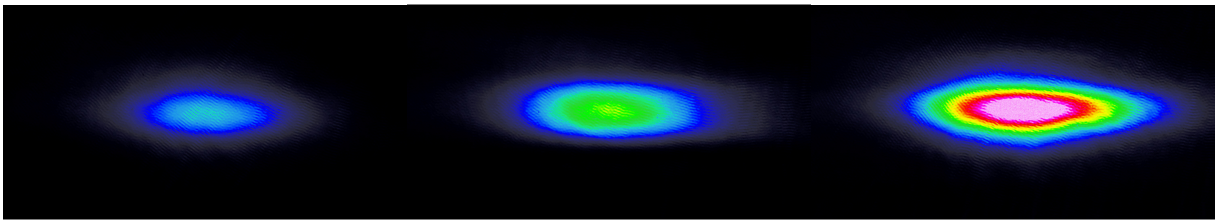

(d) **(e)** **(f)**

Figure 6.1: Example of the near field images of a waveguide coupled to a 200μm wide microfluidic channel: on the top (a) TE single mode of a waveguide before the channel was engraved, (b) after the channel was engraved and filled with air, (c) after the channel was filled with hexadecane; on the bottom images of a TM single mode waveguide crossing a 200μm microfluidic channel (d) filled with air, (e) water and (f) hexadecane.

In order to reduce light diffraction at the exit from the inlet waveguide and favour the excitation of the collecting waveguide, a drop of hexadecane was placed on an extremity of the channel in order to fill it by capillarity and allow for a better index matching between the lithium niobate crystal and the fluid inside the channel (n_{hexa}=1.434 at λ=632.8nm). No changes on the output waveguide were observed.
Unfortunately the laser ablated channels absorb too much energy at the walls and are too rough to recollect the signal from the injecting waveguide making possible only the enlightenment of the fluid inside the channels but not the detection. This issue seems aligned to results discussed in literature for silica devices: to the author knowledge no examples of waveguides in the visible range, obtained by laser ablation, were reported to be able to collect the incoming signal with a configuration similar to that described here.

The case of the microfluidic channel obtained using the dicing saw was completely different. Even in the case of the open channel in air, the single mode of the output waveguide was recognizable at the near field image collected at the surface of the crystal. An example of the near-field image of a z-propagating waveguide crossing the microfluidic channel is shown in fig.6.1b. The collected intensity is the 38% of the intensity recorded before the channel was engraved. Due to diffraction this intensity is just one half of the 74% intensity obtained by simply considering the Fresnel transmission coefficients across the two interfaces $LiNbO_3$-air, air-$LiNbO_3$. Nevertheless diffraction can enhance the sensitivity of the waveguide to the refractive index change of the fluid filling the gap: as shown in the near field image recorded in the presence of hexadecane inside the microfluidic channel (fig.6.1c), intensity raises up to 2 times that recorded in the case of air, while on the other hand the transmission of a non-diffracting plane wave should increase just by a factor 1.2.

This simple preliminary test shows that the waveguides realized by titanium in-diffusion in lithium niobate combined with the micromachining performed with the dicing saw are suitable for optofluidic applications and that the signal loss across the microfluidic channel is quite low considering that the channel has a width of 200μm, much larger than the waveguide dimensions.

6.2 Experimental Set-up for time resolved measurements

In order to be able to perform time resolved measurements of fluid samples flowing along the microfluidic channel after sealing, it was mandatory to modify the acquisition system since the CCD camera employed in the near field measurements was not able to record more than 32 subsequent images.

Since in this case there is no more interest on the shape of the mode of the waveguide but the aim is to measure the overall intensity exiting from the output waveguide, a simple photodiode was used. A transimpedence was put in series to the photodiode in order to amplify the photo-generated current and convert the signal into a voltage which was monitored with an Agilent MSO-X 2012A oscilloscope (see fig.6.2). Moreover the same PHD 2000, Harvard Apparatus syringe pumps used during the droplet generator characterization were employed to inject the fluids inside the microfluidic channels.

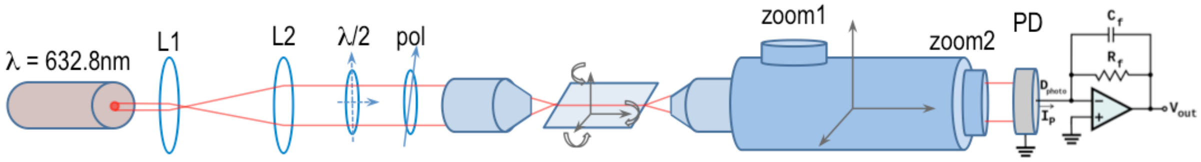

Figure 6.2: Sketch of the experimental system used to perform time resolved measurements of the transmitted intensity exiting from the collecting waveguide while fluids are flowing.

6.3 Single Microfluidic Channel

The first time resolved measurements were performed on a sample with a single microfluidic channel as those described in section 6.1. At the beginning the chip was sealed with the PDMS layer but it was observed that the optical signal from the output waveguide changed considerably with the imposed flow rate. This was due to the change in the elastic deformation of the PDMS according to the pressure inside the channel, being proportional to the flow rate of the flowing liquid.

In order to have the possibility to remove the cover, the PDMS sealing was replaced by a glass sealing type 1, but even this solution revealed to be unsuitable since after the chip was sealed and water was flown through the microfluidic channel, the waveguide signal lost more than 60% of its intensity. The explanation for that was again the deformation of the polymeric layer above the lithium niobate crystal. Indeed, after removing the covering, a PDMS ridge was found in correspondence of the microfluidic channel and it was proved to be high $0.5 \div 1\mu$m, thus masking a great part of the signal from the waveguide.

The chip was finally sealed with a glass sealing type 3 and when water was flown through the channel, no dependence on the imposed flow rate was observed. A first set of measurements was performed in order to test if the device was sensitive to the refractive index of the fluid flowing inside the microfluidic channel. Water solutions of glycerol and 2-propanol with different concentrations were prepared in order to have two sets of fluids with a progressively increasing refractive index. The values of the prepared concentrations and the respective refractive indices are listed in table 6.1.

A polyethylene tubing by Deutsche & Neumann with an internal diameter of 0.5mm and an external diameter of 1.0mm was load with small amounts of the different solutions isolated by air. The tubing was linked to the syringe pulled by the pump and to the inlet tubing of the chip and the solutions progressively injected inside the device.

Glycerol								
Concentration (w/w)	0%	6%	12%	18%	24%	32%	40%	
Refractive Index	1.333	1.340	1.347	1.355	1.362	1.373	1.384	
Viscosity [mPa·s]	1.002	1.157	1.365	1.630	1.988	2.637	3.653	
2-propanol								[152]
Concentration (w/w)	0%	10%	16%	20%	40%	60%	100%	
Refractive Index	1.333	1.342	1.348	1.351	1.364	1.372	1.378	
Viscosity [mPa·s]	1.002	2.472	2.813	3.040	2.894	2.441	2.070	
$CaCl_2$								
Concentration (w/w)	0%	2.5%	5%	7.5%	10%	12.5%	15%	17.5%
Refractive Index	1.333	1.339	1.345	1.351	1.358	1.364	1.370	1.377
Viscosity [mPa·s]	1.002	1.064	1.143	1.225	1.319	1.433	1.567	1.729

Table 6.1: Values of the refractive index at a 632.8nm wavelength and kinematic viscosity at $T = 25°C$ for different concentrations of aqueous glycerol, 2-propanol and calcium chloride solutions.

Every time a fluid fills the microfluidic channel and its advancing meniscus reaches the waveguide, the light output signal measured by the photodiode increases abruptly and gets a higher stationary value. After the fluid tranche has passed, the optical transmittivity fell down steeply indicating that the channel is again filled by air.

After several measurements the step height was observed not to be higly reproducible and a clear trend of the output signal as a function of the refractive index of the injected solution was not obtained. The sample was thus investigated by optical microscopy and it was verified that the problem lay behind the wettability of the channels and the employment of air as a separator between the subsequent fluid segments. Fig.6.3a shows the passage of a 40%(w/w) glycerol solution in water after a 20%(w/w) glycerol aqueous solution was fluxed, while fig.6.3b is the micrograph of the channel after the 40% solution has passed and the air fills the channel. The high refractive index contrast between the two solutions makes easily note that the more diluted one left some droplets on the surfaces of the channels which the second solution is not able to remove completely; moreover the last solution leaves again droplets which can contain both the solution itself or a mixture of

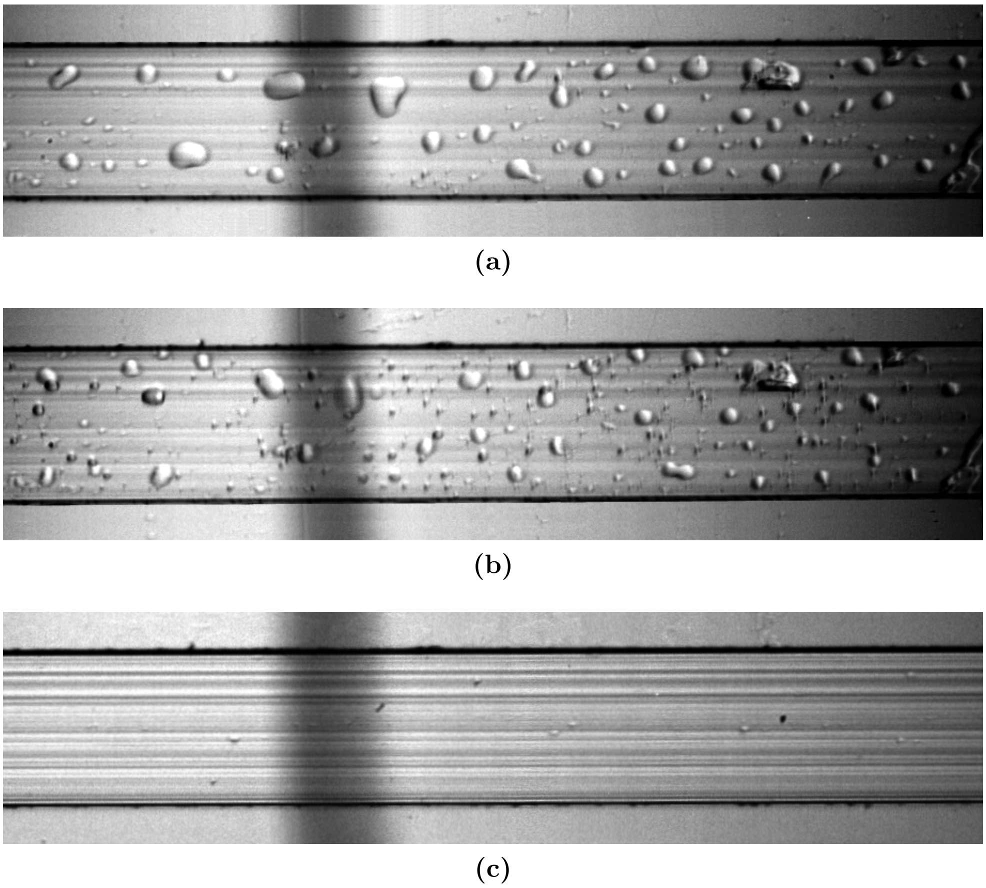

Figure 6.3: Micrographs of microdroplets pinned at the surfaces of the microfluidic channels: (a) pinned droplets of a 20% glycerol aqueous solution while a 40% glycerol aqueous solution is flowing; (b) pinned droplets of a 20% glycerol aqueous solution and a 40% glycerol aqueous solution while air is flowing; (c) pinned droplets of a 10% 2-propanol aqueous solution while a 40% 2-propanol aqueous solution is flowing.

the solutions flowing in the channel earlier.

This undesired effect modifies the concentration of the solutions flowing inside the channel and also can totally compromise the measurements since microdroplets can be found randomly distributed in front of the waveguides changing the response of the beam both when a solution is filling the channel and when air is flowing. Due to laminar flow inside the microfluidic channels, the fluid velocity field tends to zero together with the distance from the channel walls that means the fluid on the very proximity of the walls is moving extremely slow. The only force that avoids fluid separation at the walls is its surface tension. If the channel surfaces are not sufficiently hydrophobic or its wettability is increased by its roughness or by some defects, the fluid can pin and small droplets can be detached. A considerable improvement was obtained by employing 2-propanol instead of glycerol solutions, but small residuals droplets were still present when a second solution was injected (see fig.6.3c). Anyway this tests reveals a poor versatility of the device since its operation depends on the fluid.

The problem could be reduced either by a better tailoring of the channel wetting properties, or by reducing as much as possible the flow rate of the solutions, or by improving the quality of the channel walls, but it cannot be completely eliminated: nature itself was not able to do this since even on a lotus leaf some micro-droplets could stay after a rainy day. The solution is the employment of non-wetting droplets dispersed in a wetting continuous phase as will be discussed in what follows.

6.4 Droplet Detection and Triggering

After proving that the employment of a single channel did not give a reproducible response the single-channel test sample was replaced by the microfluidic droplet generator CJ2 (see table 4.1), characterized by a cross-junction channels geometry and sealed with the sealing type 3 (see section 4.4.4). Syringe pumps were employed to inject in the device mineral oil with SPAN®80 at a concentration of 0.08%(w/w) as the continuous phase and water as the dispersed phase. One of the lateral inlets was sealed in order to exploit the cross-junction as a T-junction. The signal from the TE single-mode of a z-propagating waveguide was registered during the passage of the generated droplets.

As shown in the example in fig.6.4a, when a train of droplets is generated, the voltage signal recorded by the oscilloscope has the shape of a square wave where the higher plateaus refer to the flow of the continuous phase while each lower plateau indicates the passage of a water droplet. Both the rise and the fall of the square wave is characterized by a sharp peak in proximity of the higher plateau. These peaks correspond to the passage of the advancing and the receding menisci and stand for a better confinement of the light due probably to total internal reflection on the oil/water interface at the top of the droplet or to a focusing effect of the very first and very last borders of the droplet. The signal rise and fall are extremely steep and reproducible as can be seen in fig.6.4b(c) where few signals from different droplets are superposed.

As an estimation of the precision on the determination of the time instant at which the meniscus reaches the waveguide, it was measured the time interval δt between the instants at which the signal reaches the 16% and the 84% respectively of the difference between

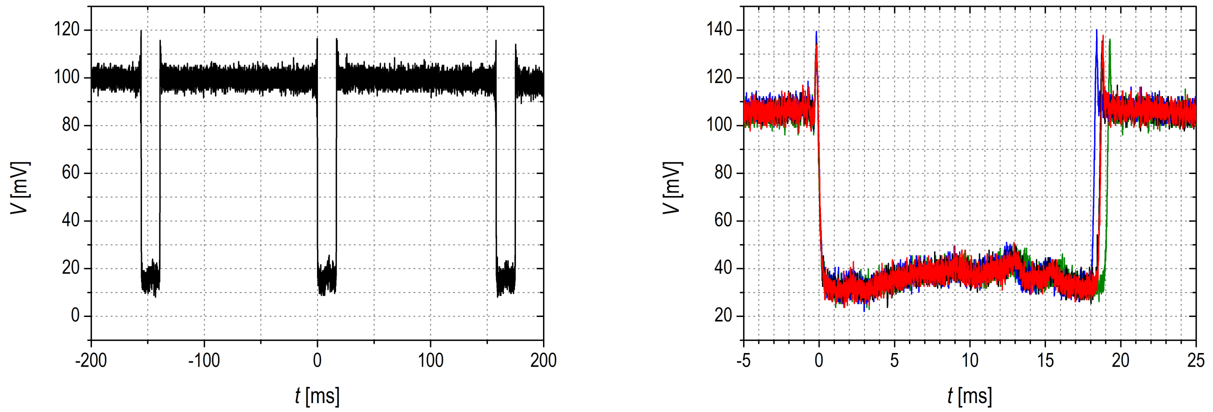

(a) **(b)**

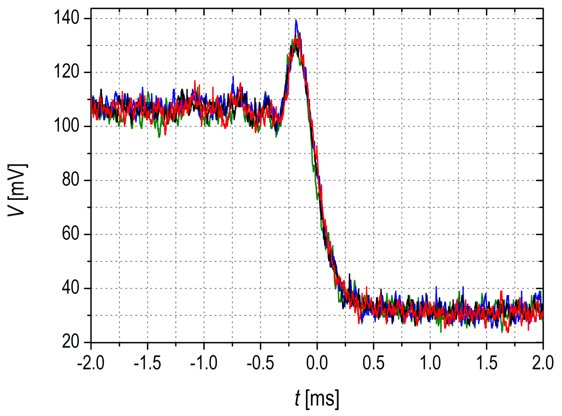

(c)

Figure 6.4: Example of voltage signal from the photodiode at the passage of water droplets in mineral oil through the CJ2 device in a T-junction configuration. (a) Three subsequent droplets; (b) superposition of the signal from four different single droplets as triggered by the oscilloscope, on the negative slope corresponding to the passage of the advancing meniscus; as can be seen the signal of different droplets has the same shape apart from slight differences in the length of the droplets (black and red lines against the green line or the blue one); (c) insight of the previous image showing the high repeatability of the signal shape at the passage of the meniscus.

the average values of the lower and the higher plateaus. Clearly this estimation depends on the speed and the shape of the droplets, and then on the flow rates employed. In the range of flow rates employed during this work δt was found to vary from $377 \pm 4\mu$s at flow rates $Q_c = 10\mu$l/min, $Q_d = 1\mu$l/min, down to $50 \pm 1\mu$s at flow rates $Q_c = 40\mu$l/min, $Q_d = 60\mu$l/min, which are values extremely low.

It is straightforward that an immediate useful application of this optofluidic system is the fast triggering of the droplets during their flow. In microfluidics research and applications the standard way to measure droplets frequency and length is employing the experimental setup described in section 5.1 which requires a microscope, a fast camera, a data storage media to record the images sequences, a software for the analysis of the images, a computer to run the software and time to post-process the sequences and gain the droplet passage

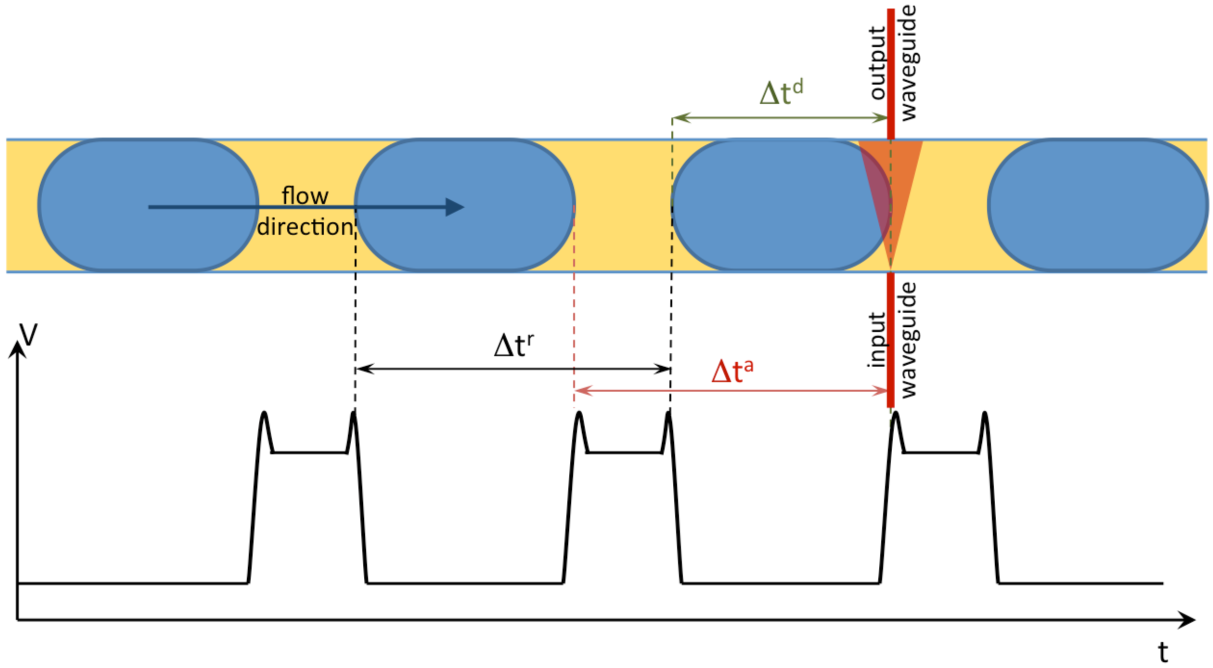

Figure 6.5: Scheme showing the time intervals measured with the integrated system during the passage of droplets.

time. The process could be fastened but, when droplet frequencies of the order of 1kHz or more are reached, a real time image processing is no more feasible.

The great advantage of this configuration relies on the perspective to need just a low power laser (a diode laser with a power less than 1mW is enough since for these measurements a beam with an intensity lower than 400μW was coupled to the waveguide), two fibers connected to the microfluidic device (one exciting the waveguide and the other collecting the signal) and a photodiode with simple electronics triggering a square wave makes realizing the great advantages of such a system.

In order to compare the two different systems the signal from about 100 droplets at different imposed flow rates of the continuous and the dispersed phase were recorded. A software was developed to analyze the output voltage from the oscilloscope in order to obtain the average voltage value of each plateau (excluding the peaks relative to the menisci) and the time instant at which each rise and fall reached their half height.

The passage time instant of all the advancing menisci were recorded and the difference Δt^a between those obtained from two subsequent droplets was calculated (see fig.6.5). From the distribution of all the Δt^a's the average Δt^a_{av} and the dispersion σ^a_t were calculated. The same analysis was performed employing the passage time of the receding menisci Δt^r.

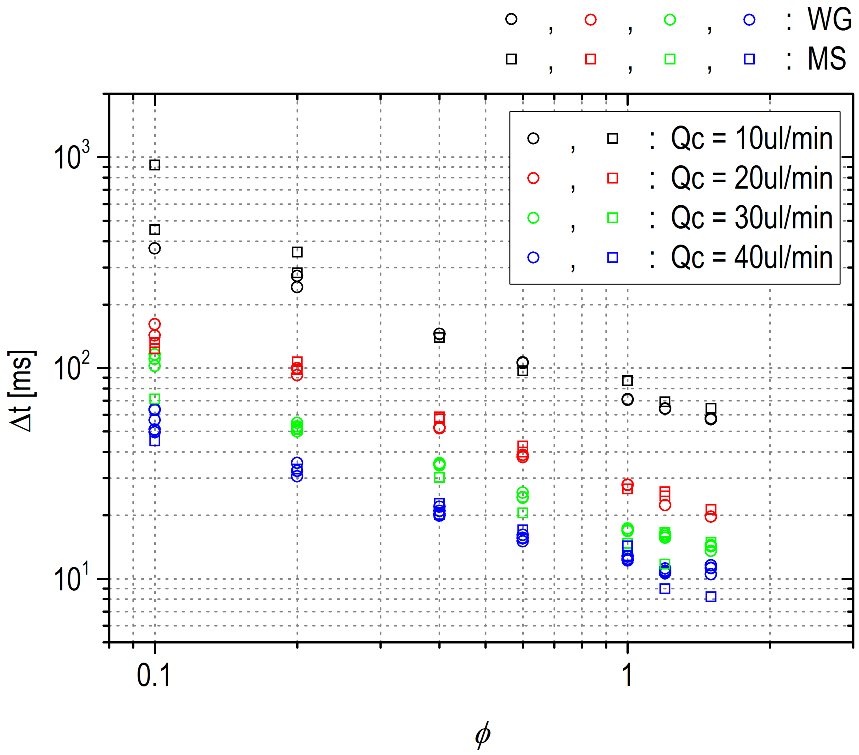

Figure 6.6: Comparison between the time interval between droplets measured with the experimental system (MS) of section 5.1 and the integrated optical trigger (WG) employing the optical waveguides described in this section. Logarithmic scales were set for a better visualization and for the same reason error bars are not drawn. Repeated measurements are reported when available.

In addition the distribution of the difference between the passage times of the advancing and receding menisci was studied to calculate the average time of passage of a single droplet Δt^d_{av}.

The signal from a series of at least 100 droplets was recorded for imposed flow rates of Q_c = 10, 20, 30, 40μl/min for the continuous phase and Q_d =$\{$0.1, 0.2, 0.4, 0.6, 1, 1.2, 1.5$\}\times Q_c$ for the dispersed phase.

The relative difference $(\Delta t^a_{av} - \Delta t^r_{av})/\Delta t^a_{av}$ between the average time interval Δt^a_{av} obtained by the advancing menisci, and that one calculated from the receding menisci Δt^r_{av} never exceeded 0.2% and no systematic trends were noticed. Therefore there is no distinctions in considering Δt^a_{av} or Δt^r_{av}. Also their dispersion was compatible within 10%.

The comparison between the Δt^a_{av} obtained by the integrated optical trigger and the time intervals Δt^m_{av} obtained with the microscope in the same conditions are shown in fig.6.6 (the logarithmic scale is needed just for a better visualization of data at the different continuous phase flow rates).

Logistical reasons prevented us to record simultaneous measurements with the microscope and the optical system so that fluctuations due to the reproducibility of the measurements performed in different laboratories and days and also the reproducibility of the generation of droplet by the device have to be taken into account. Nevertheless data from microscope image analysis and from the optical trigger are in a good agreement.

What makes the integrated optical trigger better than the standard system is the data dispersion. The dispersions of measured Δt on a population of about 100 droplets were calculated both from the data obtained with the microscope and from those gained by the optical trigger. The comparison between the two measurement systems for each imposed

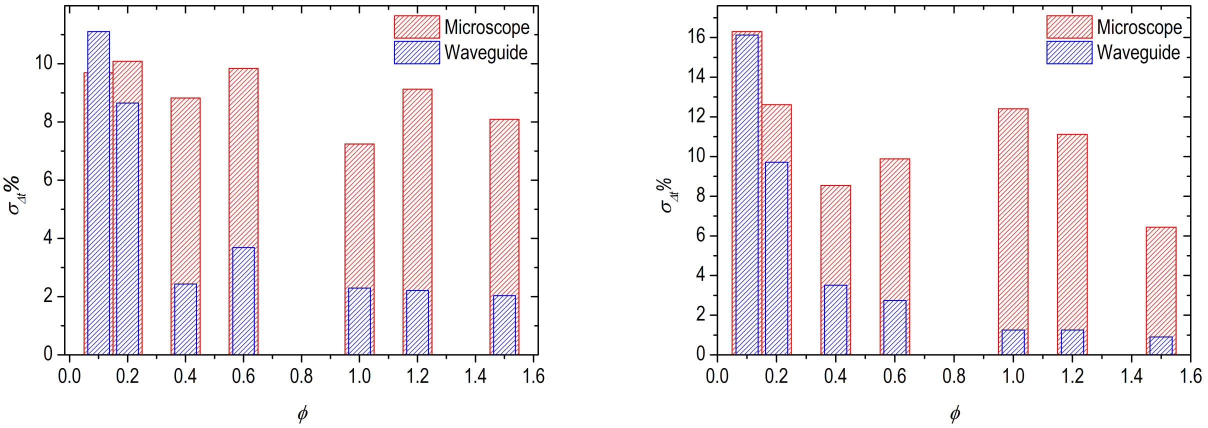

(a) $Q_c = 10\mu$l/min **(b)** $Q_c = 20\mu$l/min

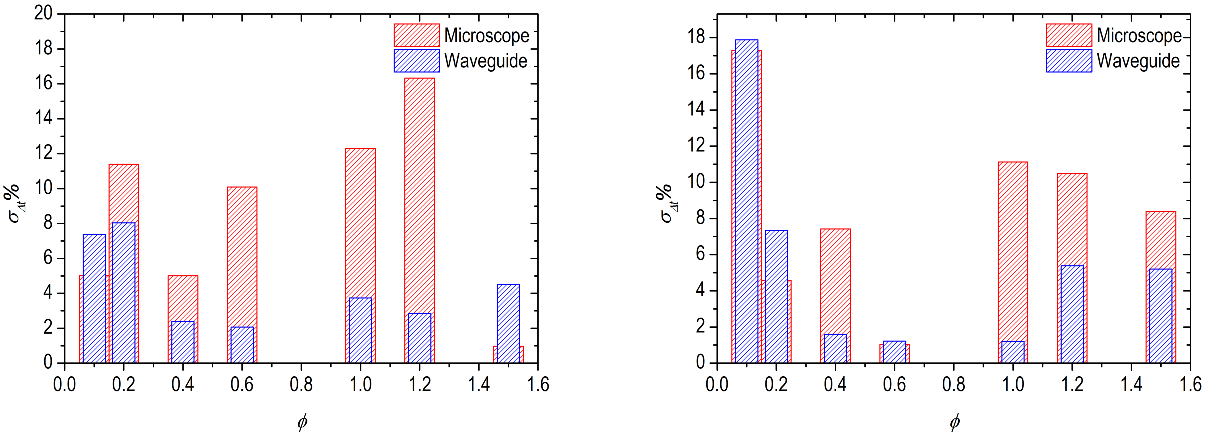

(c) $Q_c = 30\mu$l/min **(d)** $Q_c = 40\mu$l/min

Figure 6.7: Comparison between the dispersion of the distribution of the Δt between subsequent droplets obtained with the experimental setup described in section 5.1 (red larger columns) and the integrated optofluidic system described here (blue thinner columns) for each tested value of the flow rate ratio ϕ and the continuous phase flow rate Q_c.

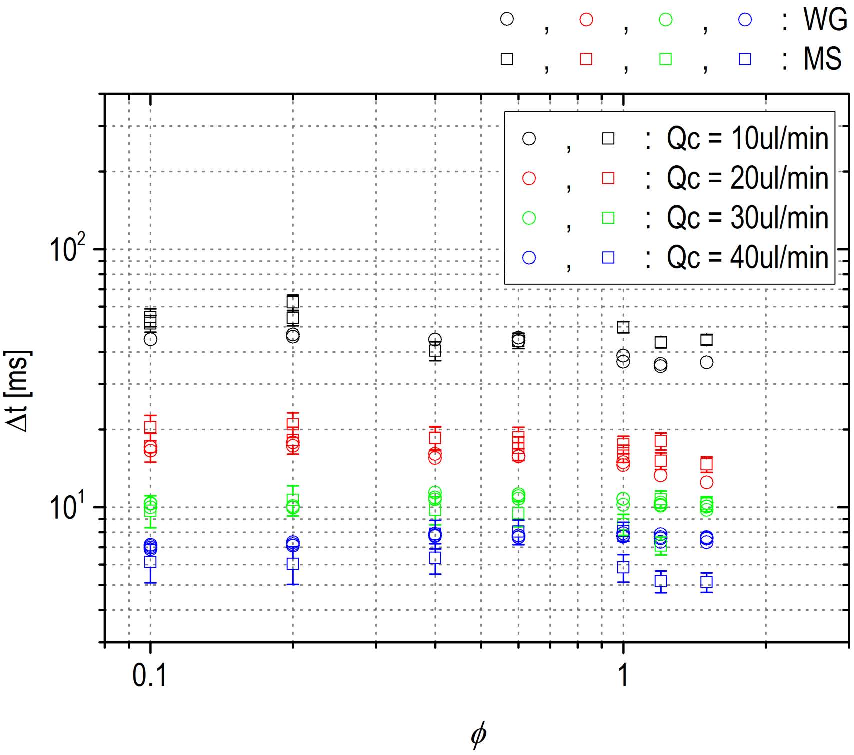

Figure 6.8: Comparison between the time of passage of a droplet measured with the experimental system (MS) of section 5.1 and the integrated optical trigger (WG) employing the optical waveguides described in this section. Error bars for the points referring to the integrated system are always smaller than the markers.

value of Q_c at each dispersed flow rate Q_d is reported in fig.6.7; where more than one measurement was available, the higher value of the dispersion was plotted. As it can be noted, apart from few points at the lowest flow rates, the optical trigger gives a quite lower dispersion in the determination of Δt. This means that part of the fluctuations detected with the microscope are due to the experimental setup rather than to the droplet generator itself.

In addition the passage time Δt^d of a single droplet measured as the difference between the passage of the advancing and the receding meniscus was compared with that obtained with the microscope system. Since the cross-junction was sealed with the sealing type 3 (see section 4.4.4), the waveguide is located at an estimated distance of $(6 \pm 2)\mu$m from the glass top wall of the channel. Then the waveguide measures the time interval Δt^d_{av} needed for the passage of the droplet horizontal section at $\Delta h = 6\mu$m from the top surface while the length registered by the camera connected to the microscope refers to the middle plane section, which includes the entire thickness of the menisci. In order to calculate the difference $\Delta L/2$ between the entire meniscus width and its portion triggered by the waveguide, the same approximation for the three-dimensional shape of the droplet discussed in section 3.3.1 was adopted supposing that the curvature radius of the droplet on the plane perpendicular to the cross-junction plane is $h/2$, with h the height of the channels. It was therefore estimated that the length triggered by the waveguide was:

$$L - \Delta L = L - \left(h - \sqrt{h\Delta h + \Delta h^2}\right) \tag{6.1}$$

The passage time of this partial length can be calculated from the length L_{av} and the velocity v_{av} obtained from the same analysis of the microscope images reported in chapter 5. By this approach it was deduced the following equation:

$$\Delta t^{d}_{\mathrm{ms},av} = \frac{1}{v_{av}}\left[L_{av} - \left(h - \sqrt{h\Delta h + \Delta h^2}\right)\right] \tag{6.2}$$

The comparison between the passage time obtained with the integrated system and that obtained from the microscope data are reported in fig.6.8 for all the different values of the continuous and the dispersed flow rates; the error bars relative to the average Δt_{wg} from the waveguide are always smaller than the markers while those for the microscope are considerably larger due to the propagation from equation (6.2).

The measurements from the two experimental systems show good compatibility and moreover the data from the waveguide seem to suffer lower fluctuations as can be seen looking at those flow rates with repeated measurements available for both systems.

6.5 Refractive index Sensing

The first test on the response of the cross-junction to the refractive index of the dispersed phase was performed generating droplets in the T-junction configuration. Instead of 2-propanol and glycerol, aqueous solutions of $CaCl_2$ were used in order to avoid substances soluble in oil and to span a quite large range of refractive index values without increasing too much the solution viscosity. The physical properties of this solutions are listed in table 6.1. The signal from about 100 droplets was recorded for each different solution.

After rescaling the voltage signal over the reference beam, the ratio $R_V = V_d/V_c$ of the measured voltage from the droplet and the voltage from the continuous phase segment

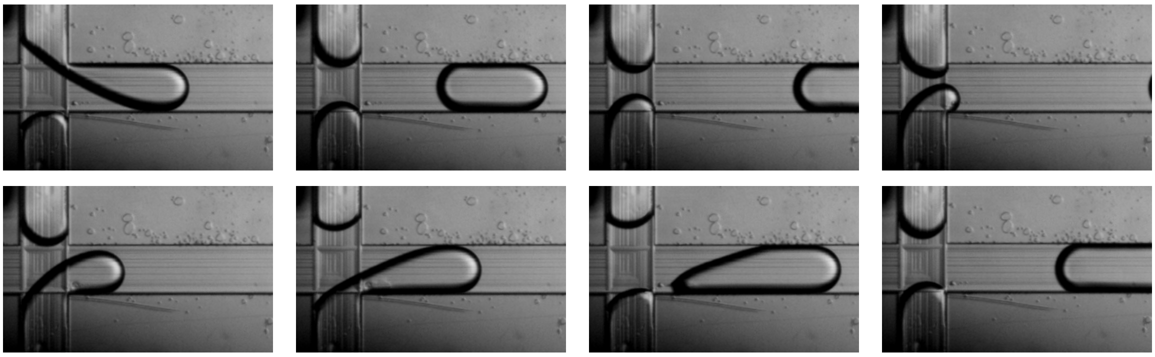

Figure 6.9: Alternating production of droplets of two different solutions from opposite microfluidic channels in the cross-junction device. The flow rates were set to $Q_c = 10\mu\mathrm{l/min}$ for the continuous phase, $Q_d^{(w)} = 3\mu\mathrm{l/min}$ for the MilliQ® water coming from the lower channel and $Q_d^{(s)} = 2\mu\mathrm{l/min}$ for a 5% $CaCl_2$ aqueous solution coming from the upper channel. The micrographs are taken every 20ms, starting from the upper image on the left, down to the lower image on the right.

preceding the droplet was investigated. The repeatability of R_V on a series of about 100 droplets was good, with a maximum standard deviation of $\sigma_{R_V}^{\max} = 5\%$.
Nevertheless it was not found any defined trend of R_V with the refractive index of the solution probably due to the poor reproducibility of the measurements. In fact any time a different solution had to be employed, the syringe had to be unconnected from the tubings and replaced by that one with the new solution. Then a long time was needed to flow the new solution along the tubings up to the reservoir inside the chip and some further minutes to wait for the complete rinsing from the previous solution. During this long time, environmental conditions such as temperature could change significantly, leading to a different response from the system. In addition also a misalignment of the waveguide could happen due to vibrations occurring during this operations.
The main problem was the lack of a reference signal to which the measurement of each single droplet could be compared. In fact the comparison between the signal from droplets of different concentration was made on measurements performed at several minutes one from the other, therefore a reference signal to account for the changes on the external conditions was needed.

The solution to this issue was the exploitation of the cross-junction device to flow simultaneously both the droplets to be measured and pure water droplets as a reference.
A solution with a certain concentration of $CaCl_2$ was injected from one of the two microfluidic channels perpendicular to the main channel, while pure Milli-Q® water was flown through the other opposite channel. The result was that droplets of water and droplets con-

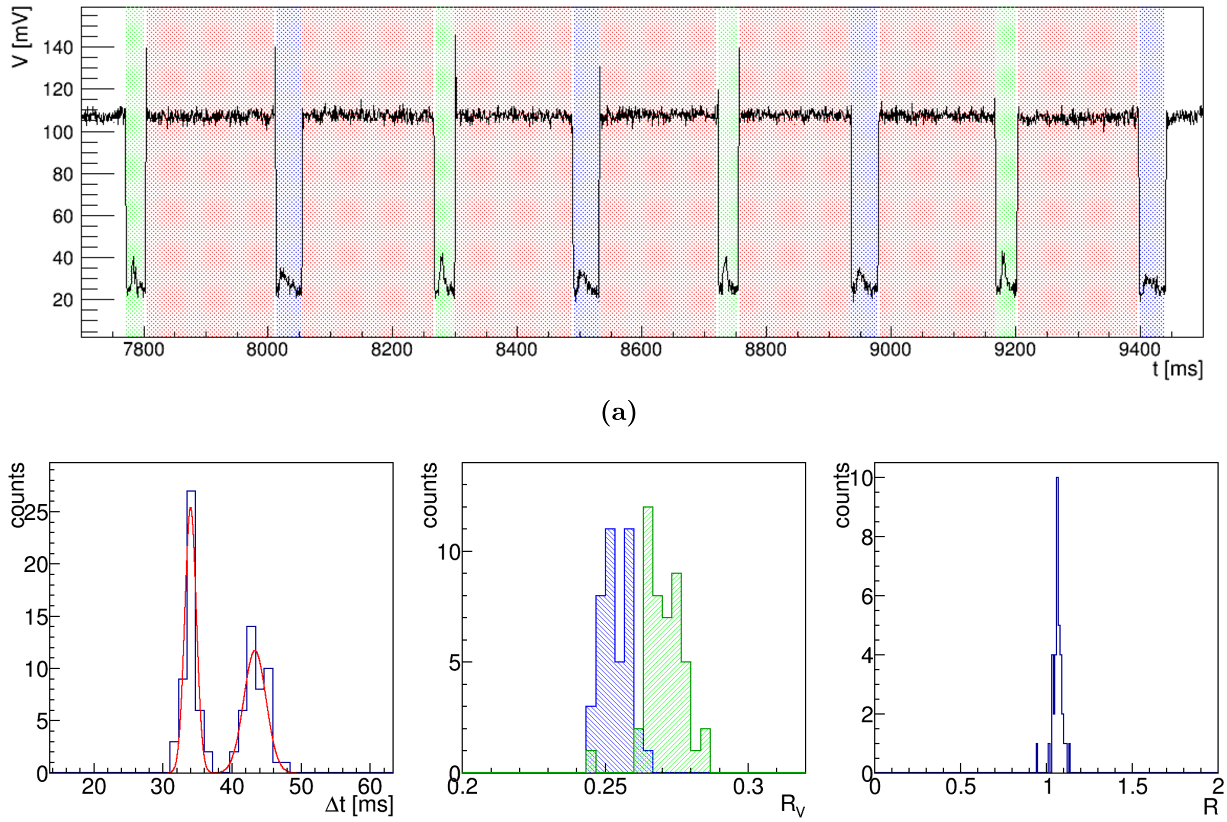

(a)

(b) (c) (d)

Figure 6.10: Main steps of software calculations for the sensing of the refractive index of a solution in the opto-microfludic device with a cross-junction configuration: (a) droplets distinction between the reference solution in blue (MilliQ® water) and the solution to be measured in green (5% $CaCl_{2(aq)}$); (b) distribution of the passage time of droplets; (c) $R_V = V_d/V_c$ distribution, colors indicate the reference solution (w) in blue and the solution (s) to be measured in green; (d) $R = R_V^s/R_V^w$ distribution.

taining the solution alternatively were injected from opposite sides into the main channel and then measured by the integrated optical system (see fig.6.9). Imposing the same flux of the two dispersed phases coming from the two transverse branches of the cross-junction there was no need for any further control on the device to obtain stable alternating droplets. The process is self-controlled: a droplet detaches from one of the dispersed phases tips and the tip recoils lowering the pressure at the cross; the other tip is then pulled inside the main channel and the continuous phase led it to breakup and recoil, and the process starts again. The two dispersed phases were observed never to merge into each other.

In addition the length of the droplets together with the number of droplets coming from a channel or the other can be tailored changing the injecting flow rates. The possibility to impose a different length for droplets coming from a different dispersed phase is useful to distinguish water droplets from $CaCl_{2(aq)}$ droplets since they can be sorted by measuring their passage time.

The analysis software was consequently modified to recognize droplets of different lengths by measuring and comparing their time of passage. An example of the output sketch from the software showing the droplet identification is reported in fig.6.10a. Blue areas stand for the reference water droplets while green areas indicate the droplets of saline solution whose refractive index has to be measured (in the example a 5% $CaCl_2$ aqueous solution was flowing); in red is the signal from the mineral oil with SPAN®80 used as continuous phase. As can be seen in fig.6.10b the passage time of the longer reference droplets and that of the shorter solution droplets have two well separated distributions so that Δt can be easily exploited to recognize the two fluids.

As discussed before the software calculated for all droplets, tha ratio $R_V = V_d/V_c$, which is the dispersed phase voltage rescaled over the voltage of the continuous phase segment preceding each droplet. The distribution of R_V is reported in fig.6.10c and colors show how the data was associated to the two different liquids.

In addition, in this double droplet configuration, every time the software recognized the passage of a water droplet (w) followed by a droplet of solution (s), it also recorded the ratio R between the values R_V^s and R_V^w: $R = R_V^s/R_V^w$ was thus defined as the actual response of the device to the refractive index of the solution. The ratio R distribution for the reported example is plotted in fig.6.10d.

Measurements from more than 6 series of about $40 \div 50$ couples of droplets were recorded for each concentration of the $CaCl_2$ aqueous solution. For each droplet series the repeatability of $R = R_V^s/R_V^w$ was verified to be as good as in the T-junction configuration, and in particular a standard deviation σ_R lower than 4% was verified.

The great improvement is on the reproducibility because this configuration showed a clear monotonic trend with the refractive index of the tested solutions was obtained, irrespective of the fact that measurements were even performed on different days. For each value of concentration a set of at least 6 independent non subsequent measurements of R were performed repeating all the tubings and syringe connection procedure and the setting of the flow rates. For each set the standard deviation $\sigma_R(C\%)$ was calculated and the maximum was found to be $\sigma_R^{\max}(C\%) = 0.01$.

The average value $R_{\mathrm{av}}(C\%)$ and its random error $\sigma_{R_{\mathrm{av}}}$ were calculated for each concentration and they are plotted as a function of both the refractive index and the concentration

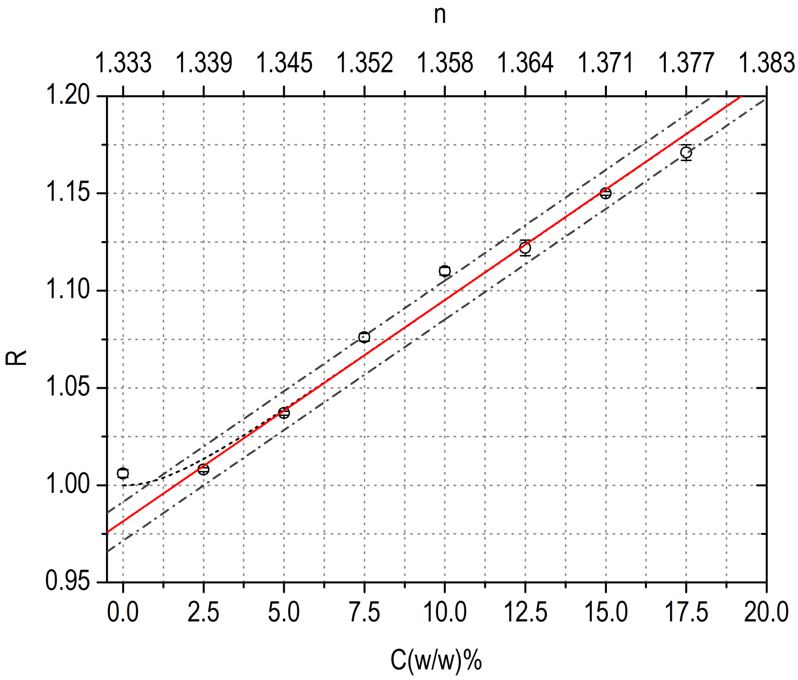

Figure 6.11: Plot of R as a function of both the concentration and the refractive index, measured from different solutions of $CaCl_2$ in MilliQ® water. The black dashed line is just a guide for the eye while the red line represents the weighted linear fit of data in the linearity region from a concentration of 2.5% up to 17.5%. Each experimental point was obtained as the average among at least 6 independent measurements. The standard deviation of each of these sets of measurements was calculated and the greatest was found to be $\sigma_{\max} = 0.01$. The dash-dot gray lines are set at a distance $\sigma_{\max}$ from the linear fit.

of the employed solution in fig.6.11.

As it can be seen the device presents two different regimes, a first one for n below 1.339, corresponding to a concentration of $CaCl_2$ lower than 2.5%, where the sensitivity $\frac{\Delta R}{\Delta n}$ is below $2 \cdot 10^{-3}$ and a second regime at $n > 1.339$ with a higher sensitivity where a monotonic trend can be identified. The number of points is not enough to infer the real detailed dependence of the device response on the refractive index of the droplets, but some considerations about its performances can be deduced by the overall trend.

The monotonicity region between $C = 2.5\%$ and $C = 17.5\%$ is well described by the weighted linear fit represented in the plot by a red line. As indicated by the gray dotted lines all points stay at a distance from the fit comparable with $\sigma_R^{\max}(C\%)$.

The sensitivity S of the device can be deduced by the slope of the interpolating line: $S_C = \frac{\partial R}{\partial C} = (1.14 \pm 0.04) \cdot 10^{-2}$ or $S_n = \frac{\partial R}{\partial n} = 4.56 \pm 0.16$. The minimum refractive index difference $\Delta n_{\min}$ between two substances to be clearly discerned by the sensor employing the described protocol can be estimated as $\Delta n_{\min} = \sigma_R^{\max}(n)/S_n = 2 \cdot 10^{-3}$ or respect to the concentration $\Delta C\%_{\min} = \sigma_R^{\max}(C\%)/S_C = 0.88\%$.

6.6 Summary and Future Perspectives

In this chapter the possibility to couple titanium in-diffused waveguides to a microfluidic channel engraved in lithium niobate was proved. The high repeatability of the system employed as a droplet trigger and counter was demonstrated and the comparison with a standard set-up used in microfuidics research showed that the integrated system gave even better performances and can reach a faster response.

Moreover, even in this prototypical form, the integrated system allows for real-time measurements also at very high frequencies since it is limited just by the electronics speed, getting rid of the need for huge data storages and elaborated software analyses. This is a great advantage both in microfluidics research and applications: a microscope has been shrinked in a waveguide, a fast-camera into a photodiode and simple electronics, a several gigabytes hard disk into a text file of few tens of kilobytes, several thousands of pixels into a single electric voltage.

Few straightforward steps reachable by standard techniques are needed to make the chip fully portable and releasing it by the near-field setup employed for the characterization: the adding of quick-lock inlets and outlets for the fluids, and the gluing of optical fibers to the ends of the integrated waveguides to inject and collect the light signal. The final aim should be the complete integration of the light source and the detection electronics.

Some additional improvements are going to be realized by our research group in the next months; among them it can be cited the employment of a splitting and recombining waveguide for the measurement of the droplet length and velocity by employing its double triggering with a single light input and output.

On the other hand the prototype was also characterized as a refractive index sensor. Its present detection sensitivity of $2 \cdot 10^{-3}$ above $n = 1.337$ is greater than other examples reported in literature wheer the refractive index of flowing droplets is measured [3, 153]. The presented measurements required just 50 droplets, that means that about 20s were enough at the employed flow rates of few μl/min. Since the device is able to sustain flow rates two order of magnitude higher and that more than 500 solution/reference couples of droplets per second can be injected at those fluxes, the time for a single measure can

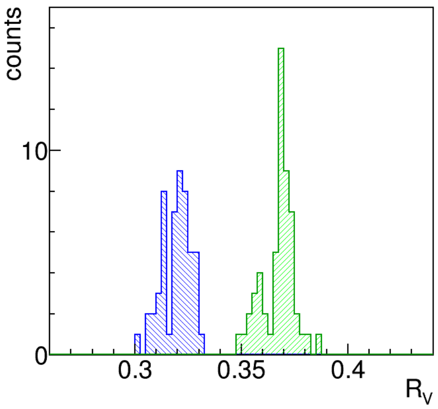

Figure 6.12: Voltage ratio R_V for alternating water (in blue) and 15% $CaCl_{2(aq)}$ droplets. The distribution have both a standard deviation $\sigma = 7 \cdot 10^{-3}$ and an average value respectively of 0.319 ± 0.001 and 0.368 ± 0.001 that means they are separated by a distance equal to 7σ.

be reduced down to the order of 0.1s. Moreover it has to be considered that although no control on the temperature of the system was added, the immediate comparison between the reference and the solution to be identified made the measurement reproducible anyway at normal ambient conditions.

The employment of droplets makes no recovery or cleaning operations needed for the chip after a measurement since the flowing of the fluid to be detected does not modify anyway the device response. The implementation of multiple inlets controlled by valves, injecting alternatively different samples to be identified, could then lead to a very high and fast parallelization of this measurement system.

In any case the presented lab-on-a-chip is surely able to distinguish with a 100% probability a single water droplet for example by a single 15% $CaCl_{2(aq)}$ droplet as shown by the example in fig.6.12 where the voltage ratio R_V is reported for alternated water and 15% $CaCl_{2(aq)}$ droplets. The two average values of the distributions, respectively 0.319 ± 0.001 and 0.368 ± 0.001 are at a distance of 7 times their standard deviation $\sigma = 7 \cdot 10^{-3}$, then no false positives are possible. This means that a single droplet of solution can be used as a digital reference for example to indicate the beginning or the end of droplet sequences to be sorted and processed in a different way, with possible applications in digital microfluidics and pharmaceutical applications.

Conclusions

The thesis presented here showed the realization of a Lab-on-a-Chip in lithium niobate where both a microfluidic stage for water-in-oil droplet generation and an optical stage for droplet detection was integrated with success.
To the author knowledge this is the first time lithium niobate is used to perform the detection of droplets flowing through microfluidic channels directly engraved on it.
During this work titanium in-diffused waveguides to illuminate droplets and collect the transmitted light were coupled effectively to microfluidic channels engraved with a dicing saw and sealed with a silica covering. During the realization of the prototype, on one hand several technological issues had to be faced and new solutions had to be conceived, on the other hand experimental investigations on the fabrication processes and the physics underlaying the chip operation were carried out.

The realization of the optical stage moved from basic knowledges of our research group and required the optimization of titanium in-diffused waveguides for the confinement of light at 632.8nm. In particular the diffusion process was characterized by RBS and SIMS measurements and single TE and TM modes waveguides were fabricated by joint photolitography, sputtering and thermal annealing. A dedicated near field setup to characterize the waveguides was built and the comparison between the obtained guided modes and the prediction from a finite element method based software was shown.

The design, the fabrication and the characterization of the microfluidic stage required some additional efforts since this research field was new to our group.
A first preliminary study was performed on lithium niobate wettability properties and a functionalization method to increase its hydrophobicity was defined. This process allowed to raise the water-$LiNbO_3$ contact angle from $62 \pm 1^\circ$ up to $101 \pm 1^\circ$ and this improvement was found to be mandatory for a stable droplet generation in the present microfluidic device.
Different techniques were employed to engrave microfluidic channels in lithium niobate:

laser ablation by femtosecond pulses at 800nm was widely investigated by optical microscopy and Atomic Force Microscopy (AFM) and the best parameters to get the lower roughness were derived; mechanical micromachining from two different types of dicing saw was also tested and analyzed.
Advantages and drawbacks on the application of both methods to microfluidics were outlined and discussed.

Specific methods for sealing the microfluidics channels engraved on the surface of the crystal, without masking the waveguides placed at the very top of the side walls had to be conceived. A traditional technique employing PDMS as described in literature was tested, but finally it was replaced by a more stiff, durable and versatile glass sealing. The final design of the chip was quite cheap, resistant to pressure higher than few atmospheres and, opposite to most diffused polymer based devices it does not suffer degradation even if organic solvents or acids are flown inside the channels.

The generation of water-in-oil droplets with the laser ablated T-junction was investigated both to define the performances of the chip and to study the theoretical scaling laws describing the break-up of the dispersed phase tip typical of cross-flow geometries.
An optical microscopy system was employed to record images of produced droplet at high frequencies (more than 1kHz) and an image analysis software developed by the LaFSI group of Padova allows for the analysis of the image sequences.
Within this PhD work a dedicated software was developed to perform a detailed statistical analysis of the droplet production frequency and length. The results showed a very stable production frequency (within 10%) and length (within 3%) of the droplets, perfectly comparable with most recent microfluidic devices reported in literature.
A comparison between the experimental data and the theoretical models proposed in the past to describe the droplet breakup in the squeezing regime was carried out. Discrepancies not mentioned before by other authors, were observed at the lowest values of the capillary number ($Ca < 3 \cdot 10^{-3}$). An empirical law was proposed on the basis of the experimental observations which accounts both for theoretical results reported in literature and for measurements described in this thesis.

The last part of this work dealt with the coupling of the waveguides to the microfluidic channels and the final realization of a completely integrated Lab-on-a-Chip able to generate and detect droplets.
Laser ablated channels were shown to be suitable for the coupling to a waveguide for the

illumination of the droplets as it is already reported in literature for ablated channels in silica. Nevertheless the roughness of the channels side walls revealed to be too high for the light to be collected from the output waveguide and further improvements are required to join the optical detection stage with the high versatility of the channels obtained by laser ablation.

On the contrary, the microfluidic channels obtained with the dicing saw were proved to be suitable for the coupling of both the injecting and collecting waveguides.

Although the collected intensity transmitted during the passage of a single fluid was demonstrated to be sensitive to the refractive index of a single fluid flowing in the channels, the measurements showed to suffer poor reproducibility due to wettability issues concerned with this configuration.

The near field setup was then implemented to perform time resolved measurements and allow for the detection of the transmitted intensity while droplets were flowing.

A dedicated software was developed to analyze the signal modulated by the passage of the droplets.

The prototype was employed to measure the time of passage and the temporal length of the droplets while they overcame the waveguide and the results were compared with those from the optical microscopy system. The response of the two systems were observed to be in a very good agreement and the dispersion of the data from the integrated system were demonstrated to be always lower than those obtained from the standard setup, specially at the highest production frequencies.

The Lab-on-a-Chip was employed also as a refractive index sensor for aqueous solutions. A cross-junction double droplet configuration employing three fluid phases (oil, pure water, aqueous solution) was conceived: both water droplets and droplets from an aqueous solution were alternatively injected into the microfluidic chip. This method allowed to get, within few tens of milliseconds, a signal relative to the intensity transmitted by the droplet of the solution and a reference signal from pure water.

The sensor was proved to have a linear response in the range $n = [1.339, 1.377]$ with a sensitivity of $\Delta n = 2 \cdot 10^{-3}$.

The first clear advantage of such a chip used for droplet counting is the complete integration of the optical stage and its very low response time compared to the experimental setups usually employed. Standard setups require a microscope, a fast camera, a several gigabytes hard disk, an image analysis software. In the integrated chip the microscope optics is shrinked in a waveguide and the output signal is just a single voltage, which can be easily processed by electronics. Further possible integrations easily achievable by standard techniques could be the gluing of optical fibers to inject and collect the light, and quick-lock inlets for a fast insertion of the tubings.

Further advantages of this LOC are the high chemical stability with respect to polymer based microfluidic chips and the fact that no operations have to be performed and no time has to be waited between two subsequent measurements since droplet microfluidics avoids contact between the dispersed phase and the walls of the channel, being completely wet by the continuous phase.

Performing refractive index measurements on single droplets in a very short time with an integrated system is very appealing both for microfluidics research and microfluidics applications in the fields of biology, medicine, pharmacology and environmental sciences. Droplets can indeed used either to carry biological samples, or used for drug delivery, or employed as chemical reactors to study phenomena at the microscale.

Finally some words have to be spent to mention the advantages coming from the exploitation of lithium niobate as a substrate for both optics and microfluidics.

In fact lithium niobate has already been employed for moving droplets via surface acoustic waves induced by piezoelectricity. The voltage can be applied through interdigital electrodes deposited on its surface and this technique has been already proved to be able to move droplets or even trap particles or cells in a specific region of the channel during fluid flow.

Moreover the trapping of particles can be performed by exploiting the electric fields produced on the surface of lithium niobate after ligth exposure due to its photorefractivity. The photorefractive effect can also be exploited to modify the refractive index of the material in order to realize Bragg gratings, beam splitters or wavelength filters. This characteristics make possible the planning of more complex optical stages able for example to treat simultaneously more wavelengths or to excite fluorescence inside droplets with a pump wavelength and collect the output signal at a greater wavelength filtering the pump signal with a Bragg reflecting grating.

Therefore the results discussed open new perspective towards the complete integration of multiple stages inside the presented Lab-on-a-Chip thanks to the many properties of lithium niobate.

Bibliography

[1] Christopher GF, Noharuddin NN, Taylor Ja *et al.* (2008) *Experimental observations of the squeezing-to-dripping transition in T-shaped microfluidic junctions*. Physical Review E - Statistical, Nonlinear, and Soft Matter Physics, **vol. 78, no. 3**:pp. 1–12. (Cited on pages xii, xvi, 47, 89, 91, 92, 93, 94, 95, and 98).

[2] van Steijn V, Kleijn CR and Kreutzer MT (2010) *Predictive model for the size of bubbles and droplets created in microfluidic T-junctions.*. Lab on a chip, **vol. 10, no. 19**:pp. 2513–2518. (Cited on pages xii, 49, 50, 89, 93, and 94).

[3] Weber E, Puchberger-Enengl D and Vellekoop MJ, *In-line characterization of micro-droplets based on partial light reflection at the solid-liquid interface*. In *ASME 2012 10th International Conference on Nanochannels, Microchannels, and Minichannels collocated with the ASME 2012 Heat Transfer Summer Conference and the ASME 2012 Fluids Engineering Division Summer Meeting*, (pp. 589–595) (American Society of Mechanical Engineers, 2012). (Cited on pages 1 and 120).

[4] Baylor ME, Cerjan BW, Pfiefer CR *et al.* (2012) *Monolithic integration of optical waveguide and fluidic channel structures in a thiol-ene/methacrylate photopolymer*. Optical Materials Express, **vol. 2, no. 11**:pp. 1548–1555. (Cited on page 1).

[5] Osellame R, Maselli V, Vazquez RM *et al.* (2007) *Integration of optical waveguides and microfluidic channels both fabricated by femtosecond laser irradiation*. Applied physics letters, **vol. 90, no. 23**:p. 231118. (Cited on page 2).

[6] Vazquez RM, Osellame R, Cretich M *et al.* (2009) *Optical sensing in microfluidic lab-on-a-chip by femtosecond-laser-written waveguides*. Analytical and bioanalytical chemistry, **vol. 393, no. 4**:pp. 1209–1216. (Cited on page 2).

[7] Bragheri F, Minzioni P, Vazquez RM *et al.* (2012) *Optofluidic integrated cell sorter fabricated by femtosecond lasers*. Lab on a Chip, **vol. 12, no. 19**:pp. 3779–3784. (Cited on page 2).

[8] Schneider MF, Guttenberg Z, Schneider SW *et al.* (2008) *An acoustically driven microliter flow chamber on a chip (μFCC) for cell–cell and cell–surface interaction studies*. ChemPhysChem, **vol. 9, no. 4**:pp. 641–645. (Cited on page 2).

[9] Friend J and Yeo LY (2011) *Microscale acoustofluidics: Microfluidics driven via acoustics and ultrasonics*. Reviews of Modern Physics, **vol. 83, no. 2**:p. 647. (Cited on page 2).

[10] Eggert H, Kuhnert F, Buse K *et al.* (2007) *Trapping of dielectric particles with light-induced space-charge fields*. Applied physics letters, **vol. 90, no. 24**:p. 241909. (Cited on page 2).

[11] Esseling M, Zaltron A, Argiolas N *et al.* (2013) *Highly reduced iron-doped lithium niobate for optoelectronic tweezers*. Applied Physics B, **vol. 113, no. 2**:pp. 191–197. (Cited on page 2).

[12] Esseling M, Zaltron A, Sada C *et al.* (2013) *Charge sensor and particle trap based on z-cut lithium niobate*. Applied Physics Letters, **vol. 103, no. 6**:p. 061115. (Cited on pages 2 and 40).

[13] Jubera M, García-Cabañes A, Olivares J *et al.* (2014) *Particle trapping and structuring on the surface of LiNbO 3: Fe optical waveguides using photovoltaic fields*. Optics letters, **vol. 39, no. 3**:pp. 649–652. (Cited on page 2).

[14] Rauber A (1978) *Chemistry and physics of lithium niobate*. Current topics in materials science, **vol. 1**:pp. 481–601. (Cited on page 6).

[15] Volk T and Wöhlecke M, *Lithium niobate: defects, photorefraction and ferroelectric switching*, vol. 115 (Springer Science & Business Media, 2008). (Cited on page 5).

[16] Lerner P, Legras C and Dumas J (1968) *Stoechiometrie des monocristaux de metaniobate de lithium*. Journal of Crystal Growth, **vol. 3**:pp. 231–235. (Cited on page 8).

[17] Sohler W, Dibyendu D, Selim R *et al.* (2005) *Erbium-doped lithium niobate waveguide lasers*. IEICE transactions on electronics, **vol. 88, no. 5**:pp. 990–997. (Cited on page 8).

[18] Wöhlecke M, Corradi G and Betzler K (1996) *Optical methods to characterise the composition and homogeneity of lithium niobate single crystals*. Applied physics B, **vol. 63, no. 4**:pp. 323–330. (Cited on page 9).

[19] Luennemann M, Hartwig U, Panotopoulos G *et al.* (2003) *Electrooptic properties of lithium niobate crystals for extremely high external electric fields*. Applied Physics B, **vol. 76, no. 4**:pp. 403–406. (Cited on page 10).

[20] Bernal E, Chen G and Lee T (1966) *Low frequency electro-optic and dielectric constants of lithium niobate*. Physics Letters, **vol. 21, no. 3**:pp. 259–260. (Cited on page 11).

[21] Du XY, Swanwick ME, Fu YQ *et al.* (2009) *Surface acoustic wave induced streaming and pumping in 128° Y-cut LiNbO 3 for microfluidic applications*. Journal of Micromechanics and Microengineering, **vol. 19, no. 3**:p. 35016. (Cited on pages 12, 37, and 39).

[22] Shi J, Mao X, Ahmed D *et al.* (2008) *Focusing microparticles in a microfluidic channel with standing surface acoustic waves (SSAW)*. Lab on a Chip, **vol. 8, no. 2**:pp. 221–223. (Cited on page 12).

[23] Weis R and Gaylord T (1985) *Lithium niobate: summary of physical properties and crystal structure*. Applied Physics A, **vol. 37, no. 4**:pp. 191–203. (Cited on page 12).

[24] Grilli S and Ferraro P (2008) *Dielectrophoretic trapping of suspended particles by selective pyroelectric effect in lithium niobate crystals*. Applied Physics Letters, **vol. 92, no. 23**:p. 232902. (Cited on page 12).

[25] FerraroP, CoppolaS, GrilliS *et al.* (2010) *Dispensing nano-pico droplets and liquid patterning by pyroelectrodynamic shooting*. Nat Nano, **vol. 5, no. 6**:pp. 429–435. (Cited on pages 12 and 39).

[26] Glass A, Von der Linde D and Negran T (1974) *High-voltage bulk photovoltaic effect and the photorefractive process in LiNbO3*. Applied Physics Letters, **vol. 25, no. 4**:pp. 233–235. (Cited on page 13).

[27] Ashkin A, Boyd G, Dziedzic Ji *et al.* (1966) *Optically-induced refractive index inhomogeneities in LiNbO3 and LiTaO3*. Applied Physics Letters, **vol. 9, no. 1**:pp. 72–74. (Cited on page 13).

[28] Vinetskii V and Kukhtarev N (1975) *Anomalous photostress and energy transfer in semiconductor holograph gratings*. Pisma v Zhurnal Tekhnischeskoi Fiziki, **vol. 1**:pp. 176–181. (Cited on page 14).

[29] Sugii K, Fukuma M and Iwasaki H (1978) *A study on titanium diffusion into LiNbO3 waveguides by electron probe analysis and X-ray diffraction methods*. Journal of Materials Science, **vol. 13, no. 3**:pp. 523–533. (Cited on page 17).

[30] Armenise M, Canali C, De Sario M *et al.* (1982) *Evaluation of the Ti diffusion process during fabrication of Ti: LiNbO 3 optical waveguides*. Journal of Non-Crystalline Solids, **vol. 47, no. 2**:pp. 255–257. (Cited on page 17).

[31] Griffiths GJ and Esdaile RJ (1984) *Analysis of titanium diffused planar optical waveguides in lithium niobate*. Quantum Electronics, IEEE Journal of, **vol. 20, no. 2**:pp. 149–159. (Cited on page 17).

[32] Wooten EL, Kissa KM, Yi-Yan A *et al.* (2000) *A review of lithium niobate modulators for fiber-optic communications systems*. Selected Topics in Quantum Electronics, IEEE Journal of, **vol. 6, no. 1**:pp. 69–82. (Cited on page 17).

[33] Runde D, Breuer S and Kip D (2008) *Mode-selective coupler for wavelength multiplexing using LiNbO3: Ti optical waveguides*. Central European Journal of Physics, **vol. 6, no. 3**:pp. 588–592. (Cited on page 17).

[34] Korkishko YN and Fedorov VA, *Ion exchange in single crystals for integrated optics and optoelectronics* (Cambridge Int Science Publishing, 1999). (Cited on page 17).

[35] Korkishko YN, Fedorov VA and Feoktistova OY (2000) *LiNbO3 Optical Waveguide Fabrication by High-Temperature Proton Exchange*. J. Lightwave Technol., **vol. 18, no. 4**:p. 562. (Cited on page 18).

[36] Chen F, Wang XL and Wang KM (2007) *Development of ion-implanted optical waveguides in optical materials: A review*. Optical materials, **vol. 29, no. 11**:pp. 1523–1542. (Cited on page 18).

[37] Peña-Rodríguez O, Olivares J, Carrascosa M *et al.* (2012) *Optical waveguides fabricated by ion implantation/irradiation: A review*. Ion Implantation, Prof. Mark Goorsky (Ed.), ISBN, (pp. 978–953). (Cited on page 18).

[38] Bentini G, Bianconi M, Correra L *et al.* (2004) *Damage effects produced in the near-surface region of x-cut LiNbO3 by low dose, high energy implantation of nitrogen, oxygen, and fluorine ions*. Journal of applied physics, **vol. 96, no. 1**:pp. 242–247. (Cited on page 18).

[39] Yin JJ, Lu F, Ming XB *et al.* (2010) *Theoretical modeling of refractive index in ion implanted LiNbO3 waveguides*. Journal of Applied Physics, **vol. 108, no. 3**:p. 033105. (Cited on page 18).

[40] Itoh K, Matoba O and Ichioka Y (1994) *Fabrication experiment of photorefractive three-dimensional waveguides in lithium niobate*. Optics letters, **vol. 19, no. 9**:pp. 652–654. (Cited on page 18).

[41] Burghoff J, Grebing C, Nolte S *et al.* (2007) *Waveguides in lithium niobate fabricated by focused ultrashort laser pulses*. Applied surface science, **vol. 253, no. 19**:pp. 7899–7902. (Cited on page 19).

[42] Horn W, Kroesen S, Herrmann J *et al.* (2012) *Electro-optical tunable waveguide Bragg gratings in lithium niobate induced by femtosecond laser writing*. Optics express, **vol. 20, no. 24**:pp. 26922–26928. (Cited on page 19).

[43] Courjal N, Guichardaz B, Ulliac G *et al.* (2011) *High aspect ratio lithium niobate ridge waveguides fabricated by optical grade dicing*. Journal of Physics D: Applied Physics, **vol. 44, no. 30**:p. 305101. (Cited on pages 19 and 56).

[44] Hu H, Ricken R, Sohler W *et al.* (2007) *Lithium Niobate Ridge Waveguides Fabricated by Wet Etching*. Photonics Technology Letters, IEEE, **vol. 19, no. 6**:pp. 417–419. (Cited on pages 19, 56, and 62).

[45] Cheng RS, Chen WL and Wang WS (1995) *Mach-Zehnder modulators with lithium niobate ridge waveguides fabricated by proton-exchange wet etch and nickel indiffusion*. Photonics Technology Letters, IEEE, **vol. 7, no. 11**:pp. 1282–1284. (Cited on page 19).

[46] Lee H and Shin SY (1995) *Lithium niobate ridge waveguides fabricated by wet etching*. Electronics Letters, **vol. 31, no. 4**:pp. 268–269. (Cited on page 19).

[47] Rabiei P and Steier WH (2005) *Lithium niobate ridge waveguides and modulators fabricated using smart guide*. Applied Physics Letters, **vol. 86, no. 16**:p. 161115. (Cited on page 19).

[48] Narayan R (1997) *Electrooptic coefficient variation in proton exchanged and annealed lithium niobate samples*. Selected Topics in Quantum Electronics, IEEE Journal of, **vol. 3, no. 3**:pp. 796–807. (Cited on page 20).

[49] Nozawa T, Miyazawa H and Miyazawa S (1990) *Water vapor effects on titanium diffusion into LiNbO3 substrates*. Japanese journal of applied physics, **vol. 29, no. 10R**:p. 2180. (Cited on page 23).

[50] Schmidt R and Kaminow I (1974) *Metal-diffused optical waveguides in LiNbO3*. Applied Physics Letters, **vol. 25, no. 8**:pp. 458–460. (Cited on page 24).

[51] Matano C (1933) *On the relation between the diffusion-coefficients and concentrations of solid metals (the nickel-copper system)*. Japanese Journal of Physics, **vol. 8, no. 3**:pp. 109–113. (Cited on page 24).

[52] Minakata M, Saito S, Shibata M *et al.* (1978) *Precise determination of refractive-index changes in Ti-diffused LiNbO3 optical waveguides*. Journal of Applied Physics, **vol. 49, no. 9**:pp. 4677–4682. (Cited on page 29).

[53] Fouchet S, Carenco A, Daguet C *et al.* (1987) *Wavelength dispersion of Ti induced refractive index change in LiNbO 3 as a function of diffusion parameters*. Lightwave Technology, Journal of, **vol. 5, no. 5**:pp. 700–708. (Cited on page 29).

[54] Caccavale F, Chakraborty P, Quaranta A *et al.* (1995) *Secondary-ion-mass spectrometry and near-field studies of Ti: LiNbO3 optical waveguides*. Journal of applied physics, **vol. 78, no. 9**:pp. 5345–5350. (Cited on page 29).

[55] Gupta S, *Optoelectronic Devices and Systems* (PHI Learning Pvt. Ltd., 2014). (Cited on page 32).

[56] Rune E (1951). *Measuring instrument of the recording type*. US Patent 2,566,443. (Cited on page 35).

[57] Le HP (1998) *Progress and trends in ink-jet printing technology*. Journal of Imaging Science and Technology, **vol. 42, no. 1**:pp. 49–62. (Cited on page 35).

[58] Terry SC, Jerman JH and Angell JB (1979) *A gas chromatographic air analyzer fabricated on a silicon wafer*. IEEE Transactions on Electron Devices, **vol. 26, no. 12**:pp. 1880–1886. (Cited on page 35).

[59] Shoji S, Esashi M and Matsuo T (1988) *Prototype miniature blood gas analyser fabricated on a silicon wafer*. Sensors and Actuators, **vol. 14, no. 2**:pp. 101 – 107. (Cited on page 35).

[60] van Lintel H, van De Pol F and Bouwstra S (1988) *A piezoelectric micropump based on micromachining of silicon*. Sensors and Actuators, **vol. 15, no. 2**:pp. 153 – 167. (Cited on page 35).

[61] Whitesides G and Stroock A (2001). *Flexible Methods for Microfluidics*. (Cited on pages 35 and 36).

[62] Stroock A and Whitesides G (2002) *Components for integrated poly (dimethylsiloxane) microfluidic systems*. Electrophoresis, **vol. 23, no. 20**:pp. 3461–3473. (Cited on pages 35 and 36).

[63] Ríos Á, Zougagh M and Avila M (2012) *Miniaturization through lab-on-a-chip: Utopia or reality for routine laboratories? A review*. Analytica Chimica Acta, **vol. 740**:pp. 1–11. (Cited on page 35).

[64] Kovarik ML, Ornoff DM, Melvin AT *et al.* (2013) *Micro total analysis systems: Fundamental advances and applications in the laboratory, clinic, and field*. Analytical Chemistry, **vol. 85, no. 2**:pp. 451–472. (Cited on page 35).

[65] Kenis PJA, Ismagilove RF and Whitesides GM (1999) *Microfabrication Inside Capillaries Using Multiphase Laminar Flow Patterning*. Science, **vol. 285, no. 5424**:pp. 83–85. (Cited on page 36).

[66] Stone H, Stroock A and Ajdari A (2004) *Engineering Flows in Small Devices*. Annual Review of Fluid Mechanics, **vol. 36, no. 1**:pp. 381–411. (Cited on page 36).

[67] Squires TM and Quake SR (2005) *Microfluidics: Fluid physics at the nanoliter scale*. Reviews of modern physics, **vol. 77, no. 3**:p. 977. (Cited on page 36).

[68] Yeo LY and Friend JR (2009) *Ultrafast microfluidics using surface acoustic waves*. Biomicrofluidics, **vol. 3, no. 1**:pp. 1–23. (Cited on pages 37 and 38).

[69] Brunet P, Baudoin M, Matar OB *et al.* (2010) *Droplet displacements and oscillations induced by ultrasonic surface acoustic waves: A quantitative study*. Physical Review E, **vol. 81, no. 3**:p. 036315. (Cited on pages 37 and 39).

[70] Tseng WK, Lin JL, Sung WC *et al.* (2006) *Active micro-mixers using surface acoustic waves on Y-cut 128° LiNbO 3*. Journal of Micromechanics and Microengineering, **vol. 16, no. 3**:p. 539. (Cited on pages 37 and 39).

[71] Esseling M, Zaltron A, Horn W *et al.* (2015) *Optofluidic droplet router*. Laser & Photonics Reviews, **vol. 9, no. 1**:pp. 98–104. (Cited on pages 37, 38, and 40).

[72] Sohler W, Hu H, Ricken R *et al.* (2008) *Integrated optical devices in lithium niobate*. Optics and Photonics News, **vol. 19, no. 1**:pp. 24–31. (Cited on pages 37 and 39).

[73] Carville NC, Collins L, Manzo M *et al.* (2014) *Biocompatibility of ferroelectric lithium niobate and the influence of polarization charge on osteoblast proliferation and function*. Journal of Biomedical Materials Research Part A, **vol. 00000**:pp. n/a–n/a. (Cited on page 37).

[74] Mazutis L, Gilbert J, Ung WL *et al.* (2013) *Single-cell analysis and sorting using droplet-based microfluidics*. Nature protocols, **vol. 8, no. 5**:pp. 870–891. (Cited on page 38).

[75] Köhler J, Henkel T, Grodrian A *et al.* (2004) *Digital reaction technology by micro segmented flow—components, concepts and applications*. Chemical Engineering Journal, **vol. 101, no. 1-3**:pp. 201–216. (Cited on page 38).

[76] Christopher GF, Bergstein J, End NB *et al.* (2009) *Coalescence and splitting of confined droplets at microfluidic junctions*. Lab Chip, **vol. 9, no. 8**:pp. 1102–1109. (Cited on page 38).

[77] Um E and Park JK (2009) *A microfluidic abacus channel for controlling the addition of droplets*. Lab Chip, **vol. 9, no. 2**:pp. 207–212. (Cited on page 38).

[78] Zhao S, Riaud A, Luo G *et al.* (2015) *Simulation of liquid mixing inside micro-droplets by a lattice Boltzmann method*. Chemical Engineering Science, **vol. 131**:pp. 118–128. (Cited on pages 38 and 45).

[79] Tan YC and Lee AP (2005) *Microfluidic separation of satellite droplets as the basis of a monodispersed micron and submicron emulsification system*. Lab Chip, **vol. 5, no. 10**:pp. 1178–1183. (Cited on page 38).

[80] Tan YC, Ho YL and Lee AP (2008) *Microfluidic sorting of droplets by size*. Microfluidics and Nanofluidics, **vol. 4, no. 4**:pp. 343–348. (Cited on page 38).

[81] Abate AR, Agresti JJ and Weitz DA (2010) *Microfluidic sorting with high-speed single-layer membrane valves*. Applied Physics Letters, **vol. 96, no. 20**:p. 203509. (Cited on page 38).

[82] Ahn K, Kerbage C, Hunt TP *et al.* (2006) *Dielectrophoretic manipulation of drops for high-speed microfluidic sorting devices*. Applied Physics Letters, **vol. 88, no. 2**:p. 024104. (Cited on page 38).

[83] Baret JC, Miller OJ, Taly V *et al.* (2009) *Fluorescence-activated droplet sorting (FADS): efficient microfluidic cell sorting based on enzymatic activity*. Lab Chip, **vol. 9, no. 13**:pp. 1850–1858. (Cited on page 38).

[84] Guo F, Ji XH, Liu K *et al.* (2010) *Droplet electric separator microfluidic device for cell sorting*. Applied Physics Letters, **vol. 96, no. 19**:p. 193701. (Cited on page 38).

[85] Jonáš A and Zemánek P (2008) *Light at work: The use of optical forces for particle manipulation, sorting, and analysis*. Electrophoresis, **vol. 29, no. 24**:pp. 4813–4851. (Cited on page 38).

[86] Tkachenko G and Brasselet E (2014) *Optofluidic sorting of material chirality by chiral light*. Nature Communications, **vol. 5**:pp. 1–7. (Cited on page 38).

[87] Elvira KS, Casadevall i Solvas X, Wootton RCR *et al.* (2013) *The past, present and potential for microfluidic reactor technology in chemical synthesis.*. Nature chemistry, **vol. 5, no. 11**:pp. 905–15. (Cited on page 38).

[88] Lagus TP and Edd JF (2013) *A review of the theory, methods and recent applications of high-throughput single-cell droplet microfluidics*. Journal of Physics D: Applied Physics, **vol. 46, no. 11**:p. 114005. (Cited on page 38).

[89] Zhao CX (2013) *Multiphase flow microfluidics for the production of single or multiple emulsions for drug delivery*. Advanced Drug Delivery Reviews, **vol. 65, no. 11-12**:pp. 1420–1446. (Cited on page 38).

[90] Tsui JH, Lee W, Pun SH *et al.* (2013) *Microfluidics-assisted in vitro drug screening and carrier production*. Advanced Drug Delivery Reviews, **vol. 65, no. 11-12**:pp. 1575–1588. (Cited on page 38).

[91] Choi JH, Lee SK, Lim JM *et al.* (2010) *Designed pneumatic valve actuators for controlled droplet breakup and generation*. Lab Chip, **vol. 10, no. 4**:pp. 456–461. (Cited on page 39).

[92] Hong JS, Lee BS, Moon D *et al.* (2010) *Pumpless dispensing of a droplet by breaking up a liquid bridge formed by electric induction*. ELECTROPHORESIS, **vol. 31, no. 8**:pp. 1357–1365. (Cited on page 39).

[93] Adamiak K and Floryan JM (2011) *Dynamics of water droplet distortion and breakup in a uniform electric field*. IEEE Transactions on Industry Applications, **vol. 47, no. 6**:pp. 2374–2383. (Cited on page 39).

[94] Robert de Saint Vincent M, Chraïbi H and Delville JP (2015) *Optical Flow Focusing: Light-Induced Destabilization of Stable Liquid Threads*. Physical Review Applied, **vol. 4, no. 4**:p. 044005. (Cited on page 39).

[95] Wu WD, Lin SX and Chen XD (2011) *Monodisperse droplet formation through a continuous jet break-up using glass nozzles operated with piezoelectric pulsation*. AIChE Journal, **vol. 57, no. 6**:pp. 1386–1392. (Cited on page 39).

[96] Churski K, Michalski J and Garstecki P (2010) *Droplet on demand system utilizing a computer controlled microvalve integrated into a stiff polymeric microfluidic device*. Lab Chip, **vol. 10, no. 4**:pp. 512–518. (Cited on page 39).

[97] Park SY, Wu TH, Chen Y *et al.* (2011) *High-speed droplet generation on demand driven by pulse laser-induced cavitation*. Lab Chip, **vol. 11, no. 6**:pp. 1010–1012. (Cited on page 39).

[98] Umbanhowar PB, Prasad V and Weitz Da (2000) *Monodisperse emulsion generation via drop break off in a coflowing stream*. Langmuir, **vol. 16, no. 2**:pp. 347–351. (Cited on page 40).

[99] Thorsen T, Roberts RW, Arnold FH *et al.* (2001) *Dynamic pattern formation in a vesicle-generating microfluidic device*. Physical Review Letters, **vol. 86, no. 18**:pp. 4163–4166. (Cited on pages 40, 45, and 90).

[100] Garstecki P, Fuerstman MJ, Stone HA *et al.* (2006) *Formation of droplets and bubbles in a microfluidic T-junction-scaling and mechanism of break-up*. Lab Chip, **vol. 6, no. 3**:pp. 437–446. (Cited on pages 40, 46, 49, 90, 92, 93, and 94).

[101] Steegmans MLJ, De Ruiter J, Schroën KGPH *et al.* (2010) *A descriptive force-balance model for droplet formation at microfluidic Y-junctions*. AIChE Journal, **vol. 56, no. 10**:pp. 2641–2649. (Cited on page 40).

[102] Wolf-Gladrow DA, *Lattice-gas cellular automata and lattice Boltzmann models: An Introduction*. 1725 (Springer Science & Business Media, 2000). (Cited on page 45).

[103] Succi S (2001). *Succi_ The_ Lattice_ Boltzmann_ Equation.pdf*. (Cited on page 45).

[104] Li XB, Li FC, Yang JC *et al.* (2012) *Study on the mechanism of droplet formation in T-junction microchannel*. Chemical Engineering Science, **vol. 69, no. 1**:pp. 340–351. (Cited on page 45).

[105] Qian D and Lawal A (2006) *Numerical study on gas and liquid slugs for Taylor flow in a T-junction microchannel*. Chemical Engineering Science, **vol. 61, no. 23**:pp. 7609–7625. (Cited on page 45).

[106] DE MENECH M, GARSTECKI P, JOUSSE F *et al.* (2008) *Transition from squeezing to dripping in a microfluidic T-shaped junction*. Journal of Fluid Mechanics, **vol. 595**:pp. 141–161. (Cited on pages 46 and 90).

[107] Stone H (2005) *On lubrication flows in geometries with zero local curvature*. Chemical Engineering Science, **vol. 60, no. 17**:pp. 4838–4845. (Cited on page 48).

[108] Xu JH, Li SW, Tan J *et al.* (2008) *Correlations of droplet formation in T-junction microfluidic devices: From squeezing to dripping*. Microfluidics and Nanofluidics, **vol. 5, no. 6**:pp. 711–717. (Cited on page 49).

[109] van Steijn V, Kleijn CR and Kreutzer MT (2009) *Flows around Confined Bubbles and Their Importance in Triggering Pinch-Off*. Physical Review Letters, **vol. 103, no. 21**:p. 214501. (Cited on page 51).

[110] Kumar S, Kumar S, Ali MA *et al.* (2013) *Microfluidic-integrated biosensors: Prospects for point-of-care diagnostics*. Biotechnology Journal, **vol. 8, no. 11**:pp. 1267–1279. (Cited on page 55).

[111] Korczyk PM, Derzsi L, Jakieła S *et al.* (2013) *Microfluidic traps for hard-wired operations on droplets*. Lab on a Chip, **vol. 13, no. 20**:pp. 4096–4102. (Cited on page 55).

[112] Faustino V, Catarino SO, Lima R *et al.* (2015) *Biomedical microfluidic devices by using low-cost fabrication techniques: A review*. Journal of biomechanics. (Cited on page 55).

[113] Tsai LF, Dahlquist WC, Kim S *et al.* (2011) *Bonding of polydimethylsiloxane microfluidics to silicon-based sensors*. Journal of Micro/Nanolithography, MEMS, and MOEMS, **vol. 10, no. 4**:pp. 043009–043009–8. (Cited on page 55).

[114] Xiang Q, Xuan X, Xu B *et al.* (2005) *Multi-Functional Particle Detection with Embedded Optical Fibers in a Poly (dimethylsiloxane) Chip*. Instrumentation Science and Technology, **vol. 33, no. 5**:pp. 597–607. (Cited on page 55).

[115] Regehr KJ, Domenech M, Koepsel JT *et al.* (2009) *Biological implications of polydimethylsiloxane-based microfluidic cell culture*. Lab Chip, **vol. 9**:pp. 2132–2139. (Cited on page 55).

[116] Zheng B, Tice JD, Roach LS *et al.* (2004) *A Droplet-Based, Composite PDMS/Glass Capillary Microfluidic System for Evaluating Protein Crystallization Conditions by*

Microbatch and Vapor-Diffusion Methods with On-Chip X-Ray Diffraction. Angewandte Chemie International Edition, **vol. 43, no. 19**:pp. 2508–2511. (Cited on page 56).

[117] Wilson ME, Kota N, Kim Y *et al.* (2011) *Fabrication of circular microfluidic channels by combining mechanical micromilling and soft lithography*. Lab Chip, **vol. 11**:pp. 1550–1555. (Cited on page 56).

[118] Iliescu C, Taylor H, Avram M *et al.* (2012) *A practical guide for the fabrication of microfluidic devices using glass and silicon*. Biomicrofluidics, **vol. 6, no. 1**. (Cited on page 56).

[119] Osellame R, Cerullo G and Ramponi R, *Femtosecond Laser Micromachining: Photonic and Microfluidic Devices in Transparent Materials*, vol. 123 (Springer Science & Business Media, 2012). (Cited on page 56).

[120] Chauvet M, Al Fares L and Devaux F (2012) *Self-trapped beams for fabrication of optofluidic chips*. Proc. SPIE, **vol. 8434**:pp. 84340Q–84340Q–7. (Cited on page 56).

[121] Chauvet M, Al Fares L, Guichardaz B *et al.* (2012) *Integrated optofluidic index sensor based on self-trapped beams in LiNbO3*. Applied Physics Letters, **vol. 101, no. 18**. (Cited on page 56).

[122] Pozza G, Kroesen S, Bettella G *et al.* (2014) *T-junction droplet generator realised in lithium niobate crystals by laser ablation*. Optofluidics, Microfluidics and Nanofluidics, **vol. 1, no. 1**. (Cited on page 56).

[123] Grilli S, Ferraro P, De Natale P *et al.* (2005) *Surface nanoscale periodic structures in congruent lithium niobate by domain reversal patterning and differential etching*. Applied Physics Letters, **vol. 87, no. 23**. (Cited on page 56).

[124] Korkishko Y, Fedorov V and Feoktistova O (2000) *LiNbO/sub 3/ optical waveguide fabrication by high-temperature proton exchange*. Lightwave Technology, Journal of, **vol. 18, no. 4**:pp. 562–568. (Cited on page 57).

[125] Bianconi M, Bergamini F, Bentini G *et al.* (2008) *Modification of the etching properties of x-cut Lithium Niobate by ion implantation*. Nuclear Instruments and Methods

in Physics Research Section B: Beam Interactions with Materials and Atoms, **vol. 266, no. 8**:pp. 1238–1241. (Cited on page 57).

[126] Tamura M and Yoshikado S (2001) *Etching characteristics of LiNbO3 crystal by fluorine gas plasma reactive ion etching*. Science and Technology of Advanced Materials, **vol. 2, no. 3–4**:pp. 563 – 569. (Cited on page 57).

[127] Ren Z, Heard PJ, Marshall JM *et al.* (2008) *Etching characteristics of LiNbO3 in reactive ion etching and inductively coupled plasma*. Journal of Applied Physics, **vol. 103, no. 3**. (Cited on page 57).

[128] Sridhar M, Maurya DK, Friend JR *et al.* (2012) *Focused ion beam milling of microchannels in lithium niobate*. Biomicrofluidics, **vol. 6, no. 1**:p. 012819. (Cited on page 57).

[129] Al-Shibaany ZYA, Hedley J, Huo D *et al.* (2014) *Micromachining Lithium Niobate for Rapid Prototyping of Resonant Biosensors*. IOP Conference Series: Materials Science and Engineering, **vol. 65, no. 1**:p. 012030. (Cited on page 58).

[130] Sohn IB, Lee MS and Chung JY (2005) *Fabrication of optical splitter and passive alignment technique with a femtosecond laser*. Photonics Technology Letters, IEEE, **vol. 17, no. 11**:pp. 2349–2351. (Cited on page 58).

[131] Gattass RR and Mazur E (2008) *Femtosecond laser micromachining in transparent materials*. Nature photonics, **vol. 2, no. 4**:pp. 219–225. (Cited on page 58).

[132] Della Valle G, Osellame R and Laporta P (2009) *Micromachining of photonic devices by femtosecond laser pulses*. Journal of Optics A: Pure and Applied Optics, **vol. 11, no. 1**:p. 013001. (Cited on page 58).

[133] Sohn IB, Lee MS, Woo JS *et al.* (2005) *Femtosecond Laser Application to Optical Memory and Microfluidics*. J. Opt. Soc. Korea, **vol. 9, no. 3**:pp. 92–94. (Cited on page 58).

[134] Gui L, Xu B and Chong TC (2004) *Microstructure in lithium niobate by use of focused femtosecond laser pulses*. Photonics Technology Letters, IEEE, **vol. 16, no. 5**:pp. 1337–1339. (Cited on page 58).

[135] Greuters J and Rizvi NH (2003) *UV laser micromachining of silicon, indium phosphide and lithium niobate for telecommunications applications*. Proc. SPIE, **vol. 4876**:pp. 479–486. (Cited on page 58).

[136] Christensen FK and Müllenborn M (1995) *Sub-band-gap laser micromachining of lithium niobate*. Applied Physics Letters, **vol. 66, no. 21**:pp. 2772–2773. (Cited on page 58).

[137] Chong HW, Mitchell A, Hayes JP *et al.* (2002) *Investigation of KrF excimer laser ablation and induced surface damage on lithium niobate*. Applied Surface Science, **vol. 201, no. 1–4**:pp. 196 – 203. (Cited on page 58).

[138] Malshe A, Deshpande D, Stach E *et al.* (2004) *Investigation of Femtosecond Laser-assisted Micromachining of Lithium Niobate*. {CIRP} Annals - Manufacturing Technology, **vol. 53, no. 1**:pp. 187 – 190. (Cited on page 58).

[139] Ward D, Statz E and Nelson K (2006) *Fabrication of polaritonic structures in LiNbO3 and LiTaO3 using femtosecond laser machining*. Applied Physics A, **vol. 86, no. 1**:pp. 49–54. (Cited on page 58).

[140] Bhattacharya S, Datta A, Berg JM *et al.* (2005) *Studies on surface wettability of poly (dimethyl) siloxane (PDMS) and glass under oxygen-plasma treatment and correlation with bond strength*. Microelectromechanical Systems, Journal of, **vol. 14, no. 3**:pp. 590–597. (Cited on pages 70 and 71).

[141] Young T (1805) *An essay on the cohesion of fluids*. Philosophical Transactions of the Royal Society of London, (pp. 65–87). (Cited on page 75).

[142] Rowlinson JS and Widom B, *Molecular theory of capillarity* (Courier Corporation, 2013). (Cited on page 75).

[143] Sanna S and Schmidt WG (2010) *Lithium niobate X-cut, Y-cut, and Z-cut surfaces from ab initio theory*. Physical Review B, **vol. 81, no. 21**:p. 214116. (Cited on page 76).

[144] Fadeev AY and Kazakevich YV (2002) *Covalently attached monolayers of oligo (dimethylsiloxane) s on silica: a siloxane chemistry approach for surface modification*. Langmuir, **vol. 18, no. 7**:pp. 2665–2672. (Cited on page 78).

[145] Rozlosnik N, Gerstenberg MC and Larsen NB (2003) *Effect of solvents and concentration on the formation of a self-assembled monolayer of octadecylsiloxane on silicon (001)*. Langmuir, **vol. 19, no. 4**:pp. 1182–1188. (Cited on page 78).

[146] Manifar T, Rezaee A, Sheikhzadeh M *et al.* (2008) *Formation of uniform self-assembly monolayers by choosing the right solvent: OTS on silicon wafer, a case study*. Applied Surface Science, **vol. 254, no. 15**:pp. 4611–4619. (Cited on page 78).

[147] Law K and Zhao H, *Surface Wetting: Characterization, Contact Angle, and Fundamentals* (Springer International Publishing, 2015). (Cited on page 78).

[148] Xu JH, Li SW, Tan J *et al.* (2006) *Controllable preparation of monodisperse O/W and W/O emulsions in the same microfluidic device*. Langmuir, **vol. 22, no. 19**:pp. 7943–7946. (Cited on page 82).

[149] Nie Z, Seo M, Xu S *et al.* (2008) *Emulsification in a microfluidic flow-focusing device: effect of the viscosities of the liquids*. Microfluidics and Nanofluidics, **vol. 5, no. 5**:pp. 585–594. (Cited on page 89).

[150] Zeng Y, Novak R, Shuga J *et al.* (2010) *High-performance single cell genetic analysis using microfluidic emulsion generator arrays*. Analytical chemistry, **vol. 82, no. 8**:pp. 3183–3190. (Cited on page 89).

[151] Tarchichi N, Chollet F and Manceau JF (2014) *Oil-in-water droplets generation in dripping regime with channel partial wetting*. Micro and Nanosystems, **vol. 6, no. 3**:pp. 145–155. (Cited on page 89).

[152] Pang FM, Seng CE, Teng TT *et al.* (2007) *Densities and viscosities of aqueous solutions of 1-propanol and 2-propanol at temperatures from 293.15 K to 333.15 K*. Journal of Molecular Liquids, **vol. 136, no. 1**:pp. 71–78. (Cited on page 107).

[153] Grad M, Tsai C, Yu M *et al.* (2010) *Transient sensing of liquid films in microfluidic channels with optofluidic microresonators*. Measurement Science and Technology, **vol. 21, no. 7**:p. 075204. (Cited on page 120).